

ARMY RESEARCH LABORATORY



Experimental Investigation of Wave and Fracture Phenomena in Impacted Ceramics: Sapphire

by H. Senf and S. Winkler

ARL-CR-310

February 1997

prepared by

**Franhofer-Institut für Kurzzeitdynamik
Ernst-Mach-Institut
Weil am Rhein, Germany**

under contract

DAJA45-90-C-0053

ERIC QUALITY INSPECTED 4

Approved for public release; distribution is unlimited.

19970404 033

The findings in this report are not to be construed as an official Department of the Army position unless so designated by other authorized documents.

Citation of manufacturer's or trade names does not constitute an official endorsement or approval of the use thereof.

Destroy this report when it is no longer need. Do not return it to the originator.

Army Research Laboratory

Aberdeen Proving Ground, MD 21005-5066

ARL-CR-310

February 1997

Experimental Investigation of Wave and Fracture Phenomena in Impacted Ceramics: Sapphire

H. Senf, S. Winkler
Franhofer-Institut für Kurzzeitdynamik

prepared by

Franhofer-Institut für Kurzzeitdynamik
Ernst-Mach-Institut
Weil am Rhein, Germany

under contract

DAJA45-90-C-0053

Approved for public release; distribution is unlimited.

Abstract

This report documents the experimental investigation of wave and fracture phenomena in monocrystalline sapphire. This research includes comparisons with glass and complements the Ernst-Mach-Institut investigation of ceramics and glasses that was published subsequently in ARL-CR-214, "Experimental Investigations of Wave and Fracture Phenomena in Impacted Ceramics and Glasses." A detailed discussion of wave phenomena and fracture phenomena is included, as well as a discussion of an electric emission method for wave and fracture detection. The work was made possible by the state-of-the-art, high-speed photographic capability available at the Ernst-Mach-Institut, specifically two 24-spark Cranz-Shradin cameras, which can be used both in transmission and reflectance. Sapphire tiles were impacted by both spherical and flat projectiles and the generation of pressure waves and disintegration effects were observed. Twenty-four high-quality photographic images could be obtained at predetermined time intervals of less than 1 microsecond.

PREFACE

This report documents the experimental investigation of wave and fracture phenomena in monocrystalline sapphire that was conducted for the U.S. Army Research Laboratory (ARL) by the Fraunhofer-Institut für Kurzzeitdynamik Ernst-Mach-Institut, Weil am Rhein, Germany. The research was originally conducted in 1990 and is being republished here as an ARL report to provide a wider dissemination of this early insight into crack and fracture phenomena that is applicable to other brittle materials. This work includes comparisons with glass and complements the Ernst Mach Institute investigation of ceramics and glasses that was published subsequently in ARL-CR-214, "Experimental Investigations of Wave and Fracture Phenomena in Impacted Ceramics and Glasses". A detailed discussion of wave phenomena and fracture phenomena is included as well as a discussion of a electric emission method for wave and fracture detection. The work was made possible by the state-of-the-art, high-speed photographic capability available at the Ernst-Mach-Institut, specifically two 24-spark Cranz-Shradin cameras, which can be used both in transmission and reflectance. The sapphire tiles were impacted by both spherical and flat projectiles and the generation of pressure waves and disintegration effects were observed. Twenty-four high quality photographic images could be obtained at predetermined time intervals of less than $1\mu\text{s}$ in transmission.

The results were compared with then current work on alumina and glasses as target materials. A terminal crack velocity was not found. Crack velocities exceeding the Rayleigh wave speed were measured. Similar to glass, nucleations of cracks in the field between the primary wave front and the front of the disintegration area form a damage velocity which can approach the longitudinal wave speed. Usually, cracks did not follow crystal planes and the influence of the crystal structure does not seem to be a strong factor.

The report was originally published as the final report to Contract number DAJA 45-90-C-0053, prepared for the European Research Office (ERO) of the U.S. Army which oversaw the contract for the U.S. Army Research Laboratory (the former U.S. Army Ballistic Research Laboratory and U.S. Army Materials Technology Laboratory) which funded the research. The sapphire tiles were provided by Dr. Dennis Viechnicki, now, Chief of the Materials Branch of the Weapons and Materials Research Directorate of the U.S. Army Research Laboratory.

The Armor Mechanics Branch would also like to acknowledge the long-term professional interaction with the Ernst Mach Institute, particularly, Mr. Hermann Senf, which has led to many fruitful technical exchanges during the course of this work. Further fracture and crack analysis is expected on other ceramics of interest in the future.

Any questions or request for clarifications can be directed to Mr. William A. Gooch, Armor Mechanics Branch, (410) 278-6080.

INTENTIONALLY LEFT BLANK

TABLE OF CONTENTS

	<u>PAGE</u>
PREFACE	iii
LIST OF FIGURES	vii
LIST OF TABLES	x
1. INTRODUCTION	1
2. EXPERIMENTAL PROCEDURE	2
3. MATERIALS	5
3.1 Glass.....	5
3.2 Sapphire	5
4. IMPACT EXPERIMENTS	9
4.1 General	9
4.2 Description of Impact Experiments	10
5. WAVE PHENOMENA	39
5.1 Camera Limits	39
5.2 Wave Velocities and Elastic Constants	40
5.3 Wave Formation in a Slab	43
5.4 Wave Splitting	44
5.5 Energy Distribution	47
5.6 Temperature of the Wave Field	51
6. FRACTURE PHENOMENA	53
6.1 General	53
6.2 Summary of Fracture Phenomena	53
6.3 Mescall Zone Development	57

7.	ELECTRIC EMISSION METHOD FOR WAVE AND FRACTURE DETECTION	64
7.1	General	64
7.2	Pre-experiments for Wave Detection	65
7.3	Application in Experiments	68
8.	SUMMARY AND CONCLUSIONS	72
9.	ACKNOWLEDGMENTS	74
10.	REFERENCES	75
	DISTRIBUTION LIST	77
	REPORT DOCUMENTATION PAGE	87

LIST OF FIGURES

<u>Figure</u>		<u>Page</u>
2.1	Experimental arrangement	2
2.2	Photographic arrangement in transmission	3
2.3	Trigger circuit	4
2.4	Electric Arrangement	4
4.1	High speed photographs, #1034	11
4.2	High speed photographs, #1035	12
4.3	Crack events, #1035	13
4.4	Total reflection at a narrow crack	14
4.5	Angles of crack planes	15
4.6	High speed photographs, #1038	17
4.7	High speed photographs, #1039	19
4.8	Space-time diagram of waves and fractures, #1039	20
4.9	Wave details and fracture nucleation in the glass target, #1039	20
4.10	High speed photographs, #1040	22
4.11	Space-time diagram of waves, #1040	23
4.12	Space-time diagram of fractures, #1040	23
4.13	Cone crack diagram, #1040	24
4.14	Edge nucleation movement, #1040	24
4.15	Edge crack velocity, #1040	25
4.16	High speed photographs, #1049	27

4.17	Space-time diagram of waves and fractures, #1049	28
4.18	High speed photographs, #1050	29
4.19	Space-time diagram of waves, #1050	30
4.20	Edge crack nucleation effects, #1050	31
4.21	Space-time diagram of inside nucleations, #1050	31
4.22	High speed photographs, #1051	32
4.23	Space-time diagram of waves and fractures, #1051	33
4.24	High speed photographs, #1052	35
4.25	Space-time diagram of waves, #1052	36
4.26	Space-time diagram of fractures, #1052	36
4.27	Spallation at the rear edge, #1052	37
5.1	Camera light pulse (spark); SR = 50ns	39
5.2	Shear wave formation and wave splitting in a slab (top view)	45
5.3	Particle paths in a tile subjected to a wave (top view)	46
5.4	Correspondence of sparks and pictures	47
5.5	Distribution of energy density in the wave	50
5.6	Distribution of radial stress in the wave	51
5.7	Initial adiabatic wave temperature rise vs. impact velocity in sapphire	52
6.1	Corner crack, #1052, 114 m/s	55
6.2	Fracture on a sapphire fragment, #1035, 39 m/s	56
6.3	Particle size vs. impact velocity in sapphire	59

6.4	Sapphire particles on steel projectile, #1040	61
6.5	Sapphire particles on sapphire, #1040	62
6.6	Sapphire particles on steel, #1040, particle size \leq 1 μm	63
7.1	Electric emission method and FET probes	64
7.2	Signals from two EE probes with an impact loaded Araldite B sample	66
7.3	Electric emission signals from two probes with sapphire	67
7.4	Contact signal and electric emission signal with TiB ₂	67
7.5a	Probe arrangement and propagation times (sapphire only)	69
7.5b	EE signals 1 and 2, shot #1034, $v_o = 98 \text{ m/s}$	69
7.5c	EE signals 1 and 2, shot #1035, sapphire, $v_o = 39 \text{ m/s}$	69
7.6a	Probe arrangement and propagation times	71
7.6b	EE signals 1 and 2, shot #1050, sapphire, $v_o = 193 \text{ m/s}$	71
7.6c	EE signals 1 and 2, shot #1052, sapphire, $v_o = 114 \text{ m/s}$	71

LIST OF TABLES

<u>Table</u>		<u>Page</u>
3.1	Properties of float glass	5
3.2	Properties of sapphire	6
3.3	Lattice parameters	7
3.4	Orientation of the sample surfaces	7
3.5	Lattice planes related to the {110} plane	8
3.6	Lattice planes related to the {300} plane	8
4.1	List of impact experiments	9
5.1	Longitudinal wave velocities in sapphire	41
5.2	Rayleigh wave velocities in sapphire	41
6.1	Fracture toughness and energy release rates for ceramics	60

1. INTRODUCTION

Part of the contract DAJA45-90-C-0053 deals with the investigation of sapphire as a material subjected to impact loading. Due to a different source of this material¹ and because of its different type compared to the other materials of the contract it was decided to report the results of these investigations separately. This underlines also the particular role of sapphire in the bunch of ceramic materials used for armor purposes. This kind of an expensive material may not be considered to be a component of a sophisticated armor system rather than applied in exceptional cases. Methods of investigations, on the other hand, are those developed in a sequence of programs carried out during the last decade and are the same, therefore, for all materials of the current contract, delivering results which can be compared to each other.

The original intention to study different energy absorbing failure processes in different materials by high-speed photography was again the driving idea with the present contract. Experiences and surprising results were gathered in previous programs with glass [1] and an ERO-Contract with alumina as the test material [2, 3]. After receiving a set of 6 sapphire tiles the question arose whether a similar behavior would be found with this material - being transparent and monocrystalline - as before with the opaque polycrystalline material of the same chemical composition.

In addition to the planned investigation of wave and fracture phenomena it was also planned trying to recover at least essential parts - the smallest particles - of the debris of the comminution or Mescall zone [4] in front of the impactor, which must be considered to be the main energy absorber in an impacted target.

¹ This material was made available
by Dr. Dennis Viechnicki, AMTL, Watertown

2. EXPERIMENTAL PROCEDURE

The experimental arrangement is shown in Figure 2.1. The target is tile-shaped and hit by a metal projectile. A trigger device activates electronic measuring and registration means, e.g., the high speed Cranz-Schardin camera. This camera is capable to take 24 pictures with frame-rates down to the tenths of a microsecond range and with exposure times around $0.5 \mu\text{s}$ (see sect.5, WAVE PHENOMENA). Wave and fracture phenomena are photographed to understand how the applied shock energy is dissipated in the tile. The optical arrangement for observation in transmission is shown in Figure 2.2. The tiles mounted close to the gun muzzle are impacted edge-on. The impactor is mounted on a sabot for a proper guidance. When impacting the sabot is still guided in the barrel so that the flat impact condition cannot be disturbed by air turbulences.

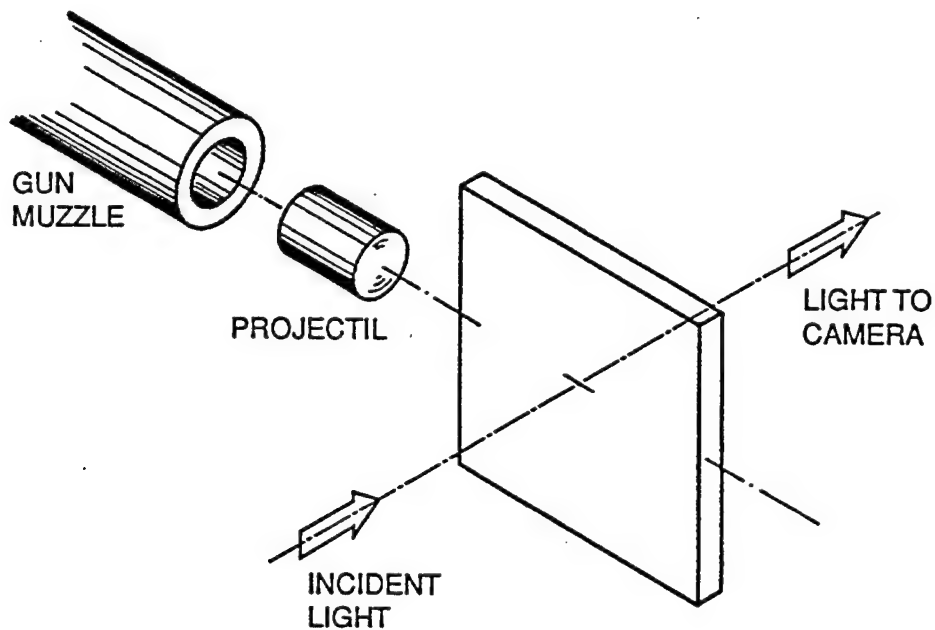


Fig. 2.1 Experimental arrangement

Experiments with an expensive test material such as sapphire or with a limited number of specimens need to be accompanied by auxiliary experiments with an inexpensive test material in order to shake down the experimental procedure and to get information on the general mechanical behavior in such a complex experiment.

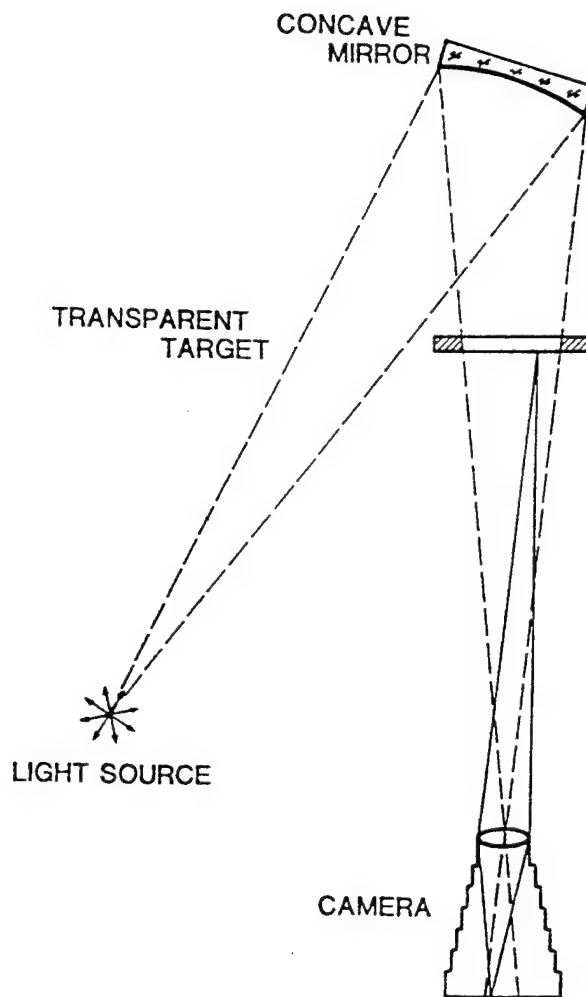


Fig. 2.2 Photographic arrangement in transmission

A critical and difficult part of impact experiments is triggering the optical and electronic measurement devices. For experiments with a slab as an impactor a twisted pair of 50 µm diameter enamelled copper wires has been glued onto the impacted edge in order to be short-circuited by the impactor within a distance of less than two diameters of the wire which is less than 100 µm before contact with the target appears. For an impact velocity of 100 m/s, for instance, the trigger signal is to be expected in the short time interval of -1 µs to 0 µs, with zero time being the instant of impact. The electric circuit to form a trigger signal from this contact signal is shown in Figure 2.3.

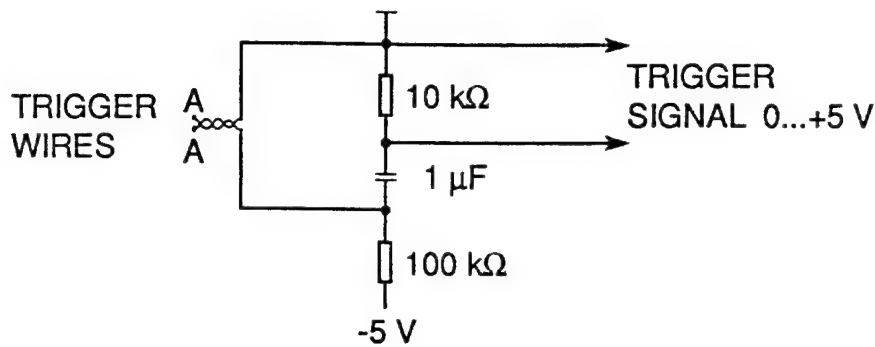


Fig. 2.3 Trigger circuit

Functioning of this trigger circuit can almost completely be pre-tested. Shortening the trigger wires at A-A and successfully triggering does not only show that the circuit works and the signal is received but confirms also that the trigger wires are intact, neither broken nor short-circuited. The signal of this circuit starts a delay generator which also serves as a TTL-pulse shaper as well, Fig. 2.4. Registration devices are triggered from this unit.

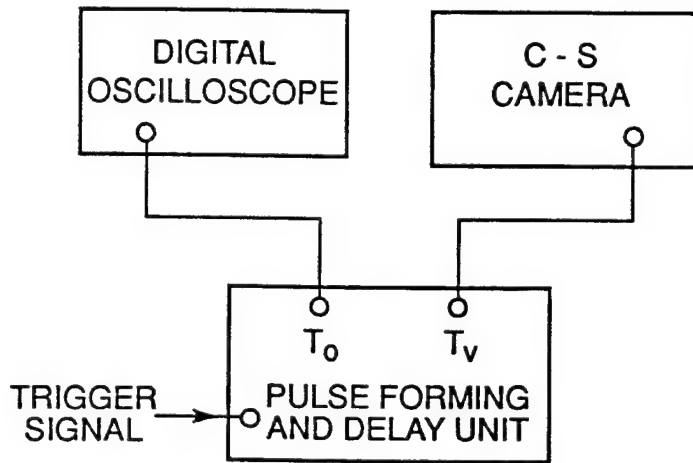


Fig. 2.4 Electric arrangement

A relatively new technique has also been applied with these experiments. This is the electric emission method (EE) which can detect energy-related effects in an arbitrary material, in particular fracture events [16, 17]. Method and results are described in Chapter 7.

3. MATERIALS

3.1 Glass

Accompanying experiments have been carried out with float glass as a target material as in the previous investigations [1-3]. This material is available and inexpensive. Material parameters are presented in Table 3.1. This float glass exhibits residual stresses caused by production with tangential compression stress at the surfaces and an inside tensile stress component.

PROPERTY	CONDITION	QUANTITY
DENSITY, ρ	published data	2500 kg/m ³
SOUND WAVE VELOCITY, c_L	published data	5860 m/s
POISSON's RATIO, ν	published data	0.23
YOUNG's MODULUS, E	published data ρc^2	70 GPa 86 GPa
ACOUSTIC IMPEDANCE	$Z = \rho c$	$15 \cdot 10^6$ kg/(m ² s)
HARDNESS, HV	published data	680

Table 3.1 Properties of float glass

3.2 Sapphire

Published sapphire material parameters are taken from data sheets or are measured - respectively calculated - during work on this contract. The published data sometimes vary considerably. Young's modulus, for example, varies in literature from about 350 GPa to about 390 GPa, probably depending on the orientation of the test bar compared with the crystallographic C-axis. Methods for determination of material parameters during this work are described in detail in chapter 5 of this report.

All target samples used in experiments of this part of the contract were tile shaped and had the dimensions 100 mm x 100 mm x 10 mm.

PROPERTY	CONDITION	QUANTITY
DENSITY, ρ	published data $\rho = M/V$	3980 kg/m ³ 3995 kg/m ³
SOUND WAVE VELOCITY; c_L	published data ultrasonic this work, average	11360 m/s 11538 m/s
SHEAR WAVE VELOCITY, c_T	published data this work	6170 m/s
RAYLEIGH WAVE VELOCITY; c_R	published data this work	5720 m/s
YOUNG's MODULUS, E	publ. data, 30° C ρc^2 this work	350 - 390 GPa 516 GPa 390 GPa
POIS.'s RAT.; v	this work	0.29
ACOUST. IMPED	$Z = \rho c$	$45.4 \cdot 10^6$ kg/(m ² s)
MELTING POINT	published data	(2040 ± 10)° C
COMPR. STRENGTH	published data	2.1 GPa
TENSILE STRENGTH	20° C 500° C 1000° C	0.400 GPa 0.276 GPa 0.359 GPa
MODULUS OF RUOTURE	max. bend. stress, orient. dependent	0.449 GPa 0.690 GPa
MODULUS OF RIGIDITY	minimum value, orient. dependent	148 GPa
SPECIFIC HEAT	20° C different 20° C sources	419 J/(kg·K) 754 J/(kg·K)
THERMAL CONDUCTIVITY	heat flow, 26° C heat flow, 23° C	0.251 J/(m·s·K) 0.209 J/(m·s·K)

Table 3.2 Properties of sapphire

General properties of this material, also compared with others, are cited from a manufacturer's brochure [5]:

Sapphire, single crystal aluminum oxide, is classed as a rhombohedral structure but is normally indexed on hexagonal axes. Optically, it is a negative, uniaxial crystal in the visible; it exhibits anisotropy in its physical, thermal, and dielectric properties. An amphoteric semiconductor, sapphire's energy band gap, approximately 10 eV, which is one of the larger for oxide crystals, permits useful optical transmission to extend from about 1450 Å to 5.5 µm.

(...) Generally, most sapphire grown by this (the CZOCHRALSKI) process is such that the c-axis or optic axis is inclined at an angle of 60 degrees from the growth axis. Where the growth axis is coincident with the c-axis, usually called zero-degree orientation, the optical quality of the sapphire is substantially lower than that obtained in all other growth orientations. ...

Of all practical optical materials (...) Cz sapphire has the greatest strength, the most useful broadband transmission, the highest operating temperature capability, the highest thermal conductivity, the highest dielectric constant and dielectric strength, the best degree of chemical inertness, the highest hardness, the best rain erosion resistance.

X-Ray diffraction measurements were carried out in order to identify the crystal orientation. As a test piece a fragment of the target of shot # 1035 was used. This showed a part of the large surface as well as a part of an edge surface. The applied Cr-K α radiation corresponds to a 2.2897 Å wavelength. The lattice parameters are listed in Table 3.3. The determined orientations of the surfaces are shown in Table 3.4

$a = 4.758 \text{ \AA}$	$b = 4.758 \text{ \AA}$	$c = 12.991 \text{ \AA}$
$a_{Rh} = 5.1282 \text{ \AA}$	$\alpha_{Rh} = 55.279^\circ$	$\tau_{Rh} = 42.956^\circ$

Table 3.3 Lattice parameters

	CRYSTAL PLANE	ANGLE OF DIFFRACTION, 20
SURFACE	{300}	112.863°
EDGE	{110}	57.532°

Table 3.4 Orientation of the sample surfaces

Theoretically, the hexagonal-rhombohedral crystal exhibits 61 possible lattice planes with many of them counted twice or more in this systematic way. These planes are listed in Table 3.5 related to the {110} plane which is the edge surface and in Table 3.6 related to the large surface which is the {300} plane. Any of the lattice planes can act as a cleavage plane, however, with different strength.

h	k	l	ANGLE
-2	1	0	120.000
-1	-1	0	180.000
1	2	0	60.000
1	-2	0	120.000
1	1	0	0.000
2	-1	0	60.000

Table 3.5 Lattice planes related to the {110} plane

h	k	l	ANGLE	h	k	l	ANGLE	h	k	l	ANGLE
-3	0	-3	162.402	-1	-2	-4	132.970	2	-3	-5	80.672
-3	0	0	180.000	-1	-2	5	130.419	2	-3	4	80.189
-3	0	3	162.402	-1	3	-5	80.672	2	2	-7	70.449
-3	1	-5	144.141	-1	3	4	80.189	2	-2	8	71.970
-3	1	4	148.431	0	-3	-3	118.464	2	0	-8	51.755
-3	2	-4	132.970	0	-3	0	120.000	2	0	7	47.988
-3	2	5	130.419	0	-3	3	118.464	2	1	-4	31.569
-3	3	-3	118.464	0	-2	-8	108.030	2	1	5	35.859
-3	3	0	120.000	0	-2	7	109.551	3	-3	-3	61.536
-2	-1	-5	144.141	0	0	-9	90.000	3	-3	0	60.000
-2	-1	4	148.431	0	0	9	90.000	3	-3	3	61.536
-2	0	-7	132.012	0	2	-7	70.449	3	-2	-5	49.581
-2	0	8	128.245	0	2	8	71.970	3	-2	4	47.030
-2	2	-8	108.030	0	3	-3	61.536	3	-1	-4	31.569
-2	2	7	109.551	0	3	0	60.000	3	-1	5	35.859
-2	3	-4	99.811	0	3	3	61.536	3	0	-3	17.598
-2	3	5	99.328	1	-3	-4	99.811	3	0	0	0.000
				1	-3	5	99.328	3	0	3	17.598
				1	2	-5	49.581				
				1	2	4	47.030				

Table 3.6 lattice planes related to the {300} plane

4. IMPACT EXPERIMENTS

4.1 General

A series of 17 experiments has been carried out which are listed in Table 4.1. Steel was used for the projectile material. This exhibits the same acoustic impedance as sapphire, $Z_{\text{steel}} = 45 \cdot 10^6 \text{ kg/(m}^2\text{s)}$.

#	SHOT No.	TARGET material	PROJECTILE shape	v_0 m/s	■
1	1034	glass	sphere 18 mm dia.	98	
2	1035	sapphire	sphere 18 mm dia.	39	
3	1036	glass	knife edge	55	f
4	1037	glass	knife edge	22	f
5	1038	glass	knife edge	24	
6	1039	glass	bar 10 mm x 10 mm, 49 mm	292	
7	1040	sapphire	bar 10 mm x 10 mm, 43 mm	311	
8	1041	sapphire	knife edge	332	f
9	1042	sapphire	knife edge	328	f
10	1045	glass	bar 10mm x 10 mm, 49 mm	307	
11	1046	glass	bar 10mm x 10 mm, 49 mm	160	
12	1047	glass	cyl. 50 mm dia. 174 mm l., flat nose	20	
13	1048	glass	cyl. 50 mm dia. 174 mm l., spher. nose	13	
14	1049	glass	bar 10 mm x 10 mm, 49 mm	175	
15	1050	sapphire	slab 49 mm dia. 10 mm thick	193	
16	1051	glass	slab 49 mm dia. 10 mm thick	104	
17	1052	sapphire	slab 49 mm dia. 10 mm thick	114	

Table 4.1 List of impact experiments

Attempts have been made to vary the impact area from zero (point or line contact) to a maximum area of 49 mm x 10 mm, which is close to the cannon caliber of 50 mm. A line contact was thought to be preferable instead of a point contact by using a steel sphere. This, however, caused increased difficulties with triggering with the consequence that it worked once in a glass experiment but it failed twice with the sapphire.

The initial impact pressures of the experiments described thereafter is calculated from the impact velocity by eq.(5.9a).

4.2 Description of Impact Experiments

1 Results of 98 m/s experiment on glass, # 1034

The calculated initial pressure in the wave is $\sigma_A = 1.1 \text{ GPa}$, eq.(5.9a). The impactor was an 18 mm diameter steel sphere. The target was a float glass plate 100 mm \times 100 mm \times 10 mm. Figure 4.1 shows a series of 24 high speed photographs of the specimen during impact at 98 m/s. Black regions in the photos are assumed to be cracks, whose surfaces stop light or reflect it and direct it away from the camera lens. Waves of any kind cannot be seen on the pictures which is a consequence of the low wave pressure.

The purpose of this experiment was to test the arrangement and in particular the new trigger which is described in chapter 2 (Fig.2.2). This included also the test of the electric emission probes for wave and fracture detection. The results are discussed in chapter 7.

2 Results of 39 m/s experiment on sapphire, # 1035

The calculated initial pressure in the wave is $\sigma_A = 0.9 \text{ GPa}$. Figure 4.2 shows a series of 24 high speed photographs of the sapphire specimen during impact at 39 m/s. Black regions in the photos are assumed to be cracks, whose surfaces stop light or reflect it and direct it away from the camera lens. No waves can be seen on the pictures. For triggering the camera a pair of contacts had been used as described in detail in [2], page 11. With this trigger device the exact instant of impact is difficult to determine. From the occurrence of damage which is first evident in picture #3 (Fig.4.2.1) it is assumed that this happened shortly before 12.75 μs after trigger.

The location of the shadows at the periphery of the projectile contact region, and their orientation at roughly 45° to the impacted surface suggests that the damage consists of cone cracks, which propagate into the target approximately 15 microseconds, Figure 4.3.

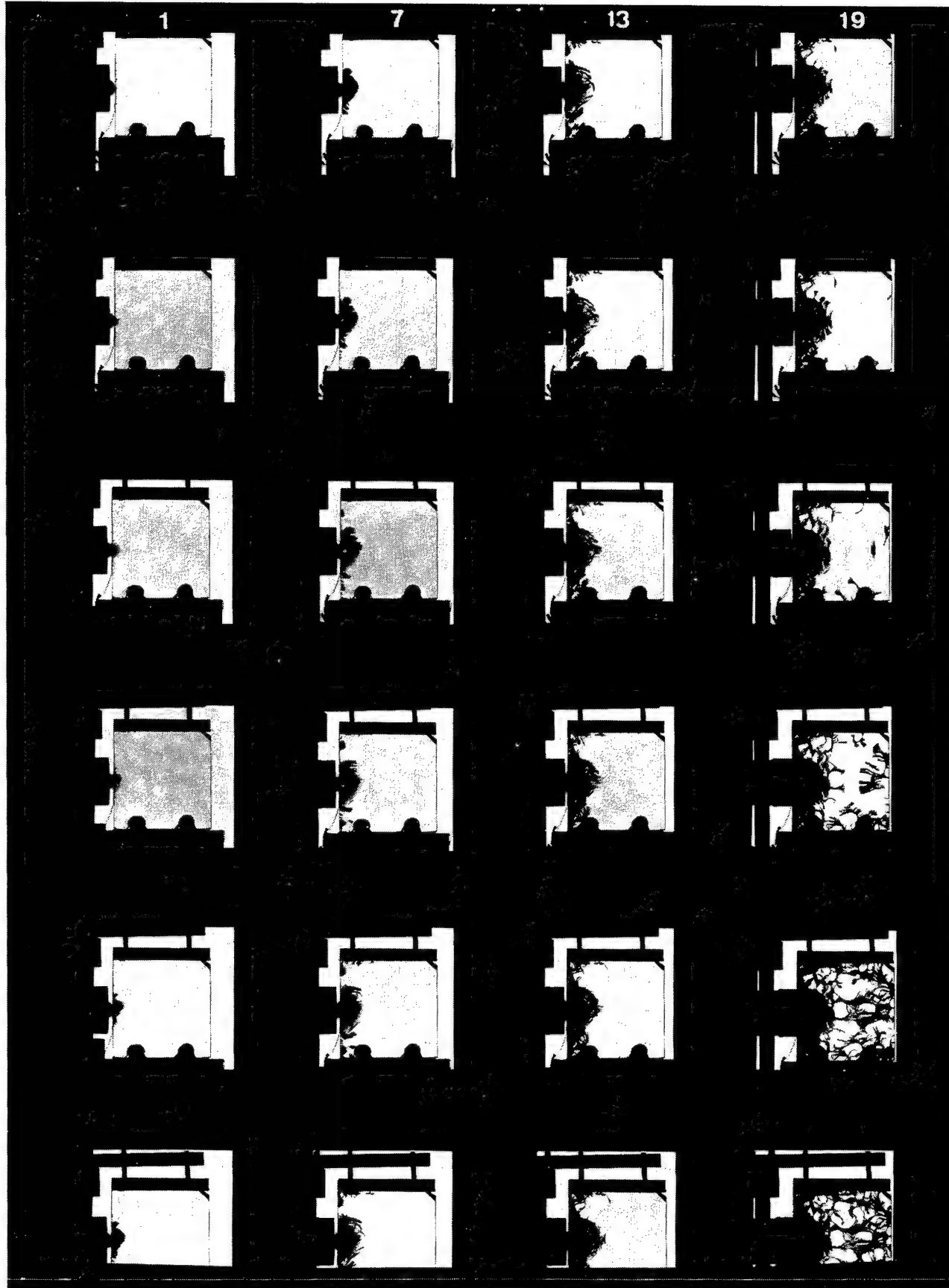


Fig. 4.1 High speed photographs, # 1034

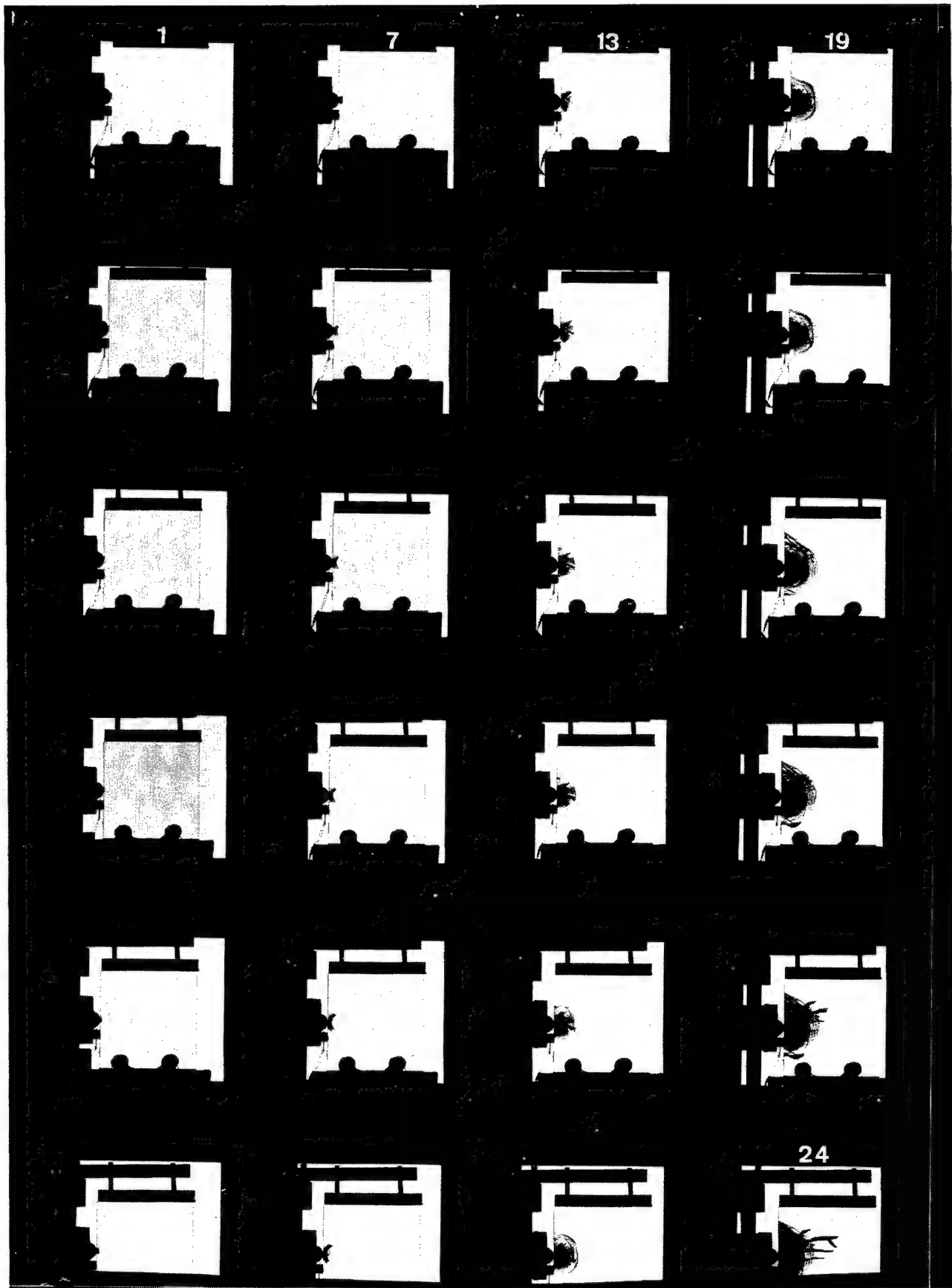


Fig. 4.2 High speed photographs, # 1035

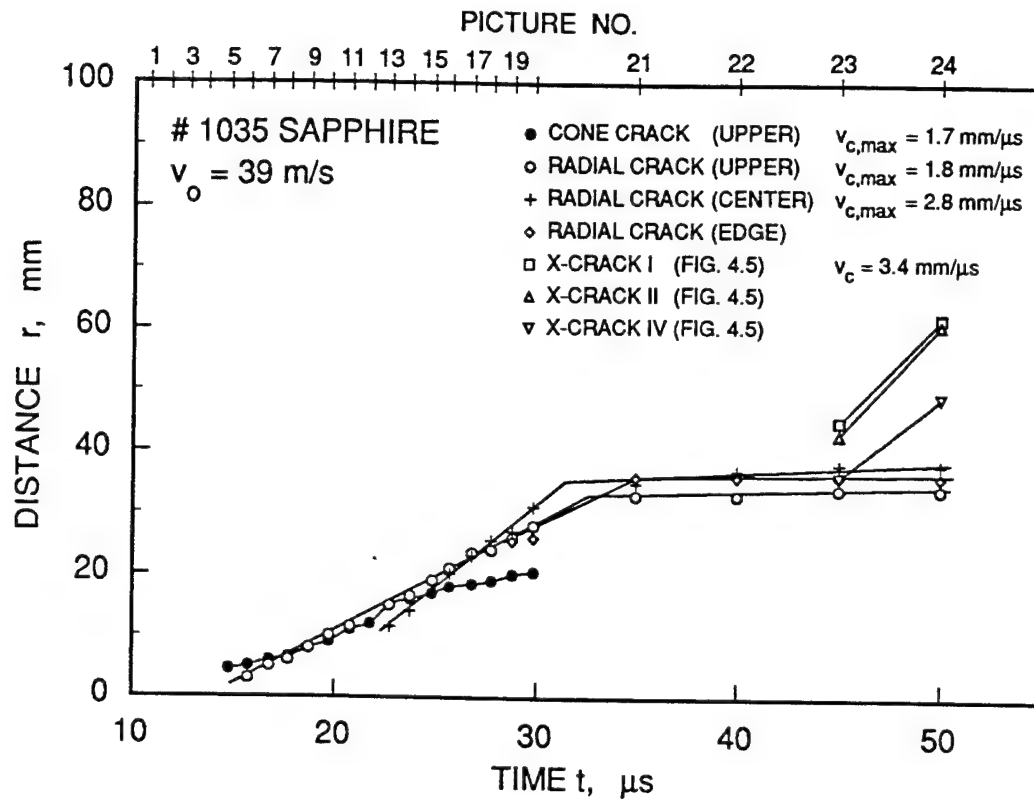


Fig. 4.3 Crack events, # 1035

The cracks seem to start at relatively modest velocities ($\sim 700 \text{ m/s}$), speed up to about 1700 m/s and slow down again. Different parallel, shell-like cracks develop within about 20 microseconds after impact and grow at velocities around 1800 m/s . Because the dominant shell crack (that is approximately parallel to the specimen sides) does not divert much of the light away from the camera lens, its front and details of its surface structure can be seen. The parallel cracks emanating from opposite sides of the impact periphery coalesce with one another in Figure 4.2, #8 and overtake the cone crack front after 7 microseconds, Figure 4.2, #9.

A parallel dominant shell crack appears to be active in Figure 4.2, #19, overtaking the arrested dominant parallel (Figure 4.2, #21) before it arrests. After 33 microseconds all damage processes local to the impact site have ceased; only structural damage continues to occur in the plate far from the impact site.

Several large radial macrocracks emanate from the impact site and propagate in x-direction through the plate to fracture it into several large pieces. The vestiges of these cracks are clearly visible in Figures 4.2, #21 to #24, although only in the last

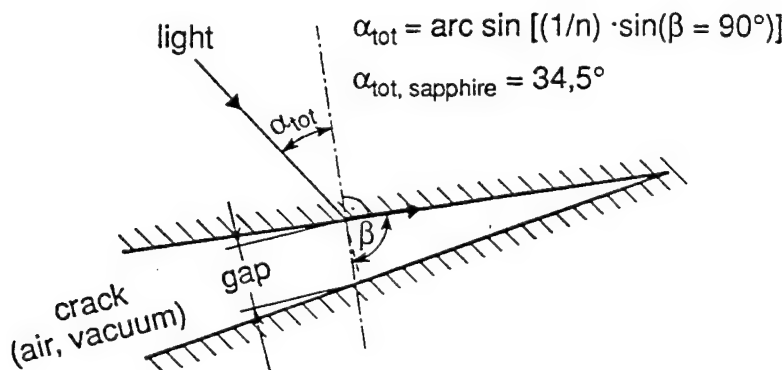
two figures are they sufficiently open to divert enough light to appear black. This "crack opening velocity" has its maximum value at about 3400 m/s (Figures 4.2, #23 and #24). It is believed, therefore, that these cracks are already there at earlier times, however, that there opening is not sufficient for a total light reflection. This means, a most of the light is able to tunnel this narrow gap, although the condition of total reflection is fulfilled (see Fig.4.4) What was called "crack opening velocity" may not be of physical relevance; it is not a crack velocity.

With respect to the crystallographic structure of the sapphire it may be assumed that fracture preferably occurs in cleavage planes. If so, it can be concluded that the angle of the cone crack which appears to be slightly more than 45° from the center line - about 47° - is a crystallographic direction. Another direction could be that of crack II, Figure 4.5. This is about 41° to the center line.

Furthermore, the macrocracks (Fig.4.2, #24, or Fig.4.5) appear very wide which is due to the projection, b, of the crack onto the plane of the film, Figure 4.5. In case these cracks are fully opened the angles listed in Table 4.2 could be the angles of the crack planes to the tile normal. Where lines are not straight, cracks may not have fully opened up to the surface; these conclusions can, therefore, be in parts wrong.

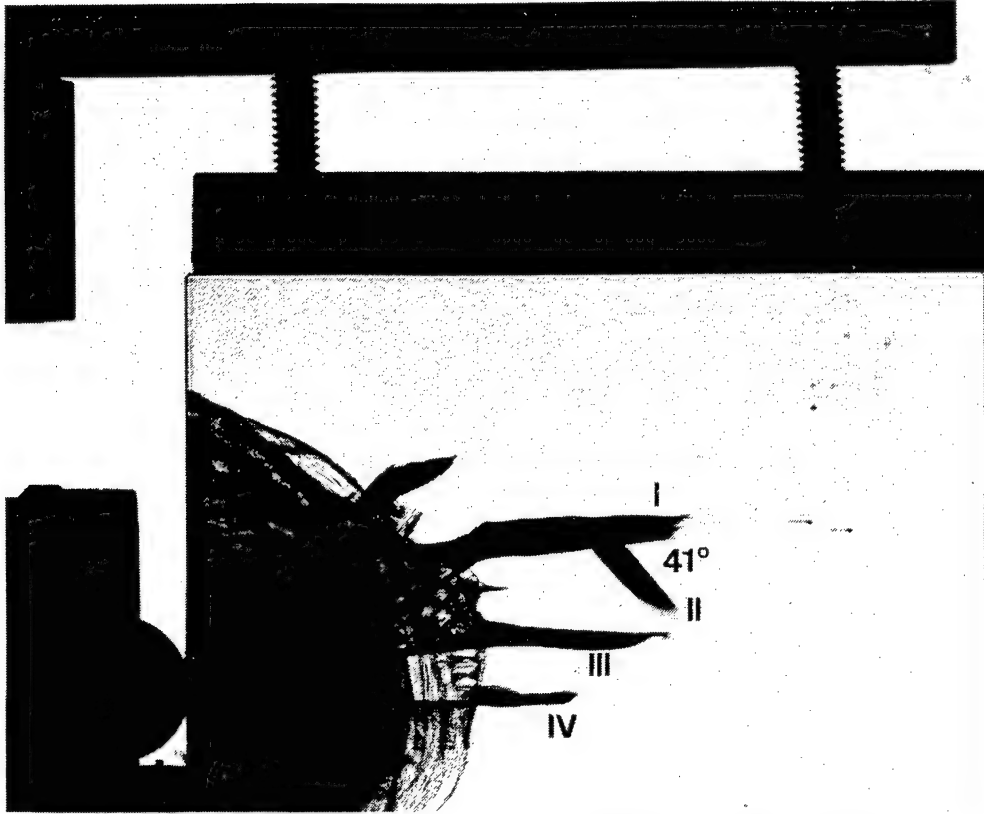
Sapphire: Index of refraction:

$$n_D^{20} = 1.7675$$

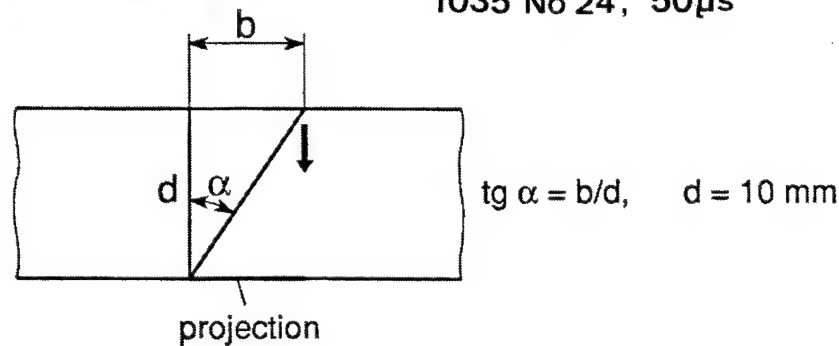


Tunneling occurs if gap < light wave length

Fig. 4.4 Total reflection at a narrow crack



1035 No 24, 50 μ s



	I	II	III	IV
b	4,3	3,0	2,0	3,0
α	23,3°	16,7°	11,3°	16,7°

possible angles of crack planes

Fig. 4.5 Angles of crack planes

3 Results of 55 m/s experiment on glass, # 1036

The calculated initial wave pressure is $\sigma_A = 0.6 \text{ GPa}$. The impactor was a knife-edge steel bar. For triggering the camera a pair of contacts were used as described in detail in [1], page 11. Unfortunately, the trigger failed in this experiment. The purpose was to test the capability of the gun device - which has no guided barrel - to carry out knife-edge experiments. From that point of view the test, although it failed, showed that principally this can be done. The knife-edge arrived at the target in the correct position.

4 Results of 22 m/s experiment on glass, # 1037

The calculated initial wave pressure is $\sigma_A = 0.2 \text{ GPa}$. The impactor was a steel knife-edge. For triggering the camera a pair of contacts were used as described in detail in [2], page 11. Unfortunately, the trigger failed also in this experiment. The purpose was to repeat shot # 1036, i.e., to test the capability of the gun device to carry out knife-edge experiments. Again the knife-edge arrived at the target in the correct position.

5 Results of 24 m/s experiment on glass, # 1038

The calculated initial wave pressure is $\sigma_A = 0.3 \text{ GPa}$. The impactor was a knife-edge steel bar. For triggering the camera a pair of contacts were used as described in detail in [2], page 11. The purpose of the experiment was to repeat shots # 1036 and # 1037 and to test the capability of the gun device to carry out knife-edge experiments. The knife-edge arrived at the target in the correct position.

Due to the very low wave pressure, the optical method could not detect waves within the target. First cracks become visible at 27 μs after trigger. The instant of impact is unknown. Two cracks seem to develop, a radial crack about normal to the surfaces and at least one shell-like crack about parallel to the surfaces. The velocity of the radial is very low in the beginning, about 0.5 $\text{mm}/\mu\text{s}$, but speeds up to 1.2 $\text{mm}/\mu\text{s}$ in the last pictures, at 80 μs . The shell crack becomes slower and arrests when it reaches the surface.

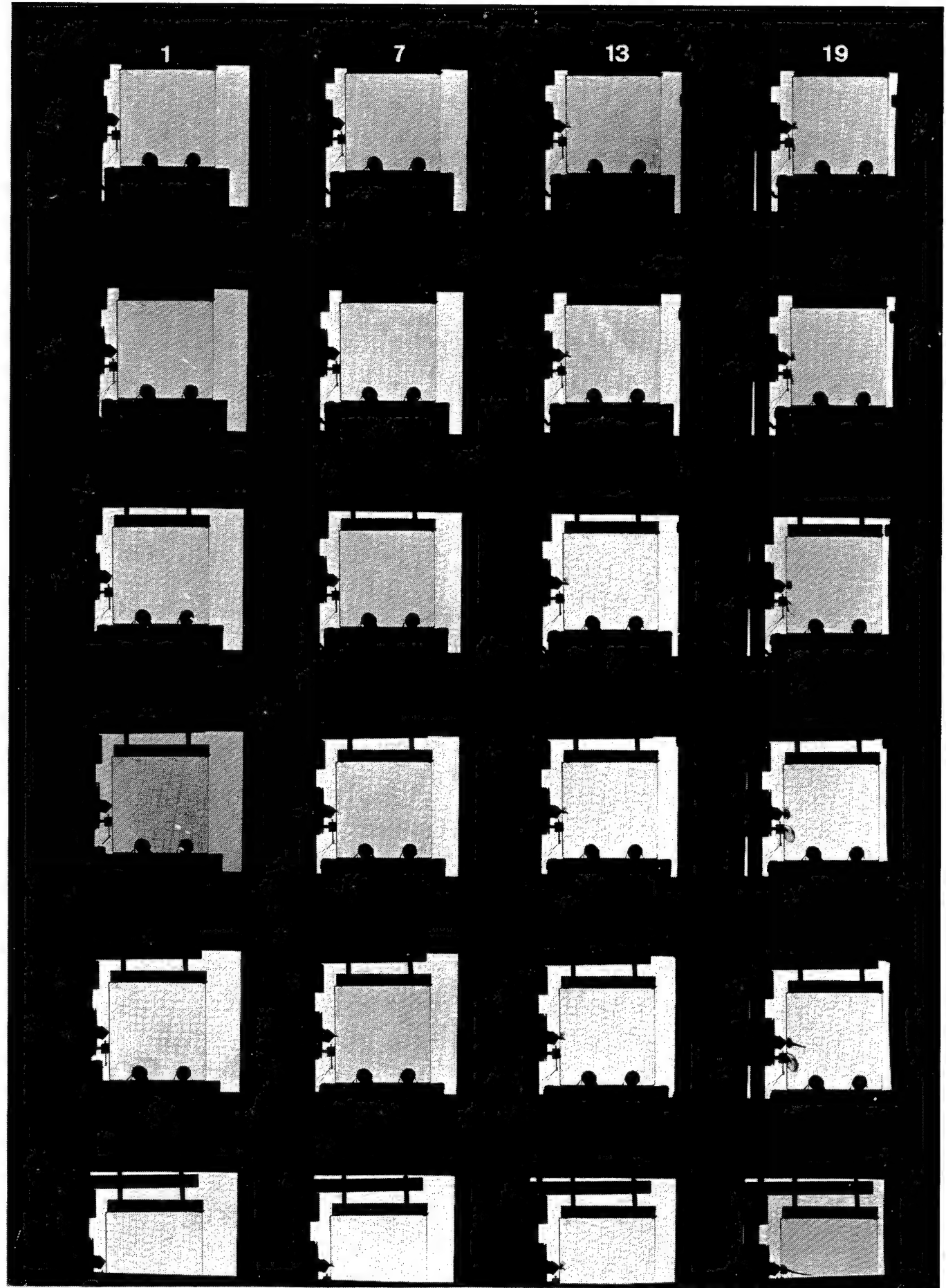


Fig. 4.6 High speed photographs, # 1038

6 Results of 292 m/s experiment on glass, # 1039

The calculated initial wave pressure is $\sigma_A = 3.3 \text{ GPa}$. Waves are photographed preceding the fracture events. The impactor was a 10 mm square and 49 mm long steel bar. Figure 4.7 shows 24 high speed photographs of this experiment. The trigger was that described in chapter 2 (Fig. 2.2).

This experiment shows interesting wave and fracture phenomena. Eight of many visible crack nucleations could be used to determine a damage velocity, $v_D = 4.3 \text{ mm}/\mu\text{s}$. Because of the 10 mm thick projectile bar the pressure pulse has a duration of 3.5 μs which results in a pulse length of about 20 mm in glass. The photographs show this pulse with the leading front and the trailing edge and a front in between, which is believed to be due to wave splitting (see sect. 5.4). The intermediate second front follows the first front after $X = 14.5 \text{ mm}$. With the method described in section 5.4, eq. 5.8, the shear wave velocity can be calculated from this distance: $c_L = 1.76 \cdot c_T$ which results in $c_T = 3330 \text{ m/s}$.

The rear pulse edge appears much thicker than the two wave fronts, Fig. 4.9. This is a consequence of this part of the pulse having been travelled twice through the impactor bar. In steel the edge splits up into an elastic part and a slower plastic part and is reflected at the rear impactor edge, thereby undergoing a fan-out effect.

Figure 4.9 shows also material being ejected at the impactor edges. The also seen air blast wave which originates from the compressed air at the impact site has a radius of more than 1 cm in this picture which corresponds to an average expansion velocity of about 800 m/s, which is almost three times the speed of sound in air. The material's velocity is less but still supersonic as can be concluded from the attached air wave.



Fig. 4.7 High speed photographs, # 1039

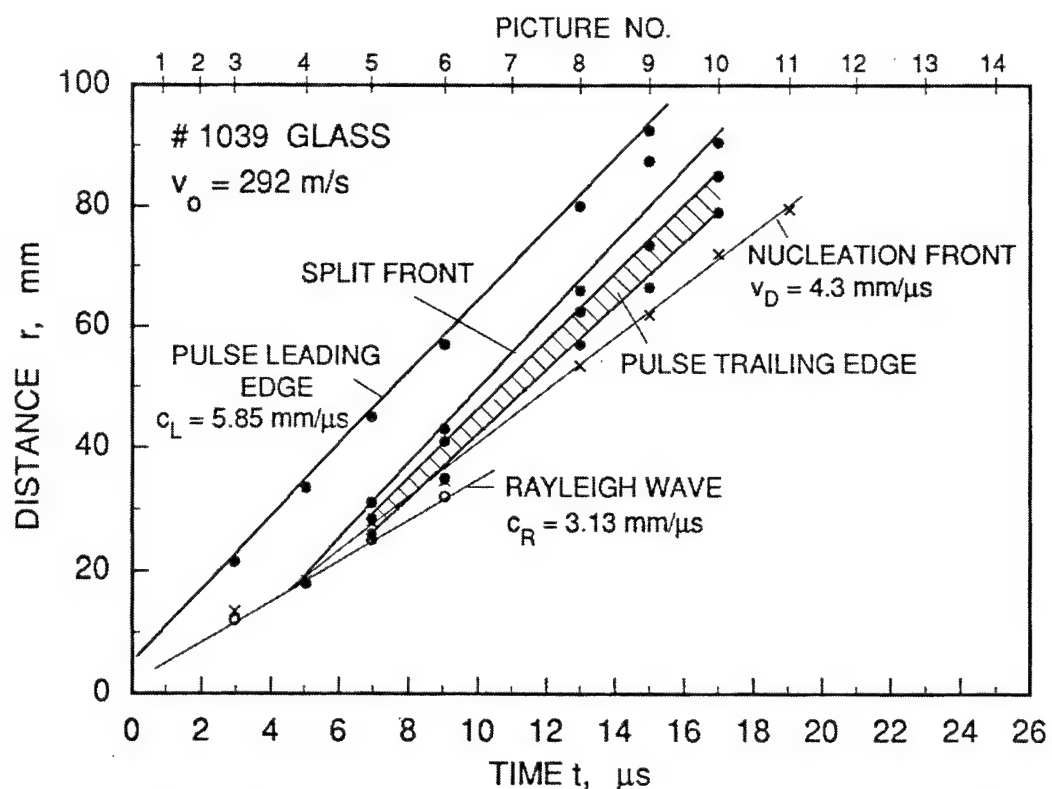


Fig. 4.8 Space-time diagram of waves and fractures, # 1039

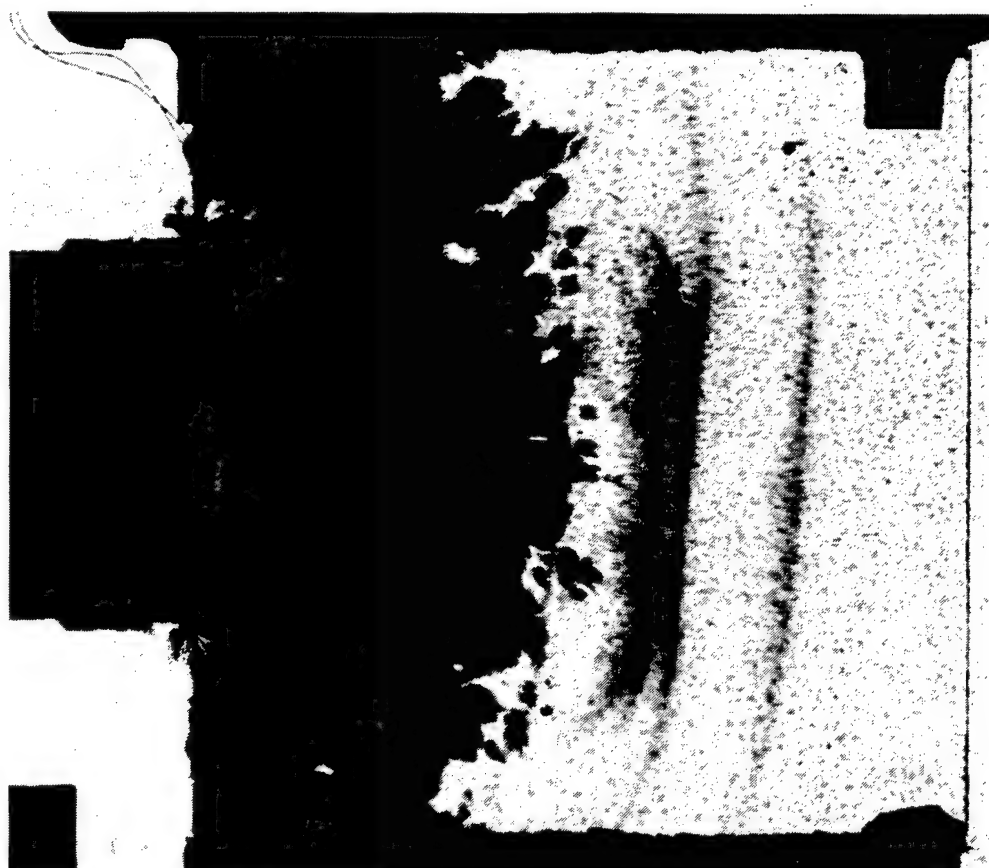


Fig. 4.9 Wave details and fracture nucleation in the glass target, # 1039, picture # 8, at 13.00 μs

7 Results of 311 m/s experiment on sapphire, # 1040

The calculated initial wave pressure is $\sigma_A = 7.0 \text{ GPa}$. Waves are photographed preceding the fracture events. The impactor was a 10 mm square and 49 mm long steel bar. Figure 4.10 shows 24 high speed photographs of this experiment. The trigger was that described in chapter 2 (Fig.2.2).

Fracture events in this experiment are about the same as before. Primary fracture events are again finished within about 10 microseconds, which is the time the pressure wave front needs to travel through the target slab. The first cracks seen on pictures #1 ff, (Fig.4.10) are cone cracks originating from the impactor edges, exhibiting a velocity of $5.4 \text{ mm}/\mu\text{s}$. Radial cracks cannot be seen. Again a narrow black volume in front of the impactor showing a fuzzy front may represent the Mescall zone. A sort of cone cracks occur under the same angle as before nucleated at the free parts of the impacted edge of the target. Reason for nucleation is presumably the primary shear wave travelling along the edge. The velocity the nucleation sites move along the edge is about $6 \text{ mm}/\mu\text{s}$.

Edge cracks also appear at the lower and upper edges which are in contact with a soft rubber sheet. They are seen first in picture #9 after 6.15 microseconds. Again these nucleations appear when the transverse wave emanated from the impact site meets the edge. Edge crack velocity was determined to about $5 \text{ mm}/\mu\text{s}$.

Inside nucleations are identified in picture #6, 4.65 microseconds after impact. The nucleation front moves with a damage velocity, $v_D = 10.1 \text{ mm}/\mu\text{s}$, Average nucleated crack velocities are $4.0 \text{ mm}/\mu\text{s}$ in forward direction and $3.6 \text{ mm}/\mu\text{s}$ in backward direction.

8 Results of 332 m/s experiment on sapphire, # 1041

and

9 Results of 328 m/s experiment on sapphire, # 1042

With the two of these experiments high velocity knife-edge tests were planned. Both failed because of the difficult trigger situation.

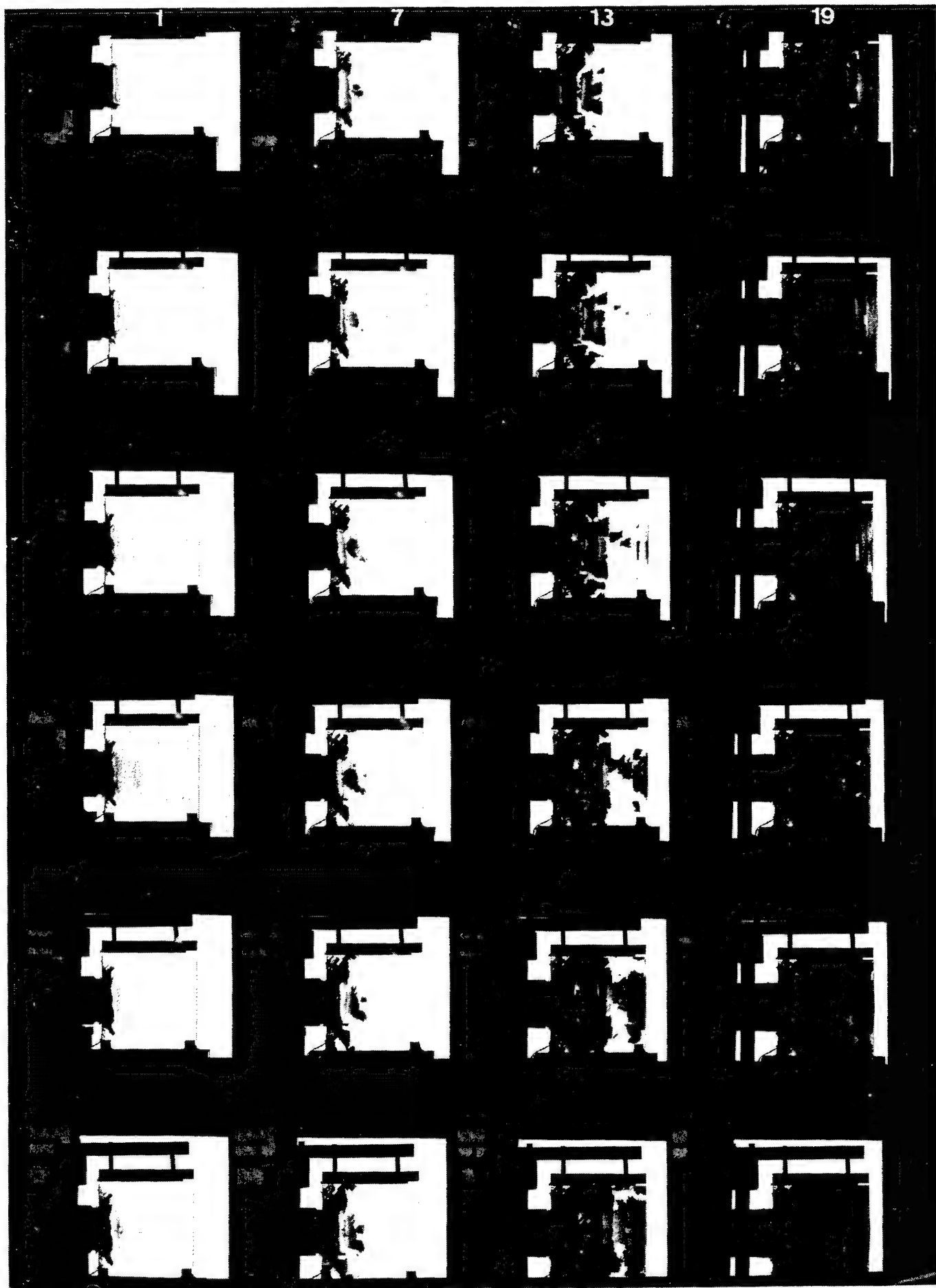


Fig. 4.10 High speed photographs, # 1040

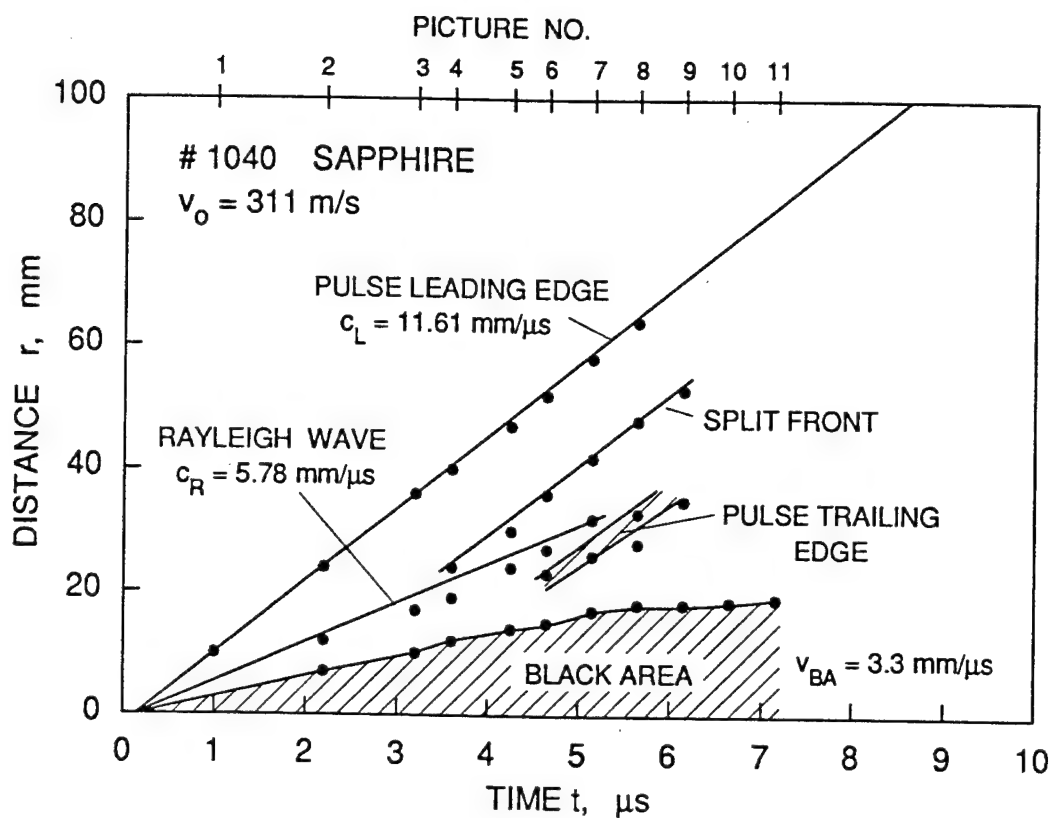


Fig.4.11 Space-time diagram of waves, # 1040

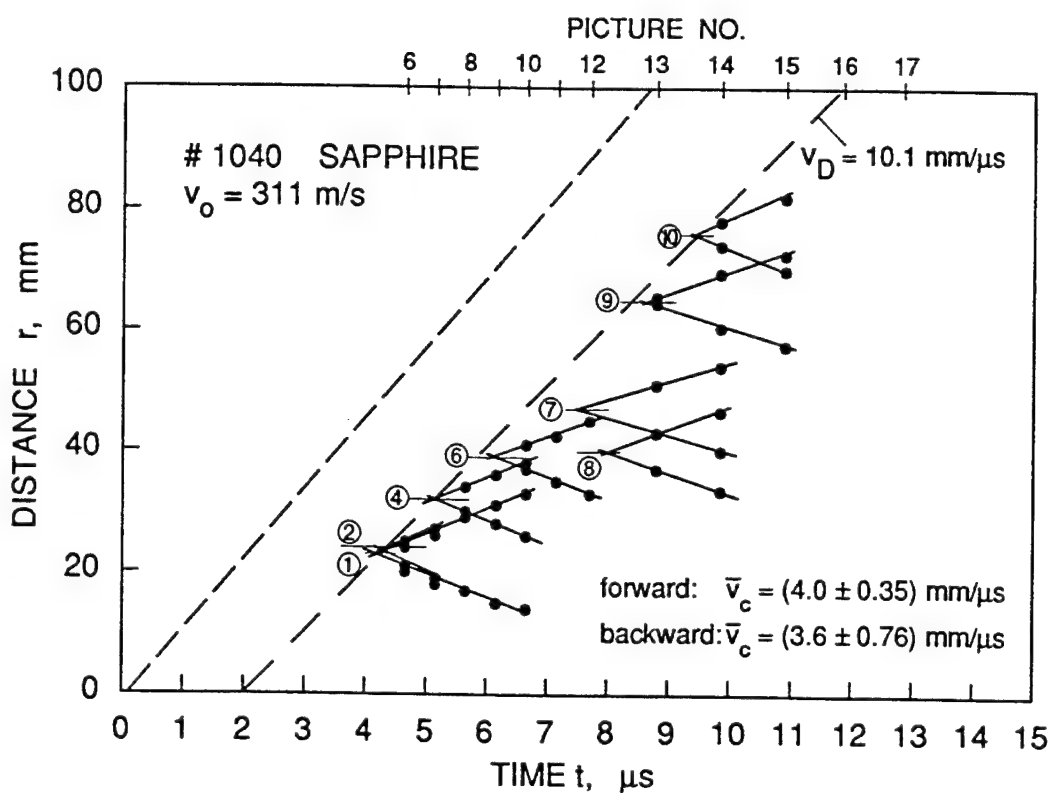


Fig.4.12 Space-time diagram of fractures, # 1040

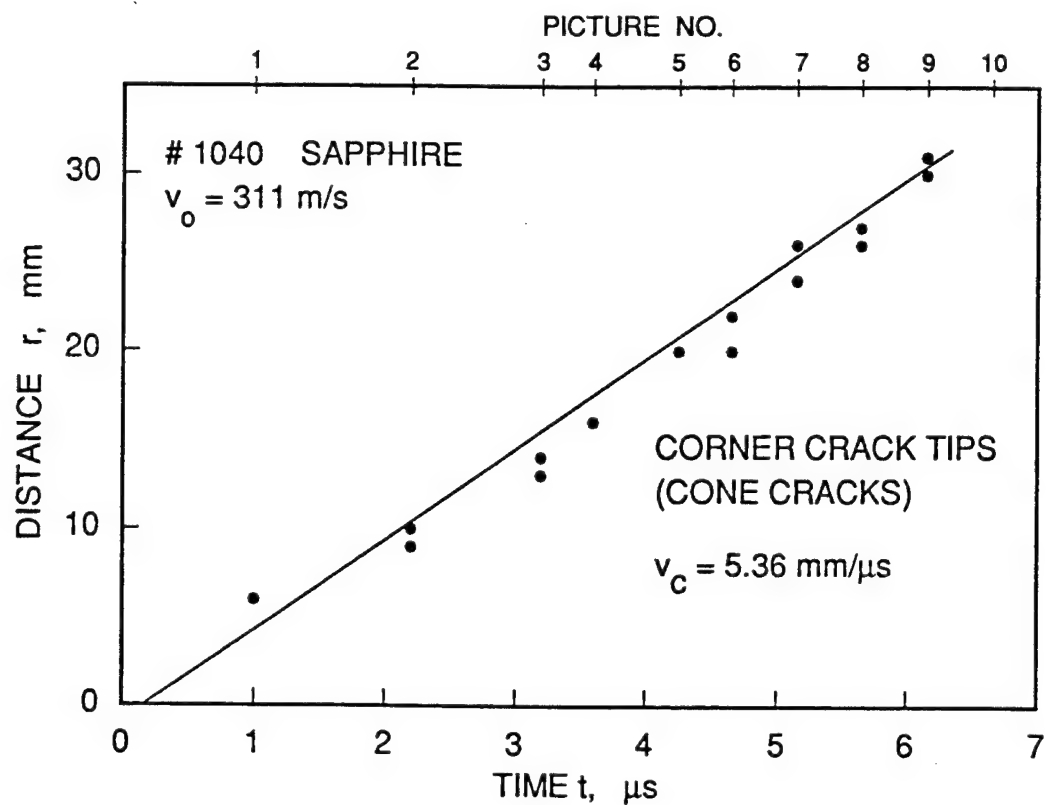


Fig. 4.13 Cone crack diagram, # 1040

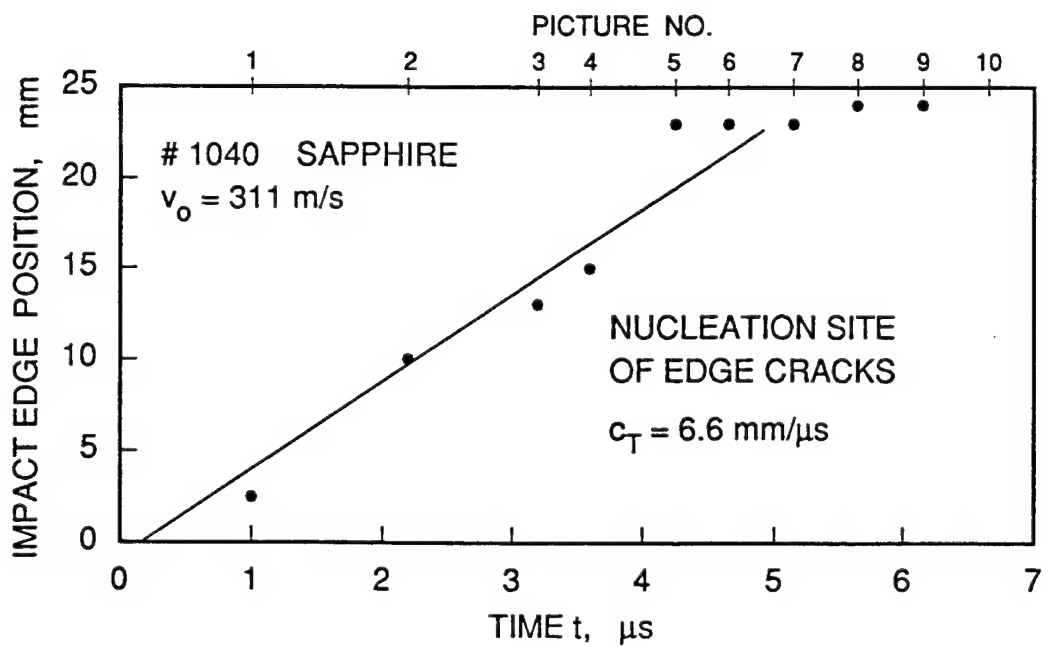


Fig. 4.14 Edge nucleation movement, # 1040

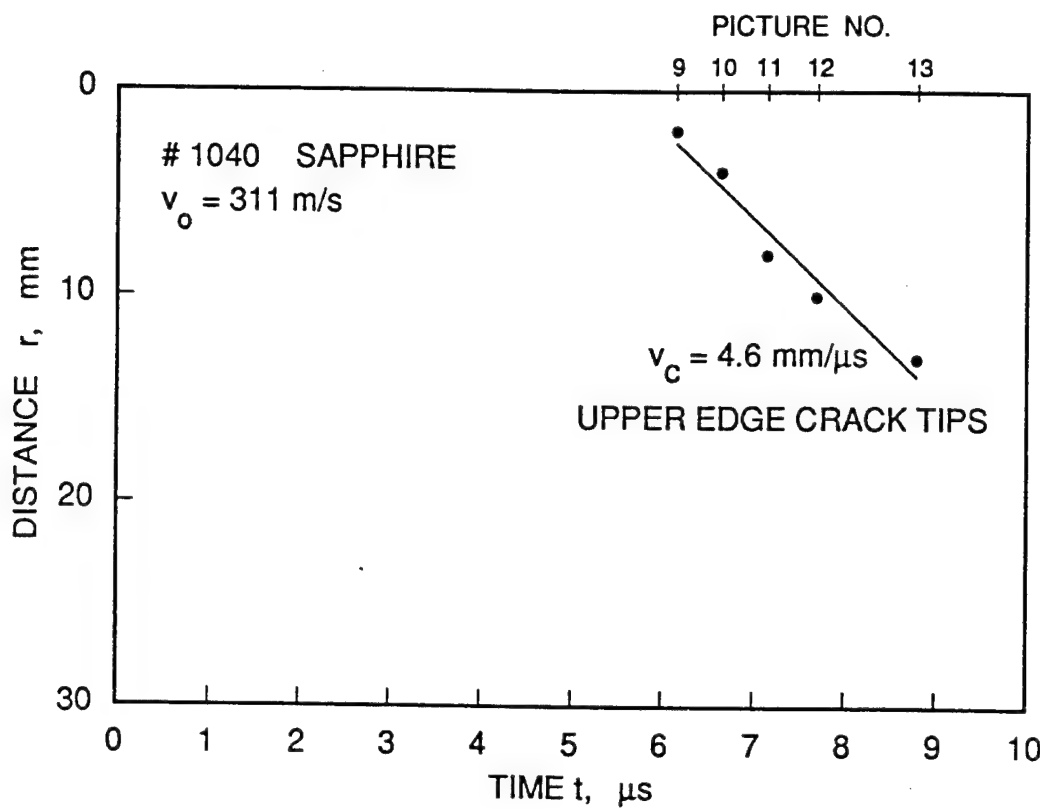


Fig. 4.15 Edge crack velocity, # 1040

10 Results of 307 m/s experiment on glass, # 1045

The calculated initial wave pressure is $\sigma_A = 3.5 \text{ GPa}$. The impactor was a 10 mm square and 49 mm long steel bar. The high speed camera has not been used in this experiment. The purpose of this experiment was an attempt to catch at least parts of a target which was wrapped twofold by tape. Additionally, a funnel-shaped debris catching device was constructed. This was fixed at the impact edge in order to catch the backwards ejected material. A 52 mm hole was provided to let the projectile pass to the impact site. Parts of the funnel inside was covered with different grease, part with cement. It was hoped that the fine debris was collected and that even the origin of the particles could be reconstructed. A high impact velocity was chosen because there was some doubt whether a Mescall zone can be produced in that sense described in [4], see sect.7.3.

Even though the projectile weighs little more than 100 g only, the kinetic energy is considerable when v_0 is 307 m/s: $E_{\text{kin}} \sim 5 \text{ kJ}$. The result was that neither a part of the target was recovered nor did the funnel work. Everything was destroyed and it was

concluded that for a successful debris catching method further development work would be necessary.

Nevertheless, three more tests have been carried out with glass targets without camera in order to vary these catching devices or to study large fragment target disintegration:

11 A 160 m/s experiment on glass, # 1046

The calculated initial wave pressure is $\sigma_A = 3.3$ GPa. The impactor was a 10 mm square and 49 mm long steel bar (untreated mild steel).

12 A 20 m/s experiment on glass, # 1047

The calculated initial wave pressure is $\sigma_A = 0.23$ GPa. The impactor was a steel cylinder with flat nose.

13 A 13 m/s experiment on glass, # 1048

The calculated initial wave pressure is $\sigma_A = 0.15$ GPa. The impactor was a steel cylinder with spherical nose, $r = 25$ mm.

14 Results of 175 m/s experiment on glass, # 1049

The calculated initial wave pressure is $\sigma_A = 2.0$ GPa. Accordingly, waves are photographed preceding the fracture events. The impactor was a 10 mm square and 49 mm long steel bar. Figure 4.13 shows 24 high speed photographs of this experiment. The trigger was that described in chapter 2 (Fig.2.2).

This experiment is very similar to the one of # 1039. It shows similar wave and fracture phenomena. Again the 10 mm thick projectile bar gave rise to a pressure pulse duration of 3.5 μ s. This time, however, the tile thickness was 8 mm only instead of 10 mm which led to a closer distance of $X = 11$ mm of the two primary wave fronts due to the splitting effect (sect.5.4).

1049

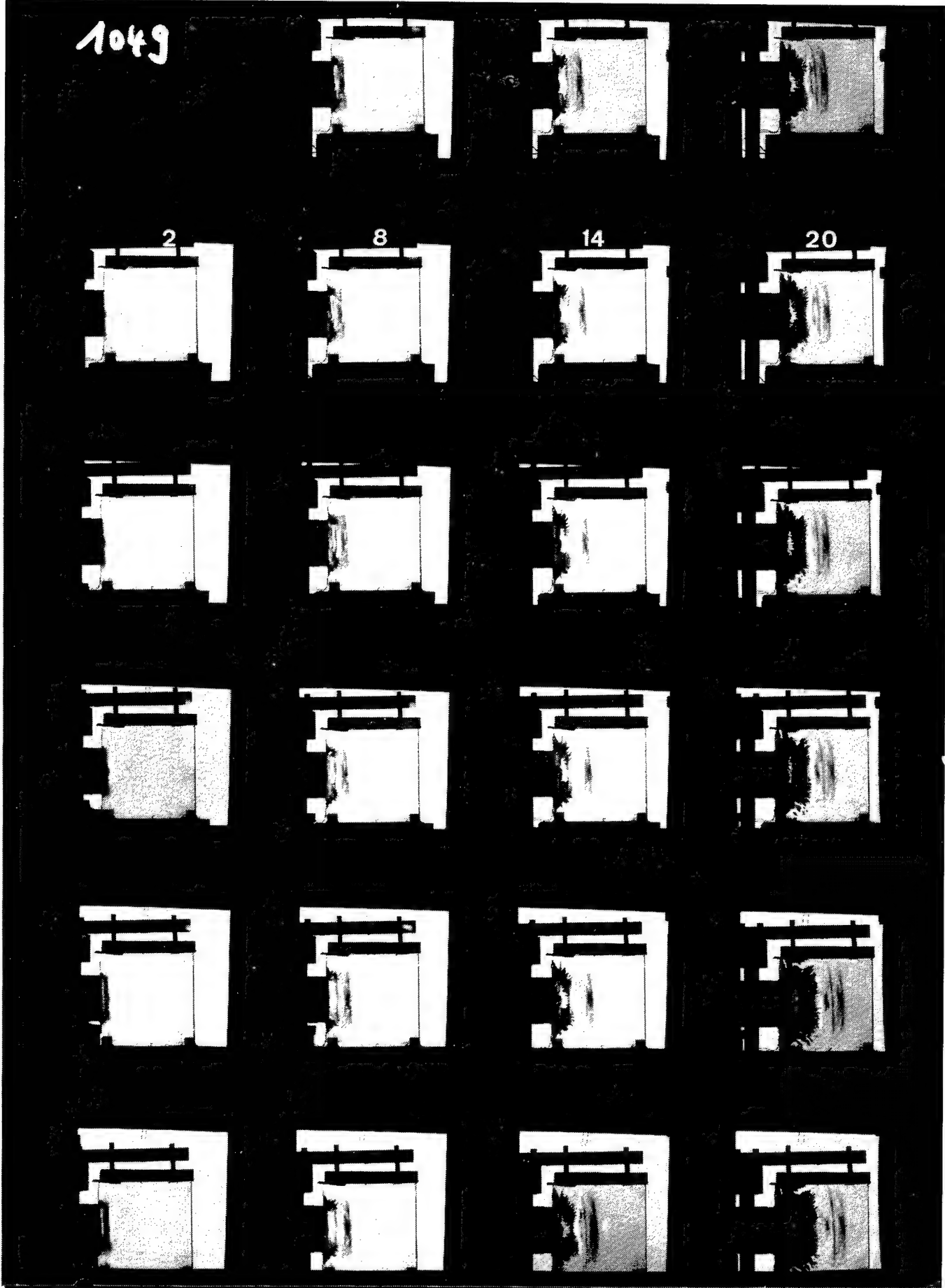


Fig. 4.16 High speed photographs, # 1049

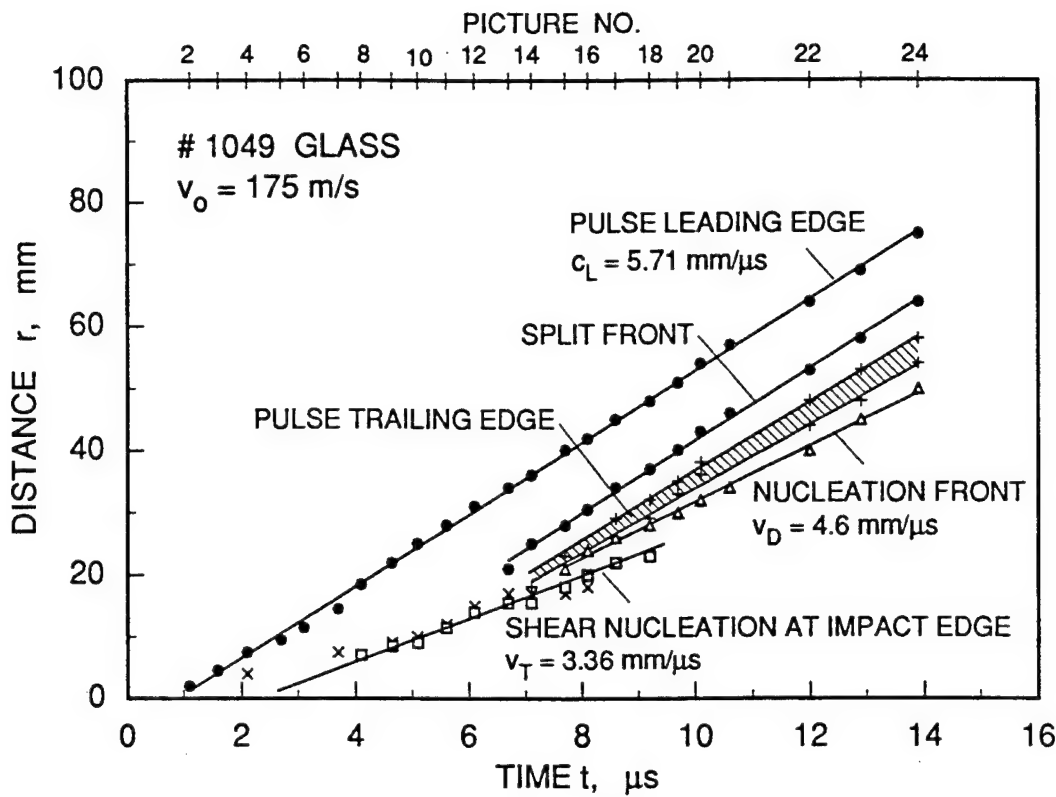


Fig. 4.17 Space-time diagram of waves and fractures, # 1049

15 Results of 193 m/s experiment on sapphire, # 1050

The calculated initial wave pressure is $\sigma_A = 4.3 \text{ GPa}$. Accordingly, waves are photographed preceding the fracture events. The impactor was a steel slab 10 mm thick and 49 mm diameter. Figure 4.4.1 shows 24 high speed photographs of this experiment. The trigger was that described in chapter 2 (Fig.2.2).

Waves are shown in the diagram of Fig.4.19. The primary pressure wave front (longitudinal wave) splits into a sequence of three subsequent fronts separated about 15 mm or 1.5 μs . A similar phenomenon has been investigated earlier with somewhat different experiments by Beinert [6] and is described here in section 5.4, Wave Phenomena. The pressure wave velocity is measured in this experiment to $c_L = 11.4 \text{ mm}/\mu\text{s}$, an average Rayleigh wave velocity is determined to $\bar{c}_R = 5.7 \text{ mm}/\mu\text{s}$.

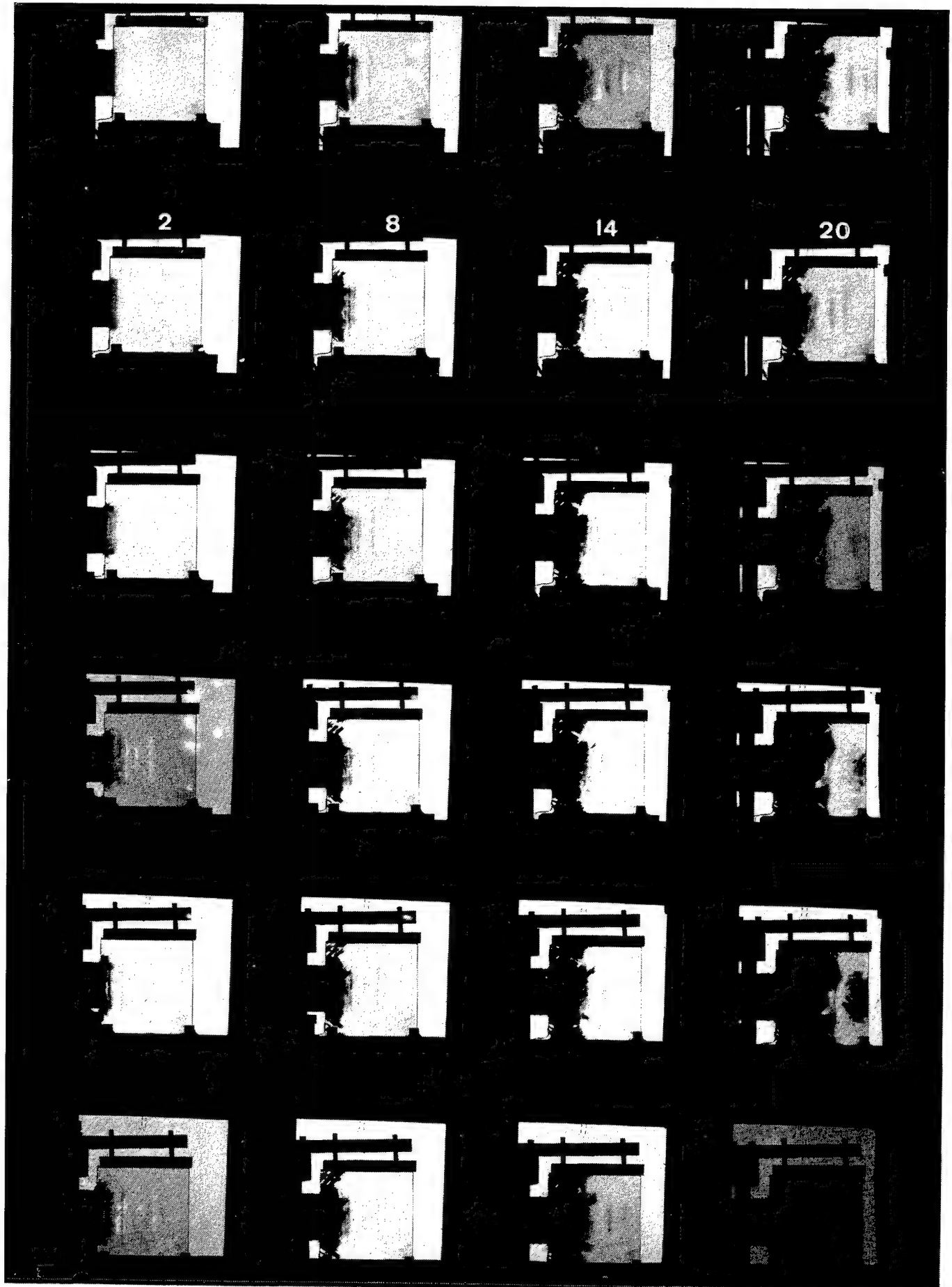


Fig. 4.18 High speed photographs, # 1050

Fracture events are more complex in this experiment. Primary fracture events are finished within about 10 microseconds, about the time the pressure wave front needs to travel through the target slab. The first cracks seen on pictures #1 ff, Fig.4.18, are again edge cracks originating from the impactor edges, showing also precursor vestiges as in the experiment # 1052. A volume in front of the impactor appears black and could possibly be the Mescall zone. Next are sort of cone cracks under the same angle as before nucleated at the free parts of the impacted edge. Nucleation reason is presumably the arrival of the transversal wave at the nucleation site. The velocity these nucleation sites travel along the edge is roughly $6 \text{ mm}/\mu\text{s}$. Edge cracks do also appear at the lower and upper edges which are in contact with a soft rubber sheet. They are seen first in picture #8 after 4.1 microseconds. Again, these nucleation loci travel with transverse wave velocity, this time determined to $6.24 \text{ mm}/\mu\text{s}$, Fig.4.20.

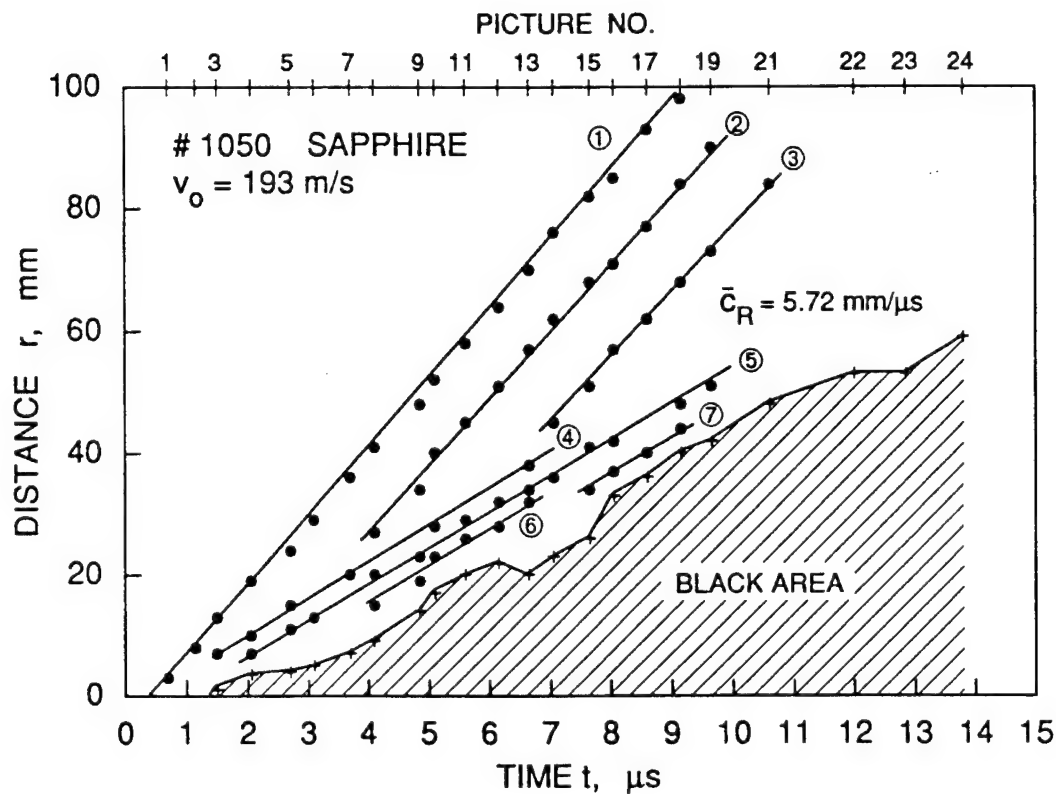


Fig. 4.19 Space-time diagram of waves, # 1050

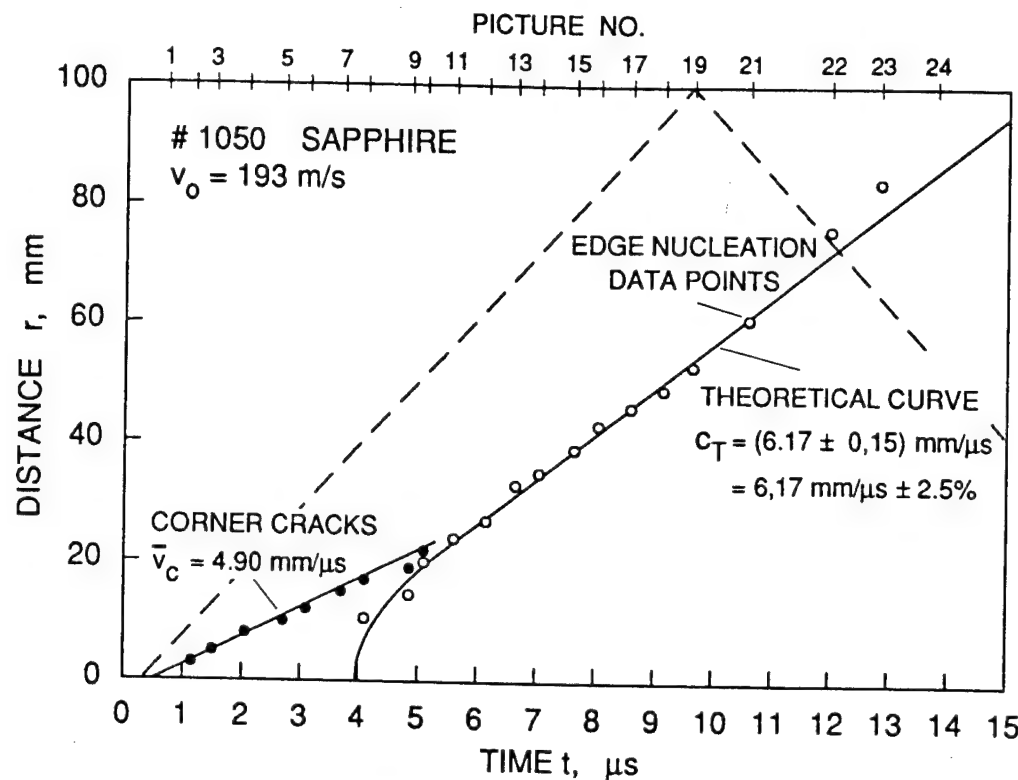


Fig. 4.20 Edge crack nucleation effects, # 1050

Inside nucleations may occur shortly after impact. They cannot clearly be identified, although there are indications from picture #3 on. Clearly to distinguish inside nucleations appear first in picture #15, 7.65 microseconds after impact. About four of them can be used to evaluate a damage velocity, $v_D = 7.0 \text{ mm/}\mu\text{s}$, Fig.4.21. The cracks propagating from these nuclei do not exhibit very uniform crack velocities.

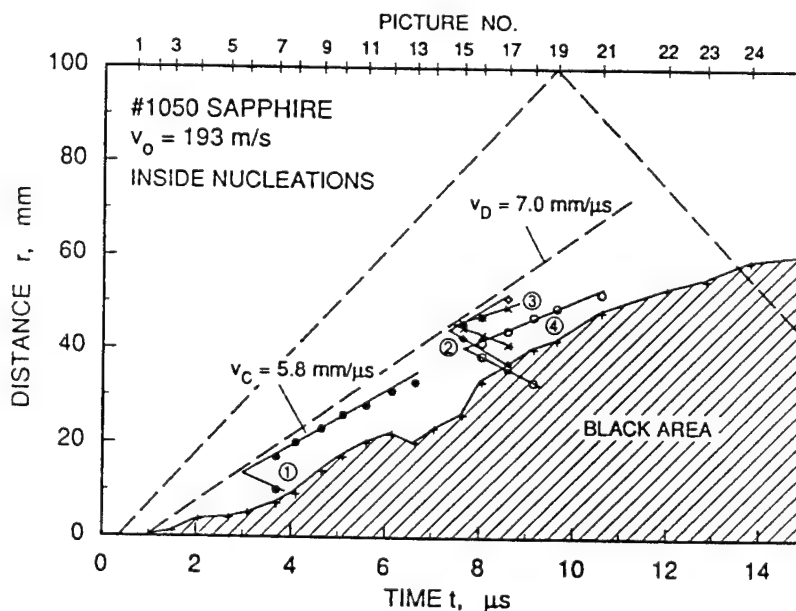


Fig. 4.21 Space-time diagram of inside nucleations, # 1050

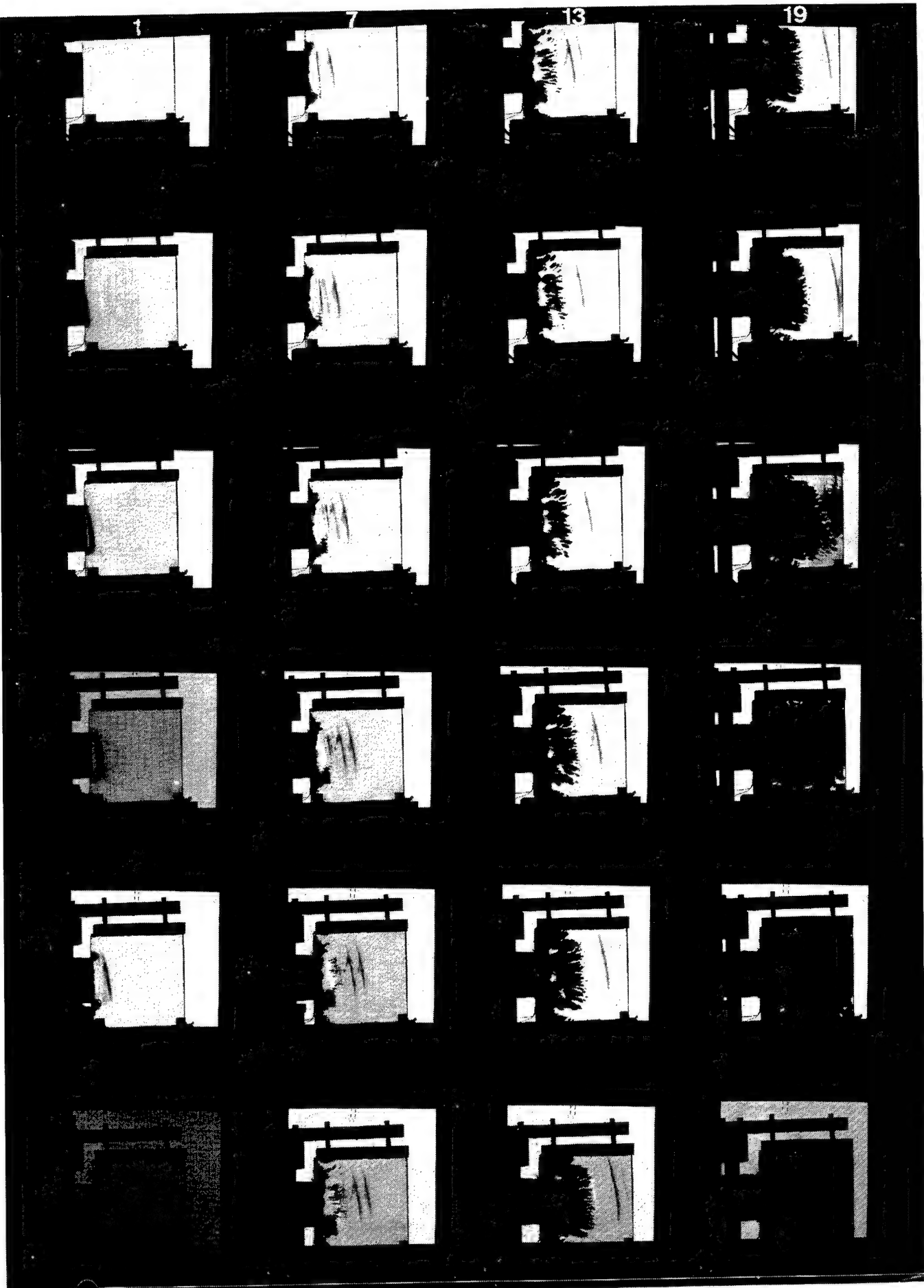


Fig. 4.22 High speed photographs, # 1051

16 Results of 104 m/s experiment on glass, # 1051

The calculated initial wave pressure is $\sigma_A = 1.2 \text{ GPa}$. Waves are photographed preceding the fracture events. The impactor was a 10 mm thick and 49 mm diameter steel slab. Figure 4.22 shows 24 high speed photographs of this experiment. The trigger was that described in chapter 2 (Fig.2.2).

This experiment is similar to those of # 1039 and # 1049. It shows similar wave and fracture phenomena. The tile thickness again was 8 mm which results in a distance of $X = 11 \text{ mm}$ of the two primary wave fronts due to the splitting effect (sect.5.4). This experiment was considered to be a pre-test for the following sapphire test. The projectile slab thickness was 10 mm which should have generated a pressure pulse duration of 3.5 μs . The glass tile, however, was in a relatively crude state with an uneven impact surface. This can be seen with the first wave front which is not as thin as usual. This leads also to a longer (25 mm) pulse length because both of the two edges have a reduced slope. There was also a tilt with the impacted edge so that the lower projectile corner hit the target first. This resulted in a tilted wave movement. Over six pictures a Rayleigh wave can be identified. Its velocity is $c_R = 3.1 \text{ mm}/\mu\text{s}$. The front of many nucleations form a damage velocity of $v_D = 3.3 \text{ mm}/\mu\text{s}$, Fig.4.23.

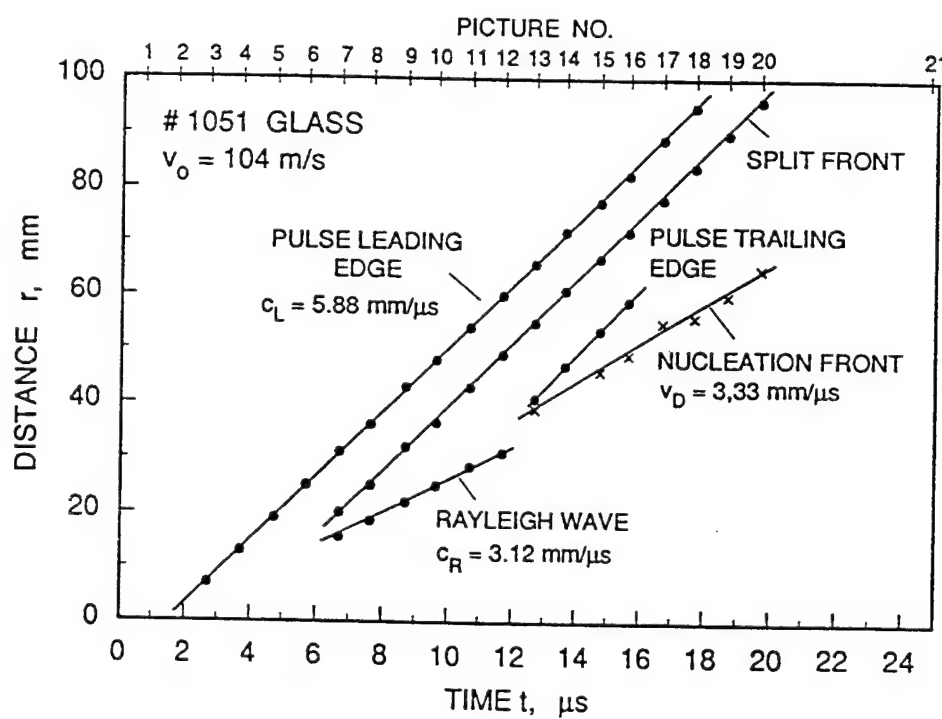


Fig. 4.23 Space-time diagram of waves and fractures, # 1051

17 Results of 114 m/s experiment on sapphire, # 1052

The calculated initial wave pressure is $\sigma_A = 2.6 \text{ GPa}$. Accordingly, waves are photographed preceding the fracture events. The impactor was a steel slab 10 mm thick and 49 mm in diameter. Figure 4.24 shows 24 high speed photographs of this experiment. The trigger was that described in chapter 2, Fig.2.2. The tilted wave front in the first pictures reveals a poor alignment. From the first pictures it was calculated that the misalignment was 0.16 mm corresponding 3.2 mrad. This caused an impact delay of 1.4 μs between the upper and lower projectile corner.

A 45° crack seems to begin instantaneously with edge contact at the lower edge, pictures #2, #3, Fig.4.24. This seems to be one tilted crack only which is concluded from the appearance of the crack front. The projection varies from about 3 to 5 mm which corresponds to angles between about 17° and 27° . Most surprising is a vestige in pictures #3 to #14 with the shape of the later crack. A continuous transition from a shadow to the dark crack suggests something similar as was observed in # 1035, the crack is generated very early but not visible due to an insufficient crack opening (Fig.4.4). These edge cracks show a slight curvature and do, therefore, not seem to be crystallographic cracks.

Within these edge cracks in the central part a crack system seems to develop with a crack propagation direction in x-direction, different parts, however, with different velocities.

A kind of spalling which is also seen in most of the experiments is particularly well formed here in #18 to #21.

It can be recalculated from wave progress that the instant of impact took place 0.65 μs after trigger which coincides with the first picture. Waves which can be observed on pictures are plotted in diagram Fig.4.25. This is the primary longitudinal wave at two places, the lower edge and at the centre line (for different positions waves separate in the diagram due to the misalignment) and one or two following Rayleigh waves. The pressure wave velocity is determined to $c_L = 11.7 \text{ mm}/\mu\text{s}$ and the Rayleigh wave velocity to $c_R = 6.0 \text{ mm}/\mu\text{s}$.

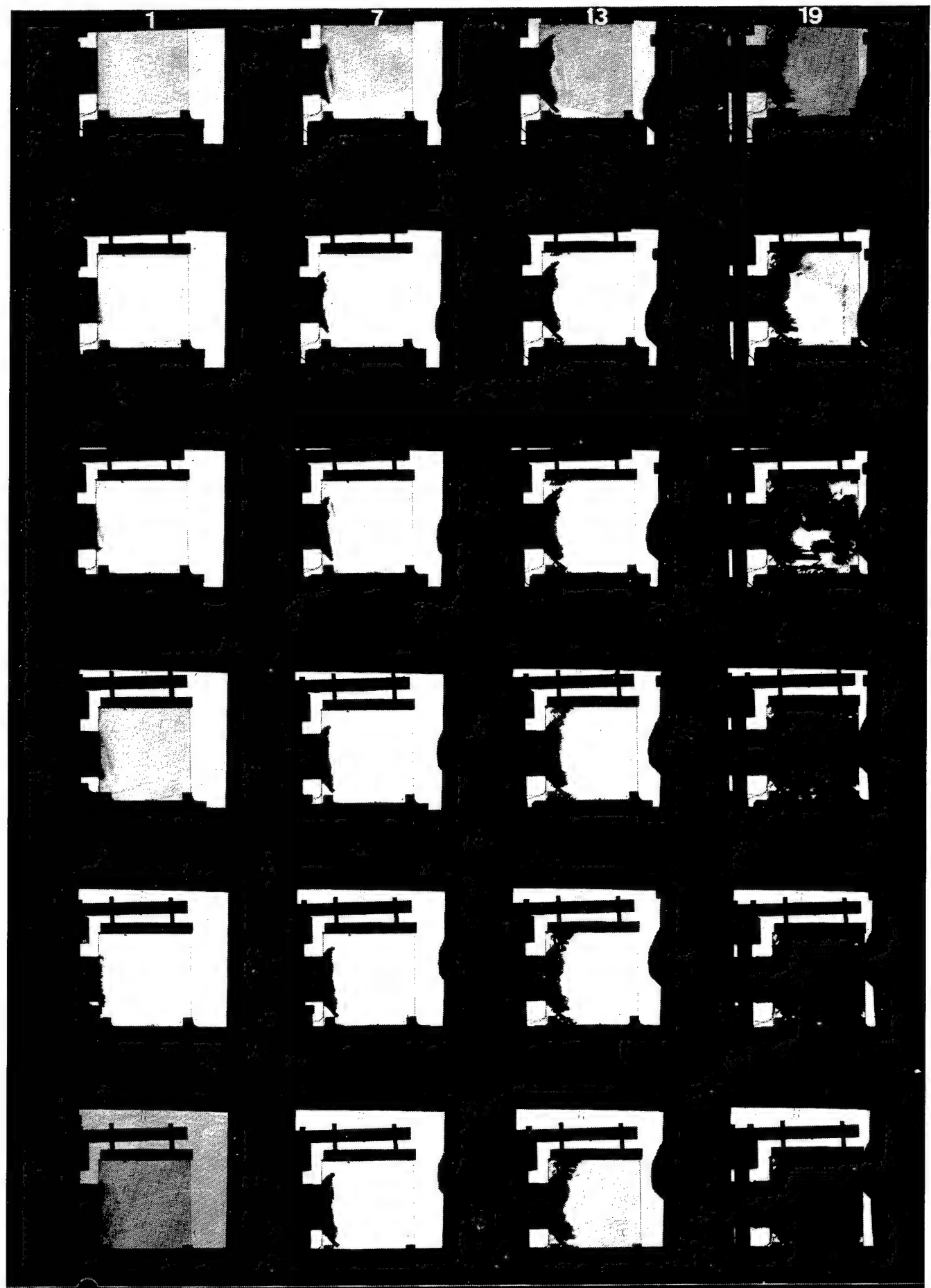


Fig. 4.24 High speed photographs, # 1052

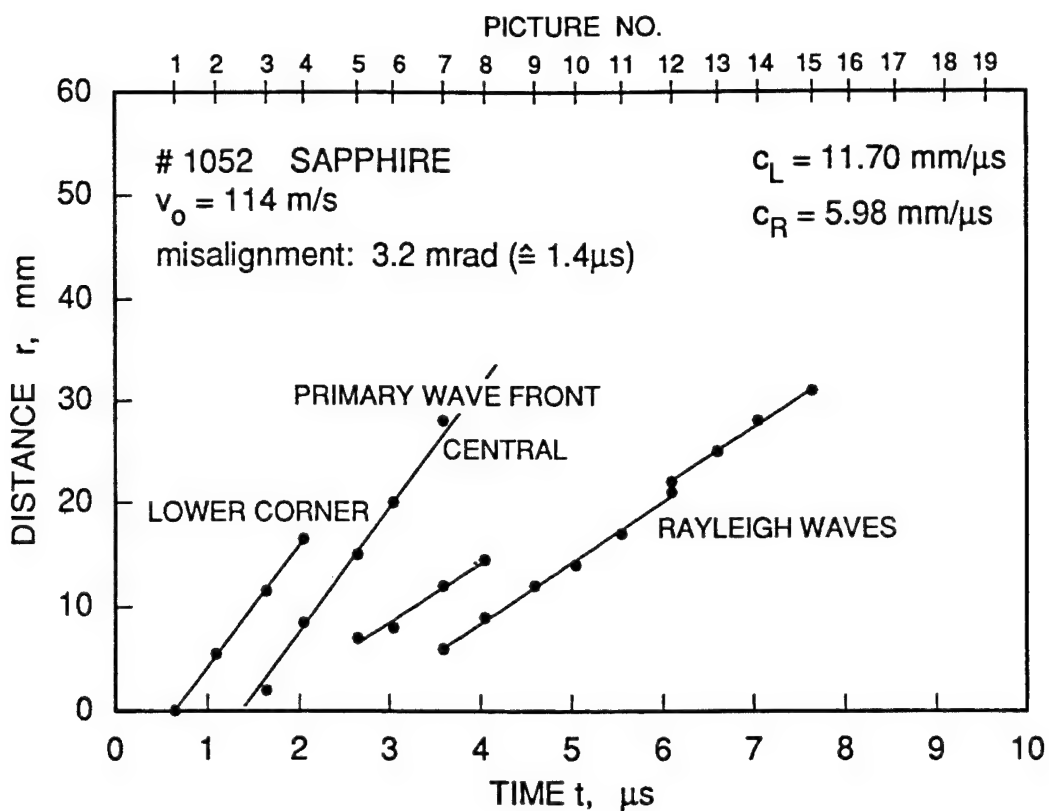


Fig. 4.25 Space-time diagram of waves, # 1052

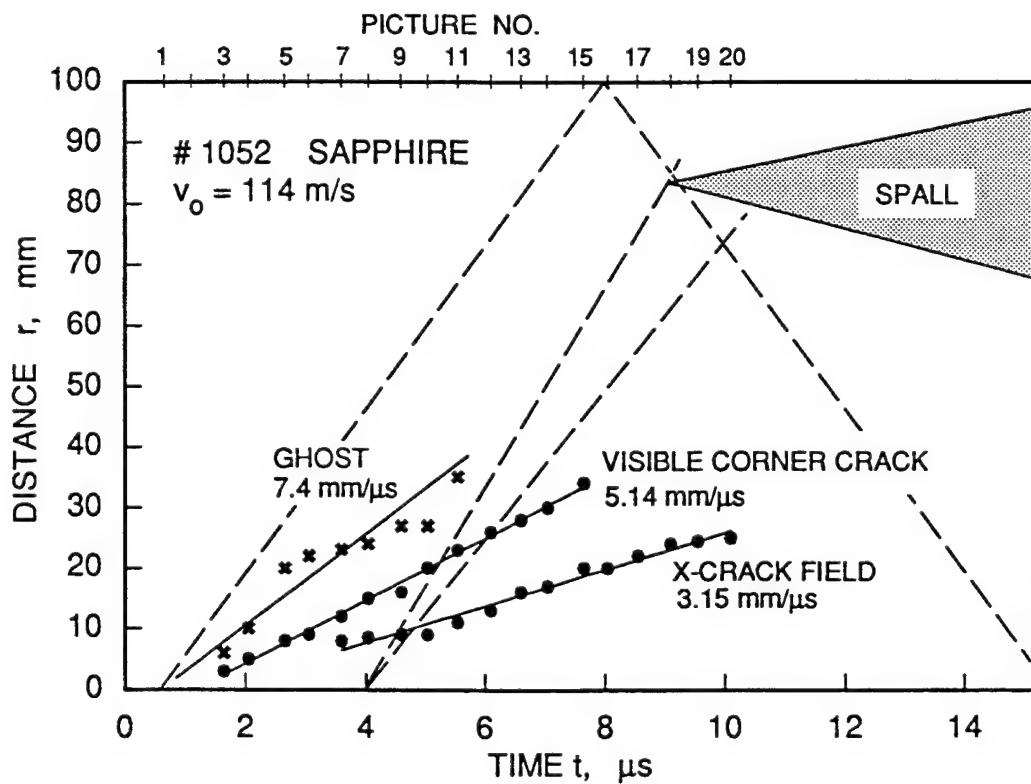
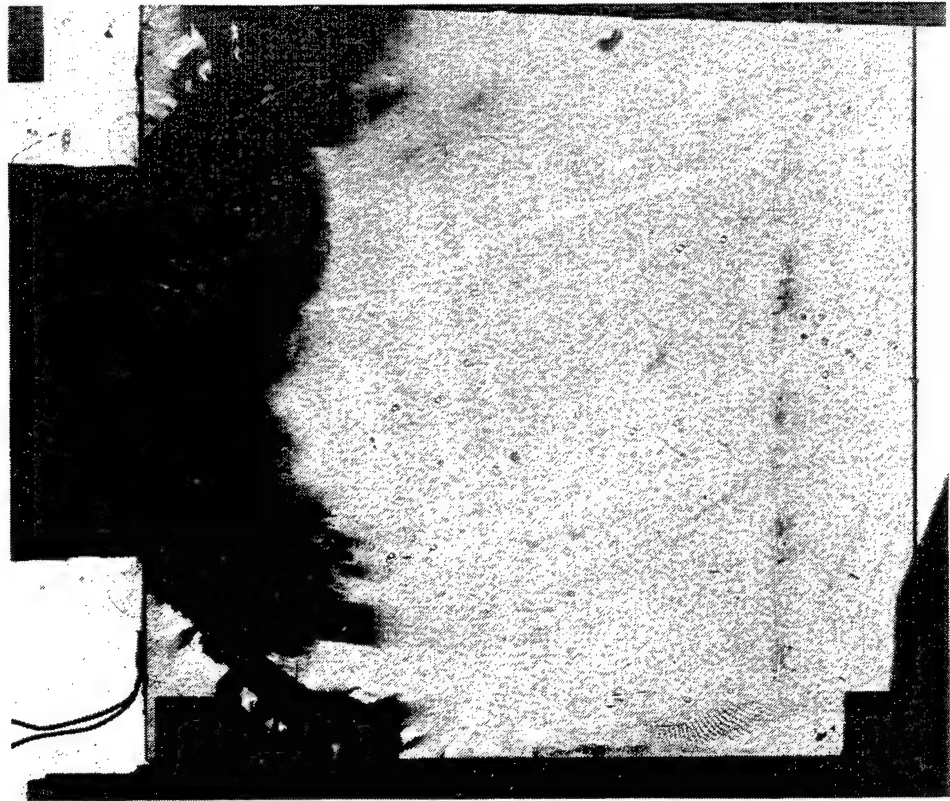


Fig. 4.26 Space-time diagram of fractures, # 1052



(a) picture # 19, 9.55 μ s



(b) picture # 20, 10.10 μ s

Fig. 4.27 Spallation at the rear edge, # 1052

Besides the appearance of spallation 17 mm from the back edge (see Fig.4.27), the 45° lower edge crack (and with some delay, caused by the misalignment, also the upper edge crack) is most interesting in this experiment because of a precursing ghost, see diagram, Fig.4.26. From crack appearance it is assumed that these two cracks are generated with or with little less than longitudinal wave velocity. The black part of the lower edge crack seems to propagate with about 5 mm/ μ s which is close to Rayleigh wave velocity. Cracks of the central main system (x cracks, i.e., cracks in x direction) propagate with velocities around 3 mm/ μ s or less.

Spalling occurs when the reflected leading edge of the primary pulse - which is a tensile stress - interacts with the arriving trailing edge of the same pulse. This trailing edge has passed the steel impactor slab and did, therefore, split up into an elastic and a slower plastic wave and was also fanned out at the rear impactor edge. This effect can, for instance, be seen in Figure 4.9 with the rear pulse edge being much thicker than the two pulse fronts. This is the reason for the observed time-extended development of the spalling effect, although the reflected wave front is assumed to be a sharp one.

5. WAVE PHENOMENA

5.1 Camera Limits

A main tool used with the presented work is the high speed Cranz-Schardin camera which, of course, has limited properties, e.g., a limited speed, which concerns framing rate, time delay, and exposure time. In applications, however, it is of importance to assess these limits. The time delay (which is connected to the time jitter) is independently determined by recording the light pulses by an oscilloscope. The framing rate is automatically limited mainly by the exposure time. This exposure time could be determined by photographing waves in the target materials.

Basically, properties of this type of camera connected with speed depend on the light pulse, see Figure 5.1. This occurs electronically delayed and exhibits a certain length. The delay time counted from the trigger event consists of two parts, the time to the beginning of the pulse which was measured to be between 0.3 to 0.5 μ s, and the rise time to the maximum of the pulse which is considered to be the instant the picture is taken. This is $\approx 0.35 \mu$ s, Figure 5.1. The maximum observed total delay time was, therefore, 0.85 μ s.

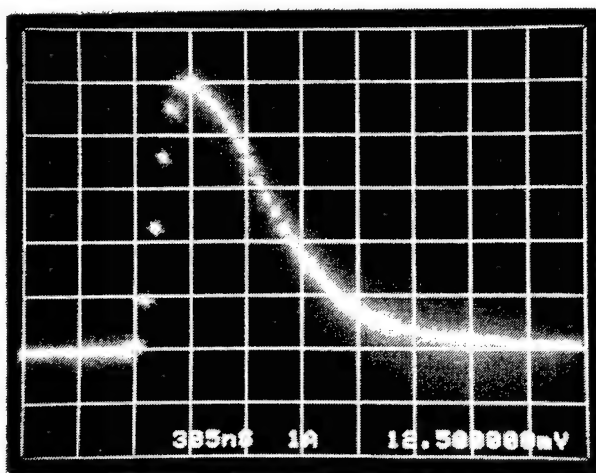


Fig. 5.1 Camera light pulse (spark); SR = 50 ns

The question is then which part around the maximum of the spark pulse illuminates the film. This exposure time can be determined by the width of the shadow of a wave

front in a picture. Due to the lack of plastic effects in ceramics and glass the wave profile can be considered to be steep and narrow. If the spark were a very short light pulse the photo would show this as a sharp line. Real photos, however, show a shadow with a finite width x which suggests an exposure time of $t_e = x/c$, with c being the velocity of the wave. This is with sapphire $c = 11.5 \text{ mm}/\mu\text{s}$ and with glass $c = 5.86 \text{ mm}/\mu\text{s}$.

In sapphire experiments a width $x \approx 5 \text{ mm}$ is observed. This leads to $t_e = 0.43 \mu\text{s}$. The width x in glass experiments is between 2 and 3 mm. Using $x = 2.5 \text{ mm}$ an exposure time of $t_e = 0.43 \mu\text{s}$ is calculated for glass. It is concluded, therefore, that the exposure time is

$$t_e \approx 0.5 \mu\text{s}.$$

This reveals an error source of about a quarter of a microsecond in determining the position of a moving effect, e.g., a wave. For a longitudinal wave in ceramics this is about a delay of 3 millimeters and for glass 1.5 millimeters, if the center of the stripe is taken for its position. The sign of this error is known from the direction of the movement; the read position is that of a retarded move. If the first appearance of a stripe is used for reading, the error will be smaller but remains usually unknown since the width of the stripe may depend on the amount of the effect.

5.2 Wave Velocities and Elastic Constants

The longitudinal sound wave velocity in sapphire was measured in two different ways, by an ultrasonic method through the tile thickness and from high speed photographs, which is parallel and perpendicular to the C-axis. The anisotropy of sapphire does not seem to be very distinct since both results fit well together.

METHOD OR SHOT #	c_L m/s	PROPAGATION DIRECTION TO C-AXIS
U l t r a s o n i c	11 360	p e r p e n d i c u l a r
# 1 0 4 0	11 610	p a r a l l e l
# 1 0 5 0	11 480	p a r a l l e l
# 1 0 5 2	11 700	p a r a l l e l

Table 5.1 Longitudinal wave velocities in sapphire

The average value of all results is

$$\bar{c}_L = (11 538 \pm 149) \text{ m/s} \quad \text{or} \quad \bar{c}_L = 11 538 \text{ m/s} \pm 1.3 \% .$$

Due to the finite length, L, of the projectile (the slab thickness) the pressure wave is of limited duration. In those cases when a bar or slab with 10 mm thickness was used the pulse duration, T, is twice the travel time for a wave through the projectile, $T = 2L/c_{\text{steel}} = 3.5 \mu\text{s}$. This time corresponds to a pulse length of about 40 mm in sapphire. The leading edge of the original pulse is considered to be relatively steep because of minimum plasticity effects. The trailing edge, however, is formed in the steel projectile thus fanned out by plastic effects and reflection.

In some experiments also the Rayleigh wave velocity, c_R , could be determined from the photographs.

SHOT #	c_R m/s	PROPAGATION DIRECTION TO C-AXIS
# 1 0 4 0	5 780	p a r a l l e l
# 1 0 5 0	5 720	p a r a l l e l
# 1 0 5 2	(5 980)	p a r a l l e l

Table 5.2 Rayleigh wave velocities in sapphire

The data point localization, however, was relatively uncertain. The best value was derived from # 1050,

$$c_R = 5720 \text{ m/s} .$$

Shear waves cannot directly be observed by photography. In experiment # 1050, however, an indirect method could be applied to determine shear wave velocity, c_T . It was assumed that the edge nucleation effect coincides with the arrival of the shear front at the edge. Measurement of the movement of the nucleation sites resulted in an average shear velocity

$$\bar{c}_T = (6170 \pm 150) \text{ m/s} \quad \text{or} \quad \bar{c}_T = 6170 \text{ m/s} \pm 2.5 \% .$$

From known wave velocities Poisson's ratio can be derived by the formula

$$\frac{c_T}{c_L} = \sqrt{\frac{1 - 2v}{2(1 - v)}} . \quad (5.1)$$

Using $c_T = 6.17 \text{ mm}/\mu\text{s}$ and $c_L = 11.5 \text{ mm}/\mu\text{s}$ a Poisson's ratio

$$v = 0.2979$$

results. The Poisson's ratio can also be determined from

$$c_L = \sqrt{\frac{E}{\rho} \frac{1-v}{(1+v)(1-2v)}} . \quad (5.2)$$

From this follows with $M = E/(\rho c^2)$

$$M = \frac{(1+v)(1-2v)}{1-v}$$

or

$$v = + \sqrt{\frac{1-M}{2}} + \left[\frac{1-M}{4} \right]^2 - \frac{1-M}{4} .$$

Using the range of moduli E of Table 3.2 and $\rho c^2 = 516 \text{ GPa}$ Poisson's ratios of

$$v = 0.3286 \quad (E = 350 \text{ GPa}) \quad \text{and} \quad v = 0.2937 \quad (E = 390 \text{ GPa})$$

are calculated. The value, $v = 0.29$, supported also by Experiment # 1050 seems reasonable. As a result of this work

$$E = 390 \text{ GPa} \text{ and } v = 0.29$$

can be confirmed.

5.3 Wave Formation in a Slab

The compression generated by the flat impact event travels with longitudinal wave velocity into the slab. Along the wave front only an x-component of the compression exists:

$$\varepsilon_x \neq 0, \quad \varepsilon_y = \varepsilon_z \equiv 0. \quad (5.3)$$

This means on the other hand that a triaxial stress field exists in and behind the wave front. Ceramics exhibit a wide range of elastic behavior. Consequently, Hooke's law can widely be applied:

$$\sigma_{ij} = \frac{E}{1+v} \varepsilon_{ij} + \frac{vE}{(1+v)(1-2v)} \varepsilon_{kk} \delta_{ij}. \quad (5.4)$$

For a wave field not influenced by surfaces this leads to

$$\sigma_x = \frac{E(1-v)}{(1+v)(1-2v)} \varepsilon_x, \quad (5.5)$$

and

$$\sigma_y = \sigma_z = -\frac{v}{1-v} \sigma_x. \quad (5.6)$$

With the condition $v \leq 0.5$ follows $\sigma_z \leq \sigma_x$. Hooke's law can also be expressed in terms of strain (or compression) units. This is, e.g., for the z-component in a triaxial stress field

$$\varepsilon_z = \frac{1}{E} [\sigma_z - v(\sigma_x + \sigma_y)]. \quad (5.7)$$

which is identically zero under the conditions cited above. However, equation (5.7) becomes important for an assessment of the strain situation behind the the wave front. A tensile stress is formed thereafter which leads to the effects described in section 5.4.

5.4 Wave Splitting

In some experiments it has been observed that the primary wave front is succeeded by one or more others in a certain distance, travelling with the same speed. A similar effect has been known earlier. Beinert [5] quantitatively investigated that phenomenon with short-pulse loaded glass plates by a schlierenoptical method in 1975. That effect is a geometrical one. The spacing between two succeeding waves depends on plate thickness. Additionally, Beinert observed and measured quantitatively an energy flow from the primary wave front to the following.

For the plane longitudinal compression wave travelling in x direction in order to meet the condition $\sigma_z = 0$ at the free surfaces, a shear wave is generated at each of the target surfaces with a particle acceleration component normal to the surface based on eq.(5.7). This distortion moves with transversal wave velocity into the target. From the geometry conditions sketched in Figure 5.2 it follows

$$X^2 + d^2 = L^2 \quad \text{and} \quad \sin \alpha = \frac{d}{L} = \frac{c_T}{c_L}$$

which leads to

$$X = d \sqrt{\left(\frac{c_L}{c_T}\right)^2 - 1} . \quad (5.8)$$

In particular the shear wave velocity, c_T , can be calculated by the pre-determined quantities speed, c_L , and distance, X , of the wave fronts. d is the thickness of the slab.

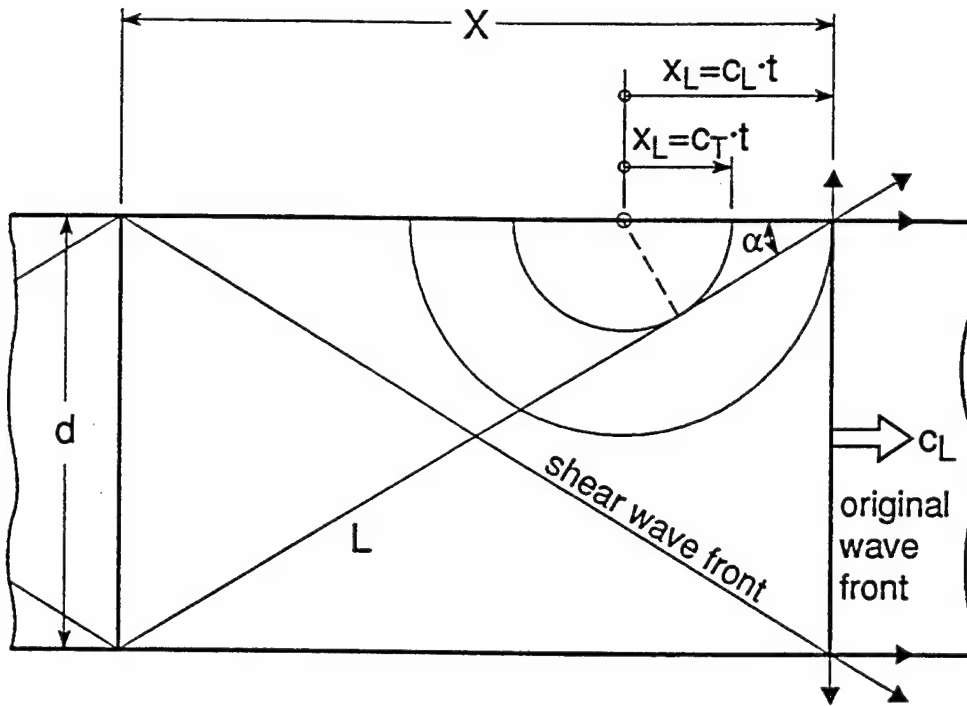


Fig. 5.2 Shear wave formation and wave splitting in a slab (top view)

An attempt is made in Figure 5.3 to geometrically understand what kind of displacement a particle in the slab is subjected to. Due to the condition $\sigma_z = 0$ at the surface the free particle (A, A') not solely moves in the x-direction but it starts also to move perpendicular to the surface (z-direction) resulting into an oblique movement and thus causing the shear wave. The responsible boundary condition at the surface is $\sigma_z = 0$, so that follows from (5.7)

$$\varepsilon_z = - \frac{v}{1-v} \frac{1}{E} \sigma_x$$

with σ_x being little smaller than the original one of the triangle AA'B given by eq.(5.5). The strain perpendicular to the wave propagation direction in the midplane B D is twice that of the regions out of center and can, therefore, lead to a fracture which moves as fast as the longitudinal wave front thus cleaving the slab in two halves. This kind of fracture has been observed in high velocity impact experiments with TiB_2 and SiC as target materials.

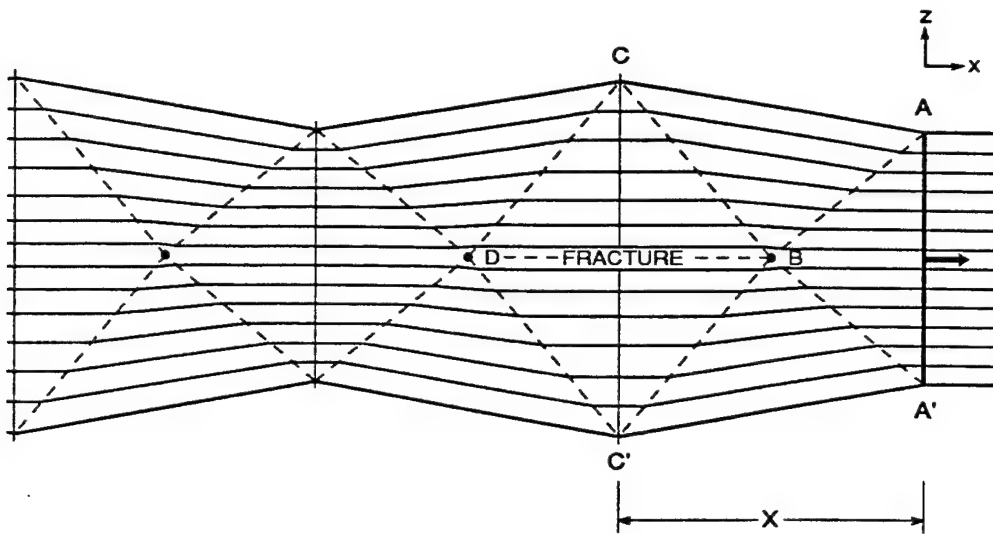


Fig. 5.3 Particle paths in a tile subjected to a wave (top view)

If fracture does not occur, the normal-to-the-surface displacement components are directed inside the slab after plane CC', Fig.5.3, causing an increasing relief normal to the surfaces and thus give rise for a periodic oscillation of the two surfaces with $2X$ being the oscillation period.

The thereby formed wave fronts are visualized on the pictures by the deviation of light, they appear as a shadow stripe. This missing light, however, can be found again on nearby pictures either on the leading or on the lag side which probably depends on a slight tilt of the target to the optical axis of the camera. In those cases where this effect was found, most of the missing light was in the picture next to the primary one. Only little of the light was also found in the second or third one. For an understanding how this works Figure 5.4 shows the correspondence between sparks and pictures. For a vertical wave, deviated light was consequently found only in the same row.

As an example (see Fig.5.4) light from spark # 8 illuminates lens # 8. Missing light in this picture caused by a deviating wave front can either be found in picture # 14 (and 20) which is the lag position, or in # 2 which is the lead position.

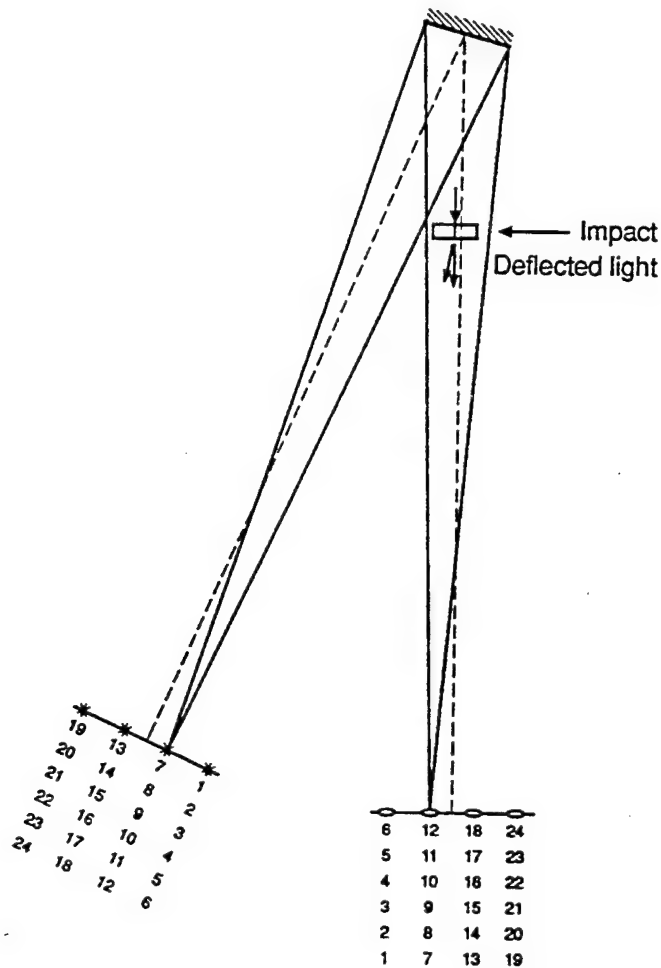


Fig.5.4 Correspondence of sparks and pictures

5.5 Energy Distribution

With the experimental arrangement chosen in the reported experiments the target is usually large compared to the impact site size. Neither the stress distribution, $\sigma(x, y, z)$, in the target nor the distribution of the energy density $w(x,y,z)$ are, therefore, uniform ones. The wave front is a more or less cylindrical one, less with a large impact area. An attempt is made, therefore, to at least estimate the actual energy distribution within the target in order to better understand some of the wave and fracture events.

Beginning with the initial stress calculated from the intersection point of the Rayleigh lines of projectile (P) and Target (T) [1],

$$\sigma_A = \frac{Z_p \cdot Z_T}{Z_p + Z_T} v_0, \quad u_p = \frac{Z_p}{Z_p + Z_T} v_0, \quad (5.9a,b)$$

the initial energy density in the generated wave is

$$w_0 = \sigma \epsilon = \frac{\sigma_A^2}{E} = \frac{Z_T^2 \cdot Z_p^2}{(Z_T + Z_p)^2} \cdot \frac{v_0^2}{E} . \quad (5.10)$$

The distribution of the energy density in the wave field is given by

$$w(r) = \frac{dW}{dV} .$$

The volume, $V(r)$, occupied by the wave increases with wave velocity, $c_L = \frac{r}{t}$, with r being the absolute value of the propagation vector of the wave. In those experiments with the impact area, A_0 , being large and constant in time, the energy flux into the target (the power) is, up to that instant when reflected waves arrive at the interface, also a constant:

$$N = \frac{dW}{dt} = \text{const.}$$

The initial energy W_i is given by $w_0 V_i$, with $V_i = A_0 \cdot r$ being an initial volume:

$$V_i = A_0 \cdot c \cdot t,$$

so that follows

$$N = w_0 \cdot A_0 \cdot c$$

and

$$w(r) = \frac{w_0 A_0}{dV/dr} . \quad (5.11)$$

The volume of the wave field for a flat impact and a target geometry of 10 cm x 10 cm x 1 cm is

$$V(r) = D \cdot d \cdot r + d \cdot r^2 \pi / 2,$$

with r being the wave propagation distance, d the target thickness and D the projectile diameter. $A_0 = D \cdot d$ is the contact area. From this follows

$$w(r) = \frac{w_0 A_0}{A_0 + d \cdot r \cdot \pi}. \quad (5.12)$$

This is a $(1/r)$ -hyperbolic curvature. At the beginning, $r = 0$, the energy density starts with $w = w_0$; for large distances r , the energy density w approaches zero. This result shows also that in those cases when a propagation vector is parallel to the lateral surfaces of the volume $V(r)$, dV/dr can simply be replaced by the wavefront surface $S(r)$.

With a point or a line contact, i.e., a hemispherical or a knife edge shaped impactor, for instance, the determination of the energy density distribution, $w(r)$, appears more difficult. In this case the impact area A_0 grows with time from zero to a certain value which can be either elastic or plastic. In correspondence with A_0 the energy flux increases from zero to a final value which depends on material and impact conditions. Another complication may arise if the shape of the impacted body is not a simple one.

In cases with simple geometry when the inferred energy is represented by a uniform compression a recalculation of the stress distribution by

$$\sigma_r(r) = \sqrt{E \cdot w(r)}, \quad (5.13)$$

with E being Young's modulus, may be possible. This curve exhibits a $1/\sqrt{r}$ slope.

Equations (5.11) to (5.13) do not hold anymore if energy is consumed to produce a comminuted zone or to fracture the target. This energy is lost for the subsequent wave energy distribution within the target. As is pointed out with more detail in section 6.3 there is some reason for the assumption that just half of the initial energy - the kinetic part - remains in the wave which would affect the effective initial energy

density w_0 and reduce the two sets of curves, $w(r)$ and $\sigma(r)$ by a factor of 1/2 or $\sqrt{1/2}$, respectively.

An application of this formalism has been made with shots # 1040, # 1050, and # 1052 without considering the effect of energy reduction by damage effects. The energy distribution is given by eq.(5.12) using $d = 10$ mm, $A_0 = 49$ mm \times 10 mm, and w_0 from eq.(5.10). These curves are shown in Figure 5.5 and calculated up to $r = 40$ mm, the approximate pulse length. With these calculations it was not considered that, possibly, energy was lost by the Mescall zone production. In Figure 5.6 $\sigma_r(r)$ curves of these three experiments are also shown calculated with eq.(5.13). Both Figures are an attempt to demonstrate qualitatively how energy and stress develop when the pulse penetrates the target.

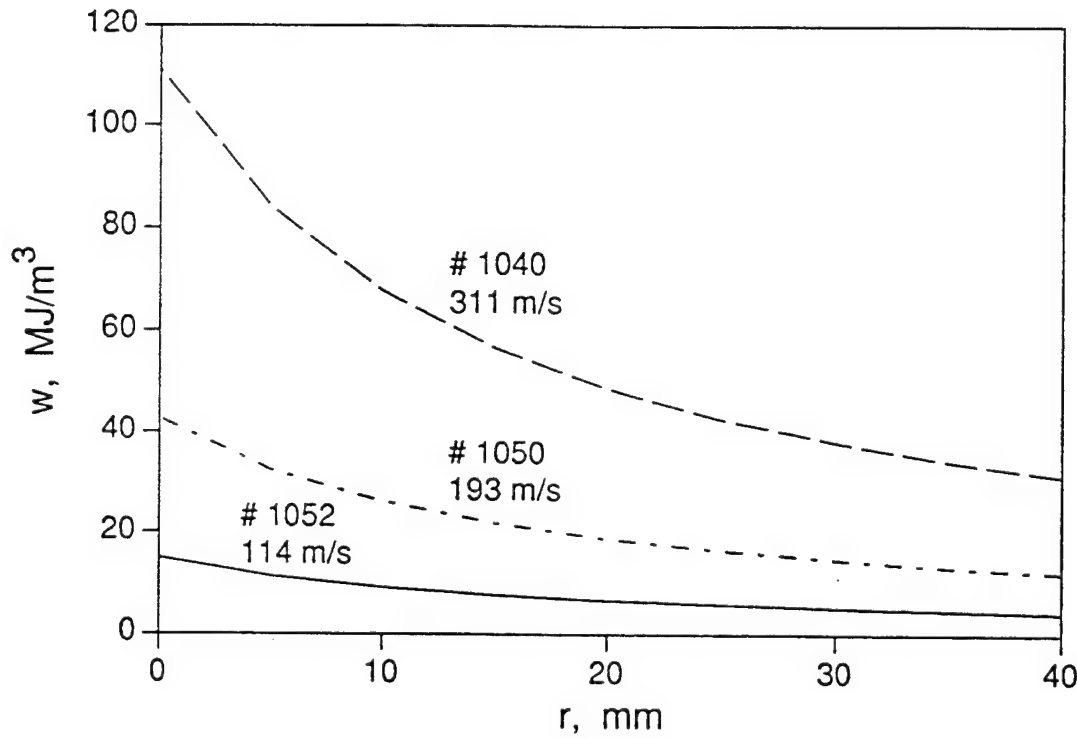


Fig. 5.5 Distribution of energy density in the wave

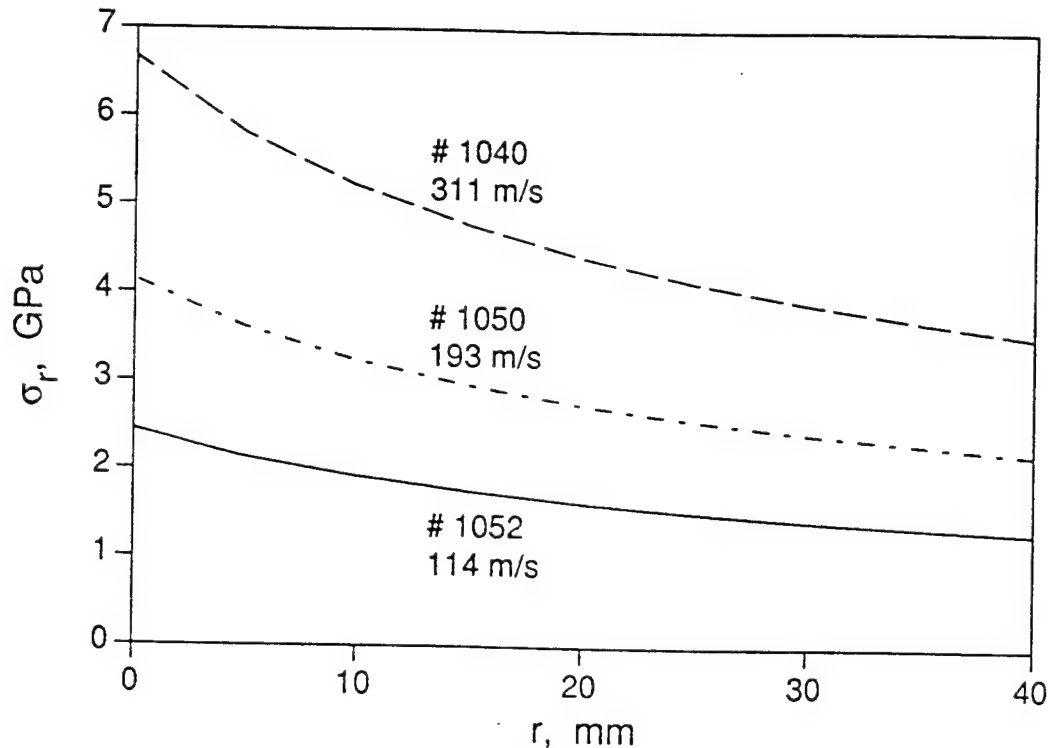


Fig. 5.6 Distribution of radial stress in the wave

5.6 Temperature of the wave field

From a known initial energy density, w_0 , of a wave field the adiabatic temperature rise, ΔT_0 , at the impact site can roughly be determined by

$$\Delta T = w_0 / \rho C \quad \text{or} \quad \Delta T = \frac{\rho \cdot c^2 \cdot v_0^2}{4 \cdot E \cdot C} \quad (5.14)$$

with C being the heat capacity of the material. For sapphire two values of C are given in Table 3.2 : $C_1 = 419 \text{ J/(kg}\cdot\text{K)}$ and $C_2 = 754 \text{ J/(kg}\cdot\text{K)}$. The temperature rise is, therefore, either ΔT_1 or ΔT_2 , whatever a heat capacity has been used for computation. Calculated data for this initial temperature rise are given in Figure 5.1 as a function of the impact velocity, v_0 . Initial wave temperature at $v_0 = 100 \text{ m/s}$ is either 8°C or 4°C over room temperature depending on which C has been used. With an impact velocity of $v_0 = 311 \text{ m/s}$ (# 1040) the corresponding temperature rises are about 70 K or 35 K, respectively.

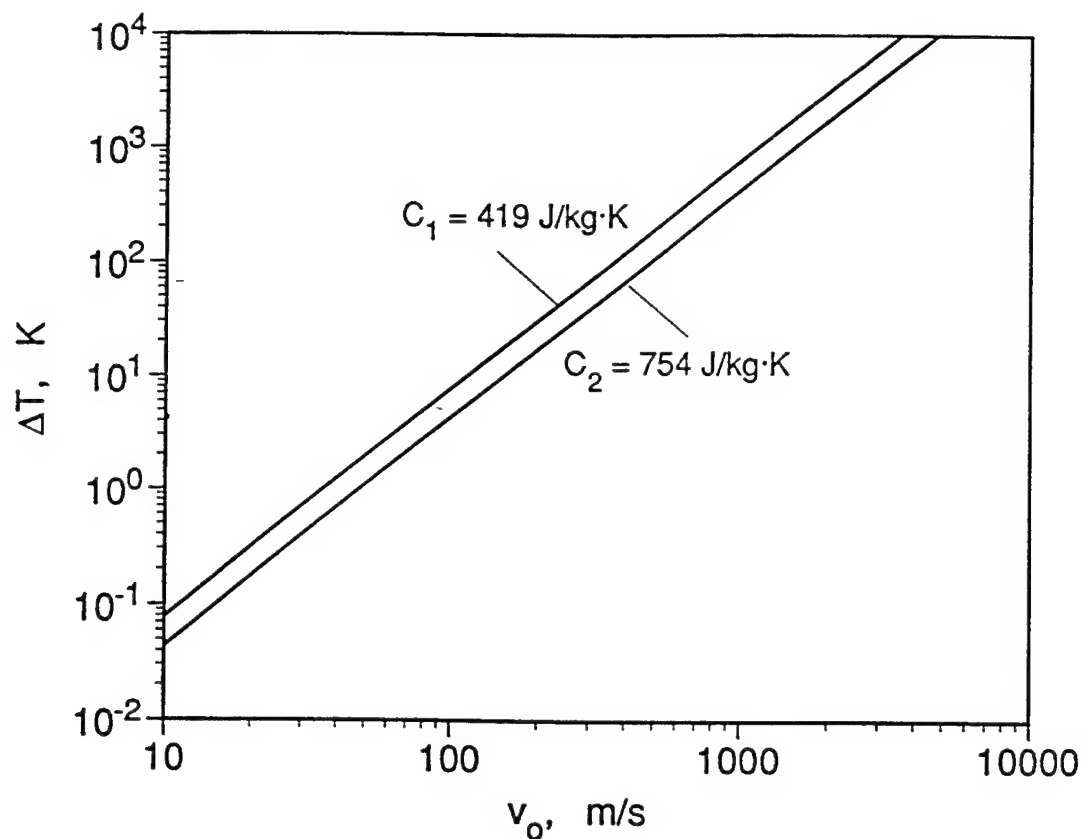


Fig. 5.7 Initial adiabatic wave temperature rise vs. impact velocity in sapphire

The temperature rise distribution of the entire wave field could be calculated, if the energy density distribution, $w(r)$, given, for instance, by eq.(5.12), in the wave field were known, or, vice versa, if the temperature at one point in the wave field could be measured, e.g., by a thermocouple, the energy distribution, $w(r)$, in the wave field could be determined in turn using one of the eqs.(5.11, 5.12).

6. FRACTURE PHENOMENA

6.1 General

Fracture mechanics states that under uniaxial loading conditions the crack speed can vary only up to a certain limit. This *terminal crack velocity* was theoretically determined by, e.g., Yoffé [6], Broberg [7], Freund [8] to be Rayleigh wave velocity: $v_{c,\max} = c_R$. Experiments showed that usually the terminal crack velocity is even less. For float glass with a longitudinal wave velocity of $c_L = 5860$ m/s the terminal crack velocity is 1460 m/s which is about half the Rayleigh wave velocity.

This "law" seemed to be violated with recent experiments on alumina tiles [2, 3]. Depending on impact conditions crack velocities up to about 90 % of the longitudinal wave velocity have been reported. Crack paths with such large propagation speeds appear fuzzy. It is not finally clear whether the observed phenomena are propagating cracks or just a chain of coalescing independent nucleations and what is the influence of the particular geometry of the target.

These very high crack velocities, on the other hand, did not occur with glass as a test material in impact experiments. In no case a crack was observed exceeding the terminal velocity of 1460 m/s. But with glass also never a crack propagation speed less than terminal velocity was observed [1].

For alumina it was concluded that the geometry will certainly have an influence but the material will primarily cause this strange behavior. It was, therefore, highly interesting what would be found with sapphire which is a material of the same chemical composition, Al_2O_3 , when impacted under the same geometrical conditions.

6.2 Summary of Fracture Phenomena

Quasistatic tests have been performed by Cook and Pharr [9]. They used an inverted microscope to photograph crack patterns in sapphire and several other transparent ceramics and glasses produced by a Vickers diamond indenter. Viewing in the direction opposite to the indentation direction (the 0001 direction), these workers found that ring and cone cracking did not occur, but rather that radial cracks and twins initiated almost immediately upon load application and that their trajectories were extremely

dependent on crystallographic orientation. Many of the radial cracks grew out of planes perpendicular to the indented surface. The primary radials nucleated sequentially during loading and were often followed by smaller secondary radials. On unloading the radials cracks continued to grow and lateral cracks formed. Similar observations were made by Evans and Wilshaw [10] and Lenkford and Davidson [11]. Cone cracks, observed in many glasses, were not seen by Cook and Pharr in any of the seven monocrystalline ceramics which they investigated, although they are nearly always produced in polycrystalline ceramics under high-rate loading (Shockley et al, [12] for example).

In the low blow tests (# 1035, sapphire, # 1038, glass) crack systems have been photographed which seem to consist of two types. *Radial cracks* propagate into the energy expanding direction about perpendicular to the two large surfaces. *Shell cracks* develop more or less parallel to the surface, normal to the radial cracks. These are curved to the surface like shells and, therefore, slow down and come to a halt when they reach the surface, see Fig.4.5, for instance.

In slab or bar impacts fractures are immediately generated at the projectile corners, therefore called *corner cracks*. These do not seem to be Hertzian *cone cracks*. Projectile corners are, obviously, most critical for an immediate destruction initiation of the target. Shearing processes seem to be responsible. Even after a high velocity impact these corner cracks occur first and propagate at an angle of approximately 45° to the x-direction (the impact direction). What is reproduced on the photos does not seem to be all of the cracks. Advancing vestiges suggest that the real crack speed is much higher than the one measured on the photos. The visible black part of these corner cracks propagates usually at around $5 \text{ mm}/\mu\text{s}$, the real speed is estimated to be 7 to $8 \text{ mm}/\mu\text{s}$. The reason for these vestiges seems to be a tunnel effect of the light due to a not sufficiently opened crack as described in section 4.2, shot # 1035.

A corner of the target, shot # 1052, 114 m/s, has been recovered and the structure of the fracture surface is shown in Figure 6.1. The crack propagation direction is upward in this picture. Fracture occurs in several crystal planes with rough steps in between.

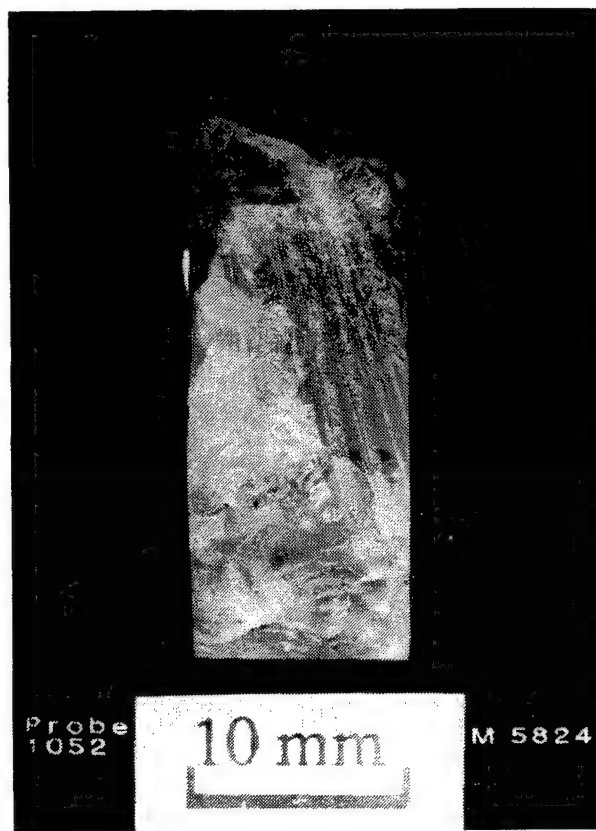


Fig. 6.1 Corner crack, # 1052, 114 m/s

The number of radial cracks increases when the impact velocity is raised, and in the competition between crystal structure and stress field their radial character becomes more clear. The fronts of the radial cracks show a loop-shaped curvature which may be formed by residual surface stresses as is known in float glass.

The propagating shear wave obviously gives rise to crack initiations along the target edges as can be recalculated (sect.4.2, shot # 1050). The cracks develop under about 45° from the edge and the speed ranges between $0.5 c_R$ and c_R .

Inside nucleations were seen with the 114 m/s, 193 m/s and 311 m/s shots. With the fastest shot a damage velocity v_D of almost 90 % of the longitudinal wave speed was achieved with about 2 μs delay at the beginning. This delay and also the damage velocity was less with the 193 m/s experiment: about 1 μs and 65 % of c_L . An augmented energy supply may require time for generating a larger Mescall zone and, thus, change the slope of the wave and cause a certain initial delay for an activation of nuclei.

A crack initiation site was found on a fragment of the # 1035 target (39 m/s). This is shown in the microphotographs of Figure 6.2,a-d: the crack surface sometimes follows different cleavage planes and arrests after a relatively slow propagation period or coalesces with other cracks in a few millimeters distance. The only occasionally visible cleavage steps demonstrate that in a complicated stress-strain situation crystallographic orientations do not play a dominant role.

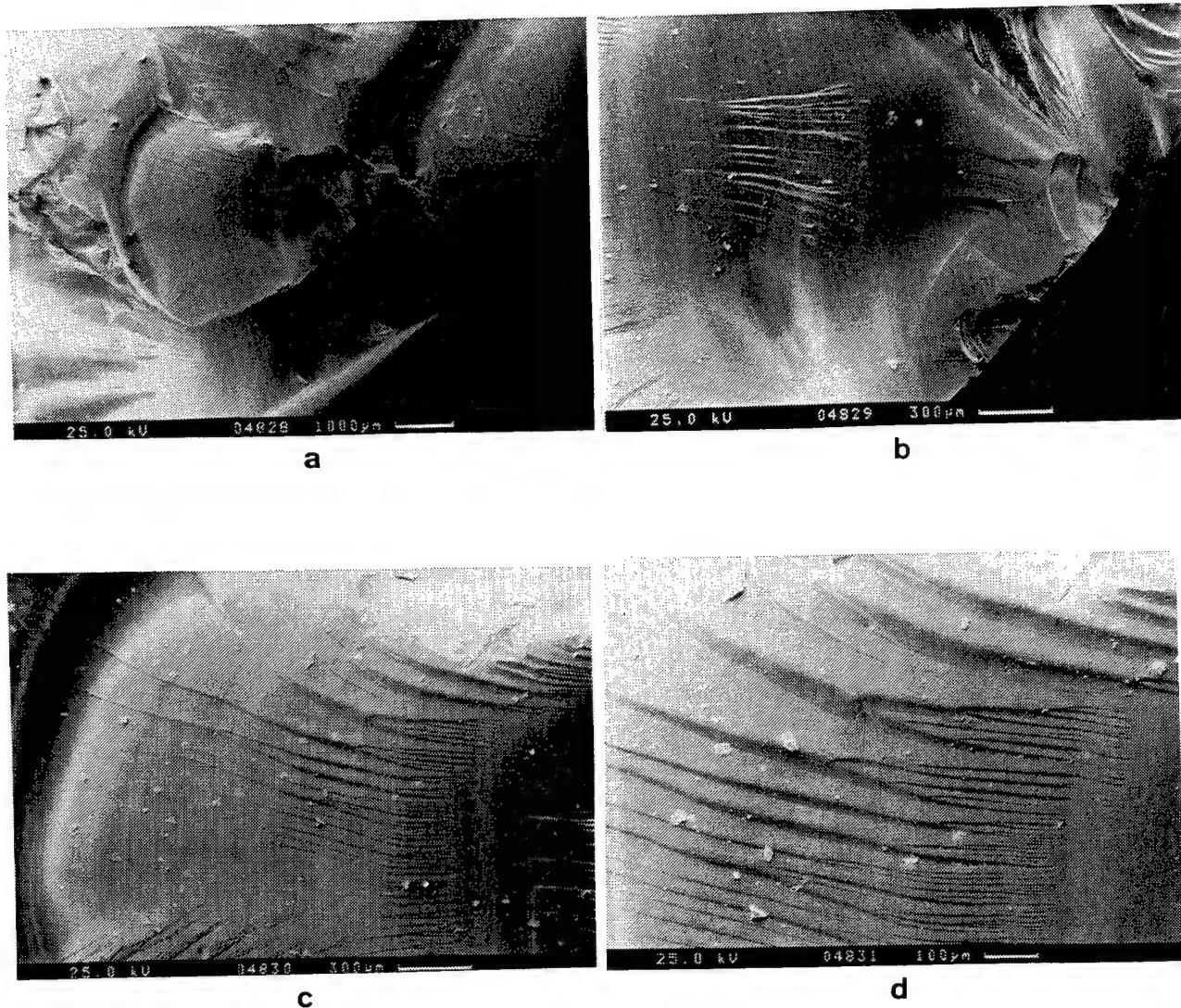


Fig. 6.2 Fracture on a sapphire fragment, # 1035, 39 m/s

Spall-like fracture appears in three of the sapphire experiments, but best in # 1052 at 114 m/s, see Fig.4.27. This straight line of shadow spots occurs 9 μ s after impact at 17 mm (half the pulse length) apart from the rear target edge. This is exactly time and place for the leading edge of the reflected pulse coinciding with the trailing edge of the incoming pulse, there summing up to a tensile stress. From Figure 5.6 it may be estimated that the effective stress at this place could be around 1 GPa with shot # 1052 and, obviously, this level exceeds the threshold for fracture initiation.

6.3 Mescall Zone Development

The high speed pictures show bubble-like air blast waves expanding backwards after impact into the air from the projectile corners, see Figs.4.9 or 4.27, for instance. Their velocity depends on the direction: sonic or less backwards along the projectile edges and supersonic (1 to 1.5 mm/s) along the target edge within the first 5 μ s or longer depending on the impact velocity. Afterwards this speed slows down. Some dark spots in the bubbles suggest larger particles being ejected from the corner when the impact velocity was slow. Radial black lines indicate ejected fine material moving at about 1 mm/ μ s under an angle of about 30° from the target edge. Ejected material is more dense and moves faster (1.5 mm/ μ s) when the impact velocity increases. The ejection angle increases to some 60° with increasing impact velocity. The fine particles overtake the bubble at times exceeding 5 μ s.

A black and cloudy zone in the target in front of the projectile looks at its front like a fan of a large number of single cracks emanating radially from the impact site. Their speed is around 3 mm/ μ s. There is no particular evidence of a comminution zone, even not with the 311 m/s shot. Casual bright spots in the black zone originate from deflected light of a different spark in the same row according Fig.5.4.

It was not possible to measure the particle size during or after the experiment. But an attempt was made to estimate the particle size of the comminuted material on the basis of energy consumption. In a disintegrated initial volume, V , of $n = V/V_p$ particles of an assumed spherical shape with radius, r , and Volume $V_p = 4\pi r^3/3$ the total generated surface is

$$S = n \cdot 4\pi r^2 = 3 \frac{V}{r}$$

The energy transferred by the expanding wave and therefore available within this initial volume is

$$W = w_0 \cdot V,$$

with w_0 from eq.(5.10). This energy, W , is consumed to generate the total surfaces, S , according

$$W = G \cdot S,$$

with $G = K_c^2/E$ being the energy release rate. These equations combined lead to

$$r = 3 \frac{G}{w_0} .$$

For sapphire is known $K_{lc} = 1.80 \text{ MPa}\sqrt{\text{m}}$ (Field [13], Table 1, p.32). With $E = 390 \text{ GPa}$ it follows $G = 8.3 \text{ J/m}^2$ in sapphire. From eq.(5.10) an initial energy density $w_0 = 0.12 \cdot 10^9 \text{ J/m}^3$ is calculated for the fastest shot, # 1040 (311 m/s). With these parameters follows

$$r = 0.2 \mu\text{m}.$$

Figures 6.5 and 6.6 show particles of the Mescall zone of shot # 1040. These are of sub-micrometer size.

The size of the particles depends on the material and on the impact velocity. It does not depend on the impact area. If w_0 is replaced by eq.(5.10) the particle size can be related to the impact velocity. This diagram is drawn in Figure 6.3.

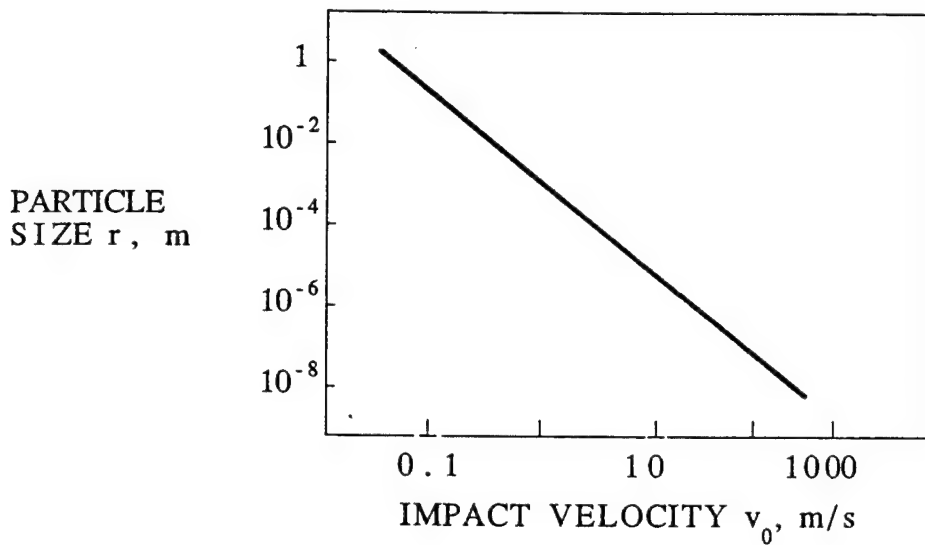


Fig. 6.3 Particle size vs. impact velocity in sapphire

This estimation is certainly too simple. Several influences may reduce the energy available for comminution purposes. The kinetic part of the energy of the wave field which is half of the total may remain for wave propagation instead of being consumed for Mescall zone production. And also the potential fraction may only be used partly for the generation of new fracture surfaces. Other parts will be converted into kinetic energy of the particles or lost by friction, i.e., converted into heat. The actual minimum particle size may, therefore, be larger than the calculated 0.2 μm .

A much more sophisticated micromechanical computational model - named FRAGBED - has been developed by Curran et al [3]. This model takes also into account that effects such as shearing, sliding, flow, ejection, and re-compaction play an important role in the local comminution process. They claim that the material has to be attacked with sufficient energy in order to produce a comminution region with very fine debris which then is called Mescall zone. Sufficient energy, obviously, means several 100 m/s impact velocity depending on both the shock impedances of projectile and target. Ceramographic investigations from shots with confined material which were carried out by Shockley et al [12] revealed the Mescall zone to be a relatively thin layer in front of the projectile nose.

For a comparison of the fracture mechanics properties of sapphire with those of some other ceramic materials Table 6.1 shows fracture toughness data, K_{Ic} , given by Viechnicki et al [14]. Additionally, the range of calculated energy release rates, G, is shown.

Material	YOUNG's Modulus, E GPa	Fract.Toughness K_{Ic} , MPa \sqrt{m}	Energy Rel. Rate G, J/m ²
Sapphire	390 [this report]	1.80 [13]	8.3
SiC	391 ... 408	3.01 ... 5.23	~ 23 ... 68
Al ₂ O ₃	291 ... 394	3.5 ... 3.75	~ 35 ... 41
B ₄ C	457 all [14]	3.7 ... 4.5	~ 30 ... 44
TiB ₂	440 ... 551	6.69 ... 8.00	~ 81 ... 145

Table 6.1 Fracture toughnesses and energy release rates for ceramics

The recovered projectile steel bar of shot # 1040, 311 m/s, contains small fragments and tiny particles of sapphire from the impact site on its surface. The micro-photographs of Figures 6.4 to 6.6 show three different regions with fragments. An overview of almost the entire area is shown in Fig.6.4.a. Larger pieces of the 10 μm range in Figs.6.4.c...e seem small particles re-compacted to larger particles, an effect which may be considered to be a criterion for a Mesall zone. A large sapphire fragment is seen in Fig.6.5. Small particles in the 0.1 to 1 μm range are found on slip planes of the crystal fragment. Tiny sapphire particles on a steel surface are seen in Fig.6.6. These pictures confirm roughly the calculations above.

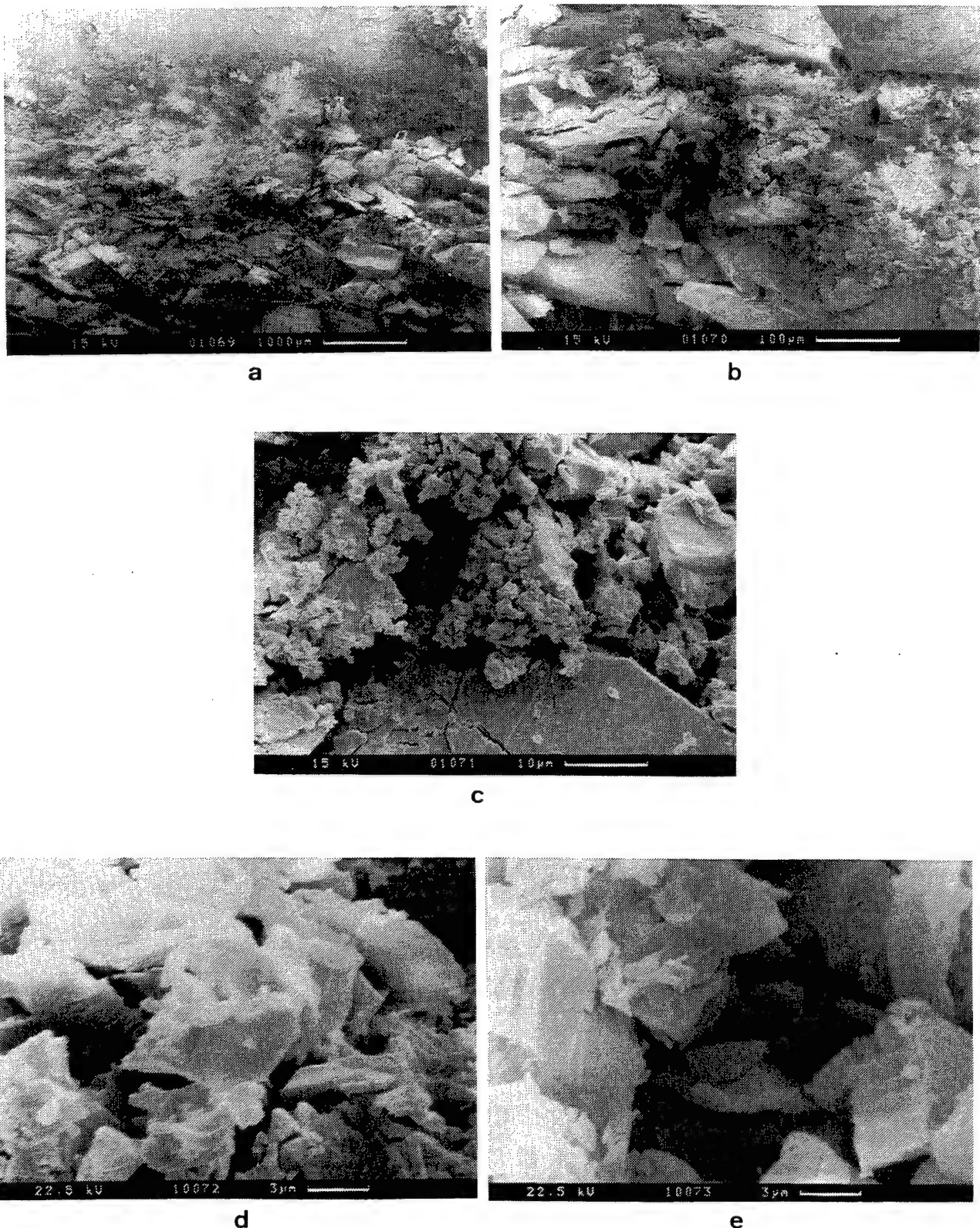
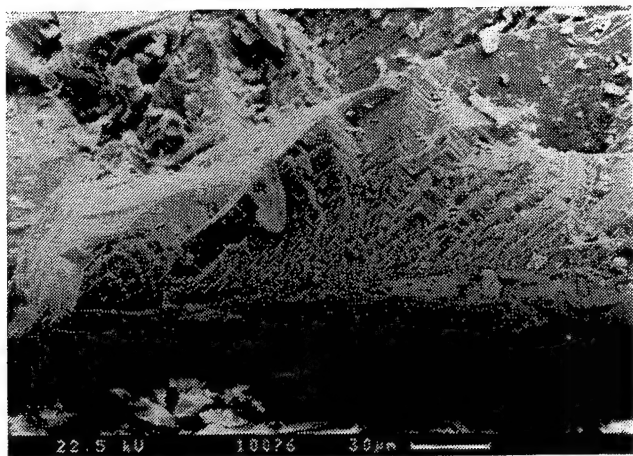
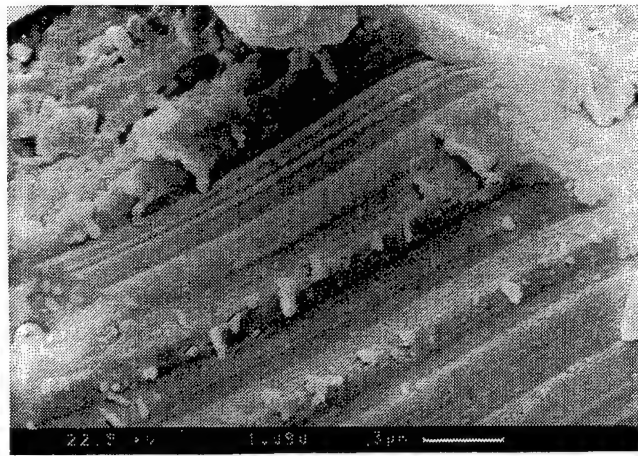


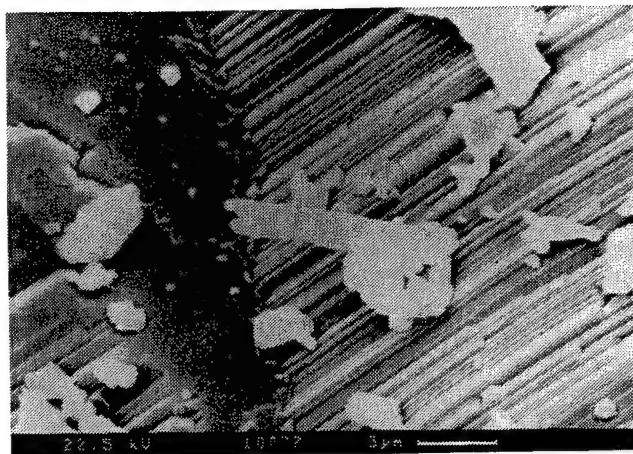
Fig. 6.4 Sapphire particles on steel projectile, # 1040



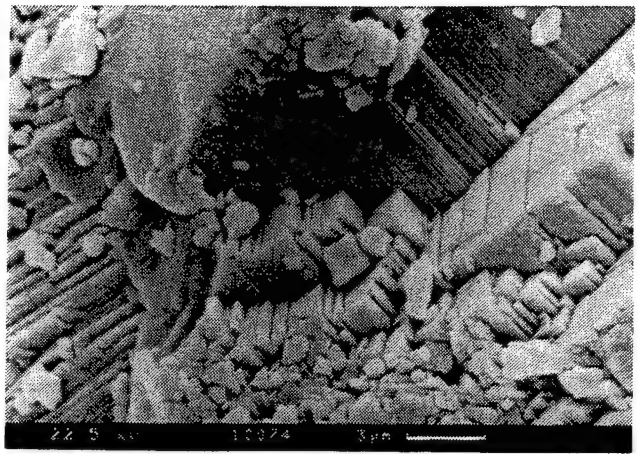
a



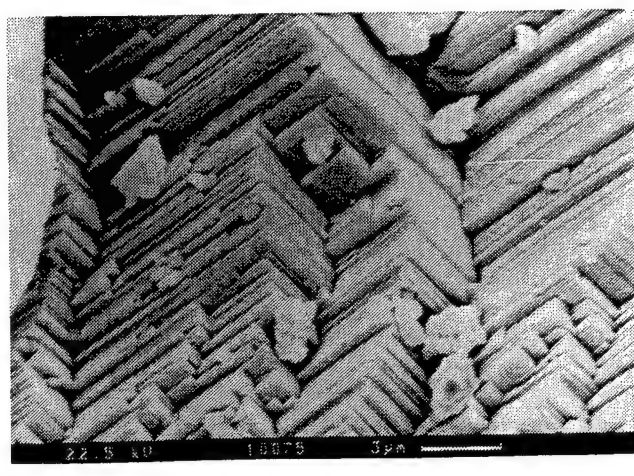
b



c

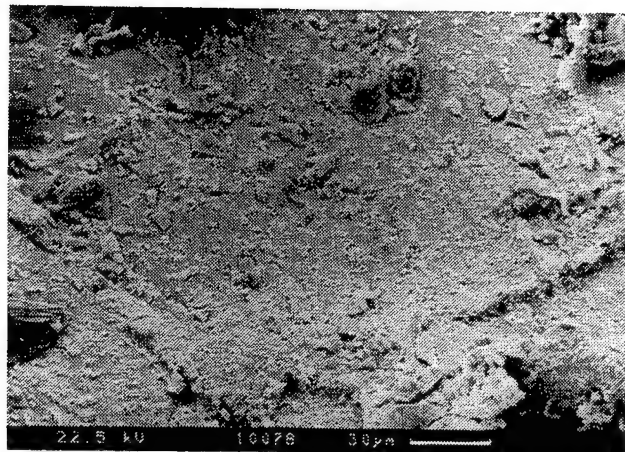


d

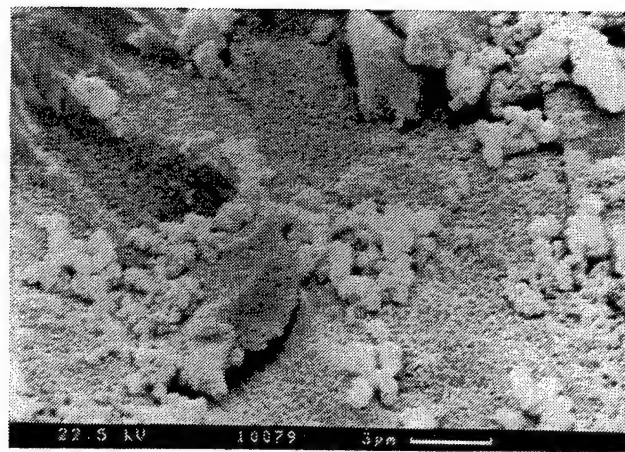


e

Fig. 6.5 Sapphire particles on sapphire, # 1040



a



b

Fig. 6.6 Sapphire particles on steel, # 1040, particle size $\leq 1 \mu\text{m}$

7. ELECTRIC EMISSION METHOD FOR WAVE AND FRACTURE DETECTION

7.1 General

It was assumed and observed in experiments [16] that loaded and fracturing materials of any kind emit electric signals and that this phenomenon could be developed into a measurement technique [16, 17]. This effect was named *electric emission (EE)*. Corresponding to the *magnetic emission (ME)* effect, which was found earlier [18] and which uses a coil as a sensor, for EE a capacitor serves as a pick-up indicating the occurrence or changes of a static electric field, Figure 7.1. Field detection does not require any contact to the specimen, it does not even require a specimen preparation. This method is fast, effective, and inexpensive to apply¹.

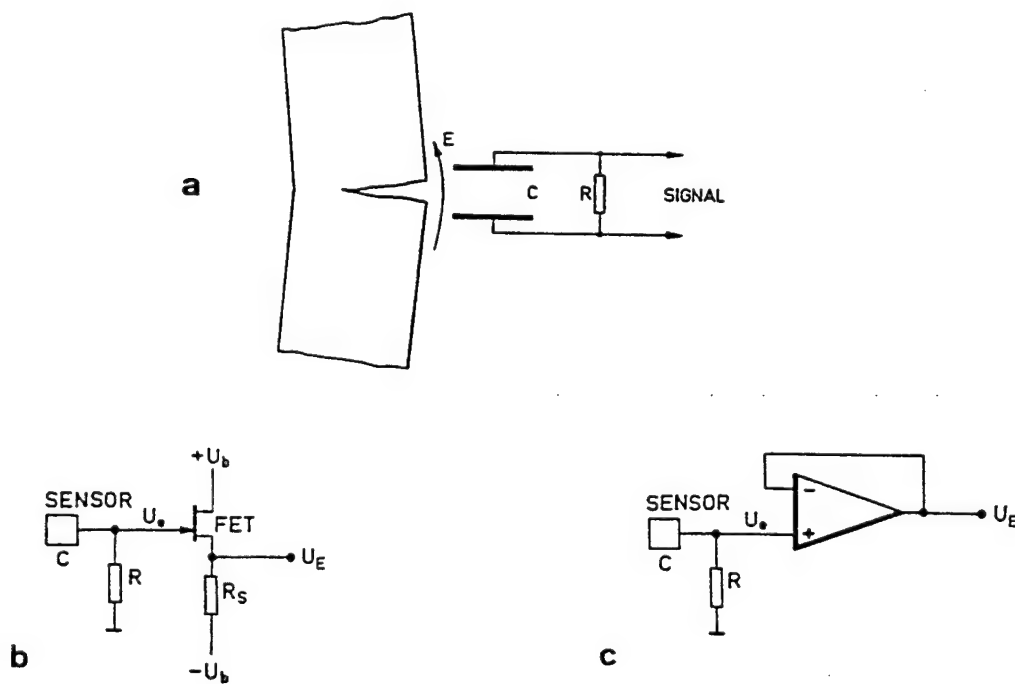


Fig. 7.1 Electric emission method and FET probes

The essential part of the probes used during this work is a field effect transistor (FET, Fig 7.1b). The transistor function is that of a source follower. The advantage is

¹ German Patent Nr. 40 04 171

twofold: this single device furnishes the detection capacitor which is the input capacity of the transistor, and it renders the required impedance conversion. This capacity C - extended by a small metal area of some ten square millimeters only - is of the order of 10 pF (10^{-11} Farad) which, therefore, is capable to deliver large signals, $U = q/C$, with q (= charge) being the signal source. A time constant, $\tau = R \cdot C \approx 10\mu\text{s}$, is chosen for the present application. Instead of a single transistor an operational amplifier with a FET input stage can also be used with the advantage of an accurate zero line (Fig. 7.1c).

With the magnetic emission effect the measured change of the external magnetic field is caused by a change of the magnetic structure of the ferromagnetic material in consequence of an energy transfer into the material. The origin of electric fields measured with the EE method is different from material to material; with high polymeric materials the deformation or rupture of molecule chains may cause large electric fields, with ceramics an elastic deformation (electro striction) of crystals may be the reason for an electric field which is expected to be a rather small effect.

7.2 Pre-experiments For Wave Detection

A series of pre-experiments has been carried out in order to test the capability of the EE method for detecting waves - not fracture - in an impacted material. Tiles of an epoxy resin, Araldite B, of float glass, titanium diboride, TiB_2 , silicon carbide, SiC , alumina, Al_2O_3 , and sapphire, Al_2O_3 , have been used as test materials.

Reported first is a typical result with Araldite B. This material exhibits low wave velocities and did, therefore, not cause any time resolution problems. Material parameters are

$$c_L = 2500 \text{ m/s}, \quad c_T = 1060 \text{ m/s}, \quad c_R = 997 \text{ m/s}, \quad v = 0.39.$$

The tile was impacted edge-on by a 4.5 mm diameter lead bullet at 76 m/s. Two EE probes ($\tau = 10 \mu\text{s}$) were mounted in a distance of 7 mm and 22 mm from the impacted edge. Signals of these two probes are shown in Figure 7.2. The upper signal, (1), comes from the first probe at 7 mm, the lower from the one at 22 mm. The zero line which is almost $400 \mu\text{s}$ corresponds to the free flight distance after the triggering light barrier. This is the same with Figures 7.3 and 7.4.

The second signal, (2), is delayed by 6.0 μ s (difference of the first deviation from zero line of the two signals). This corresponds to an information velocity of 2.5 mm/ μ s which, obviously, is longitudinal wave speed in this material. The individual shape and the difference of the two signals reflects the complicated superposition of waves in the tile. This can be analyzed up to a certain degree. The first minimum of (the upper) signal 1 indicates the arrival of the Rayleigh wave produced at the impact site, this signal is a mixture of the pressure front and the Rayleigh wave.

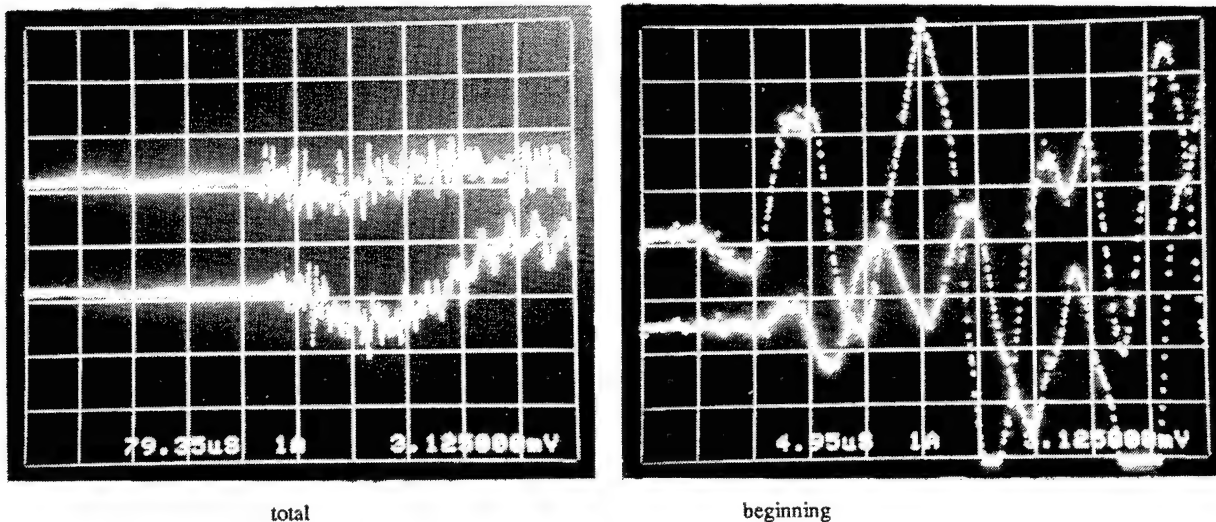


Fig. 7.2 Signals from two EE probes with an impact loaded Araldite B sample

The periodic behavior is due to the wave splitting effect (see sect. 5.4). This can be seen best with signal 2. The calculation of the distance X of two subsequent wavefronts (eq.(5.8)) yields $X = 21.4$ mm or a corresponding time $t = 8.5$ μ s. The distance of the first three or four maxima of signal 2 is little more, 10 μ s. In this material this is probably due to a plastic wave front effect which results in a certain delay.

The same experiments carried out with glass, TiB_2 , SiC, alumina and sapphire are more difficult to analyze because of the very fast wave speed. A typical result with sapphire is shown in Figure 7.3.

Longitudinal wave fronts seem always difficult to detect. Larger effects originate from shear or from Rayleigh waves. This is in particular true with ceramics. The signals are much smaller than with plastic materials as was expected. The second minimum in Figure 7.3 appears delayed by about 1.3 μ s with respect to the first minimum which corresponds to the propagation time of a longitudinal wave between the two probes being positioned on the tile in a distance of 15 mm.

The electric conductivity of TiB_2 was utilized to generate a contact signal for the impact event in Figure 7.4. A 50 μm enamelled copper wire was fixed at the impact site in order to produce a signal when being short-circuited to the grounded target by the projectile. The probe was placed 22 mm from the impact site. The voltage jump in the

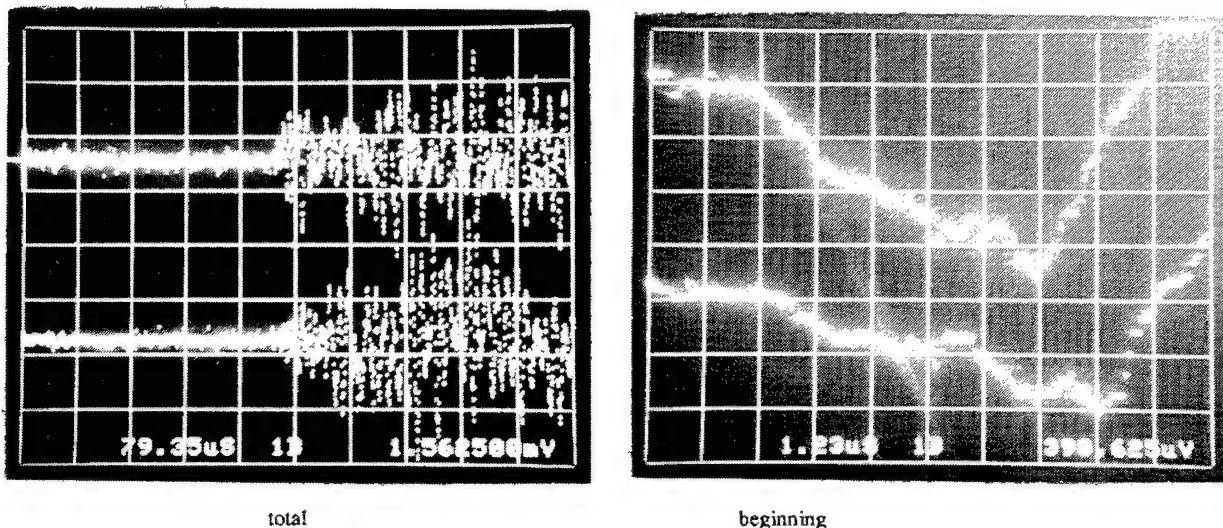


Fig. 7.3 Electric emission signals from two probes with sapphire

upper signal indicates this event. A first hump maximum appears at about 2 μs which can be interpreted as the longitudinal wave front. Even if the wave front would be a pressure steep step function (which is not expected with that point-like contact of a small bullet), the corresponding electric field may not be very sharply located because of the wide-spread source. A second, rather noisy signal begins at 3.4 μs with a maximum

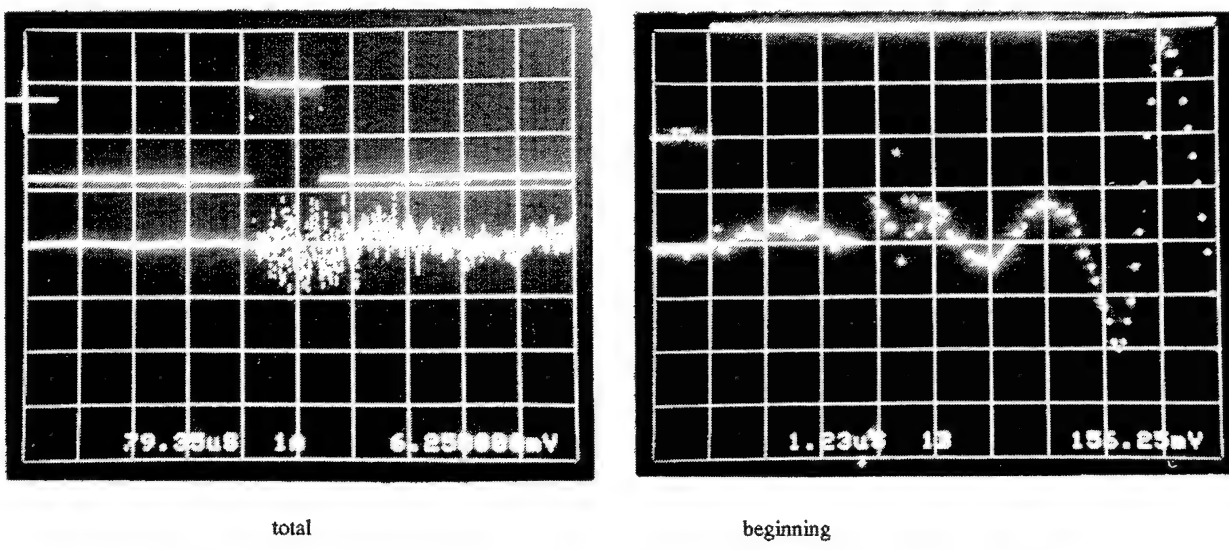


Fig. 7.4 Contact signal and electric emission signal with TiB_2

at about $4.5 \mu\text{s}$ which could correspond to the Rayleigh wave rather than to the shear wave. The periodic signal thereafter shows a repetition rate of $2.5 \mu\text{s}$. If wave splitting accounts for that, this is little more than is calculated using a repeated occurrence $t(2X) = 2.2 \mu\text{s}$ (eq.(5.8) and Fig. 5.3) of the same state in the target.

These experiments - in particular those with Araldite B - demonstrate the capability of the method to detect longitudinal and Rayleigh waves as well, even if interpretation sometimes appears difficult. Currently, it is worked on a further improvement of the probes (shielding, size of sensitive area, time constant).

7.3 Applications in Experiments

In all experiments on glass and sapphire reported in chapter 4 two EE probes have been mounted close to the lower edge of the specimen which can be seen as round or square shadows on the pictures, see high speed photographs of the experiments, chapter 4. This position was chosen in order not to disturb too much the light paths of the high speed camera. The purpose of the probes was to detect the instants of arriving waves or the initiation of fracturing.

Figure 7.5a shows the situation with shots # 1034 and # 1035. A first result was achieved with shot # 1034, Fig.7.5b, on a glass target. Trigger occurred with the cross mark. These signals of the two probes fit approximately to what is calculated for the propagation time of a Rayleigh wave travelling along the edges of the target. For probe 1 the distance is approximately 75 mm and if $c_R \sim 3 \text{ mm}/\mu\text{s}$ is taken for the Rayleigh wave velocity a travelling time of $25 \mu\text{s}$ is calculated which is about what the upper trace shows for the hump. For probe 2 the distance is approximately 125 mm which leads to a travelling time of $42 \mu\text{s}$. Correspondingly, shows the lower trace about $40 \mu\text{s}$ for the hump.

Fig.7.5c shows the signals of shot 1035 with a sapphire target. Contact of the projectile with the target was expected at about $10 \mu\text{s}$ after trigger (crossmark). Electric emission indicates this by the onset of some noise in both of the traces. If time is counted from this mark a first negative hump is found at little more than $10 \mu\text{s}$ in the

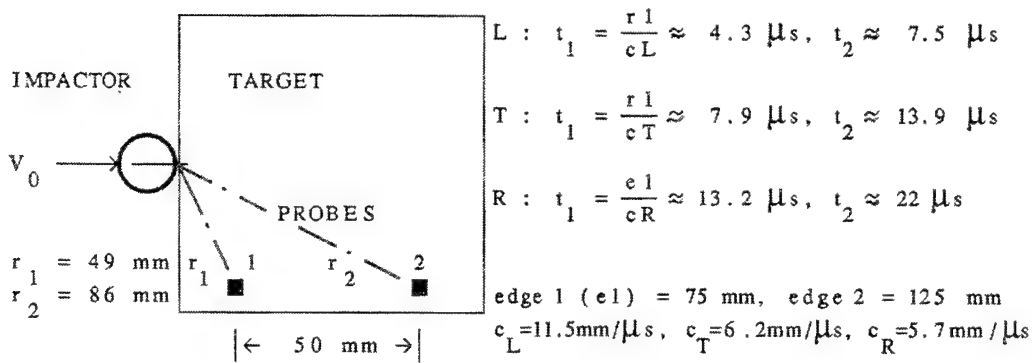


Fig. 7.5a Probe arrangement and propagation times (sapphire only)

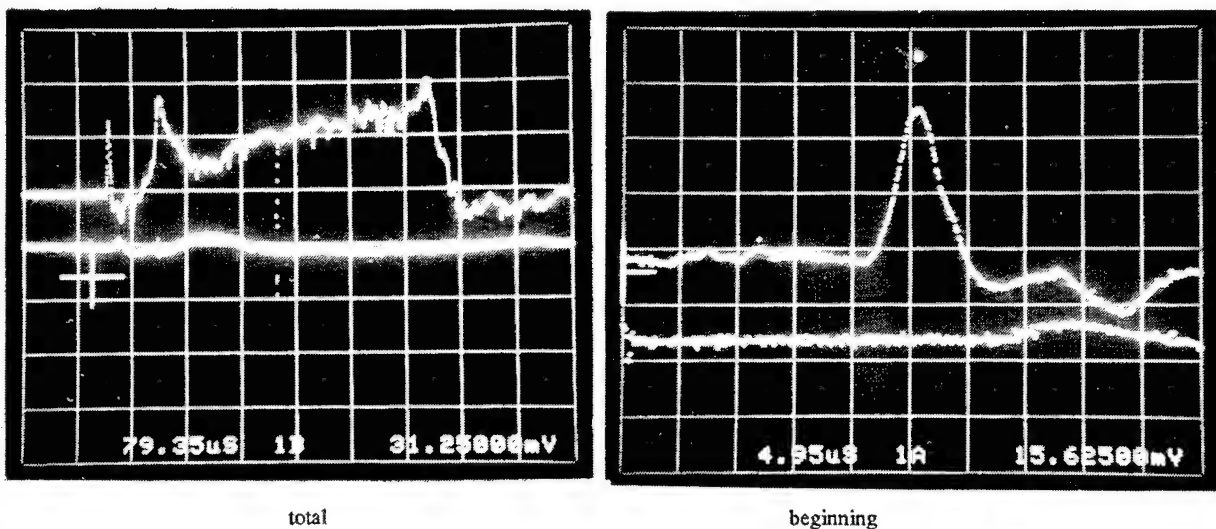


Fig. 7.5b EE signals 1 and 2, shot # 1034, glass, $v_0 = 98 \text{ m/s}$

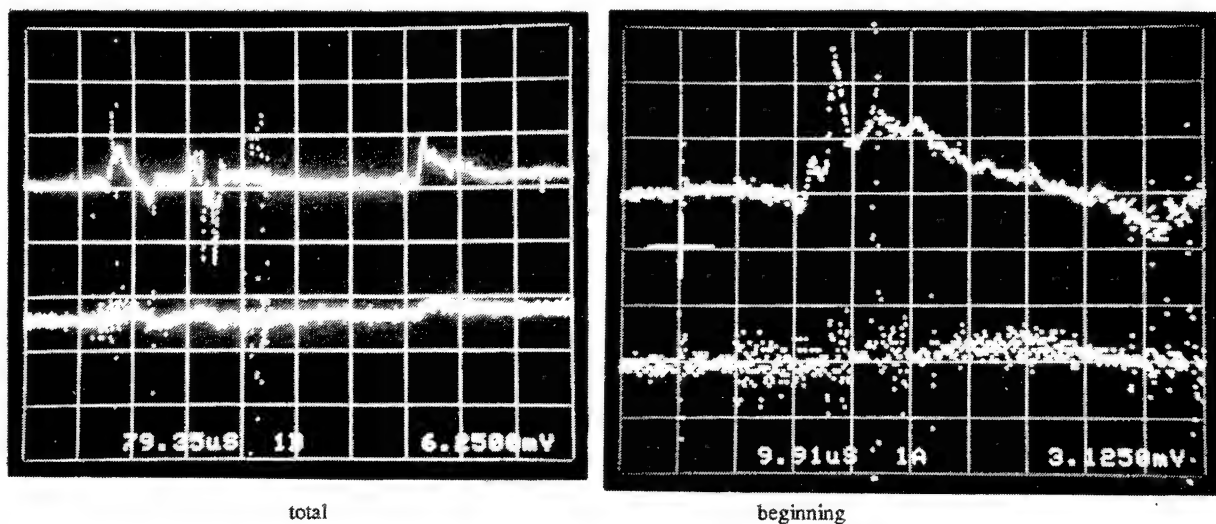


Fig. 7.5c EE signals 1 and 2, shot # 1035, sapphire, $v_0 = 39 \text{ m/s}$

upper trace for probe 1. Due to the low impact velocity in this experiment the lower signal originating from probe 2 is not clear to distinguish within the noise. There is some indication that after $20\mu\text{s}$ a signal begins. The calculations given under R in Fig.7.5a make reasonable that a Rayleigh wave which travelled along the target edges may have caused these parts of the signals. The maxima of the two signals correspond to velocities around $2 \text{ mm}/\mu\text{s}$ which could be caused by the far field of an approaching crack tip (see Fig. 4.2).

The probe arrangement with the two sapphire shots # 1052, $v_0 = 114 \text{ m/s}$, and # 1050, $v_0 = 193 \text{ m/s}$, was the one shown in Figure 7.6a. The signals of the two experiments are shown in Figure 7.6b and 7.6c. In each of the two pictures the upper signal, probe 1, shows the arrival of the primary wave after about 2 or 3 μs indicated by the maximum of a little hump in each curve. A similar effect with probe 2 which is expected at $8 \mu\text{s}$ cannot be stated. There is a noisy event beginning at about this time in both signals of # 1052 which is not understood. A maximum with probe 2 around 15 to 20 μs may be correlated with a more or less complicated arrival of a shear or Rayleigh wave. Within those first 50 μs no fracture can be identified, - even though it seems from the photographs that the targets are totally destroyed in a shorter time. Large signals appear usually at later times as is demonstrated with Figure 7.7, the complete signals of probes (1) and (2) of # 1050. It is also usual that the signal of probe (2) exhibits much larger amplitudes than the other. With shot # 1040, $v_0 = 311 \text{ m/s}$ meaningful signals were not achieved.

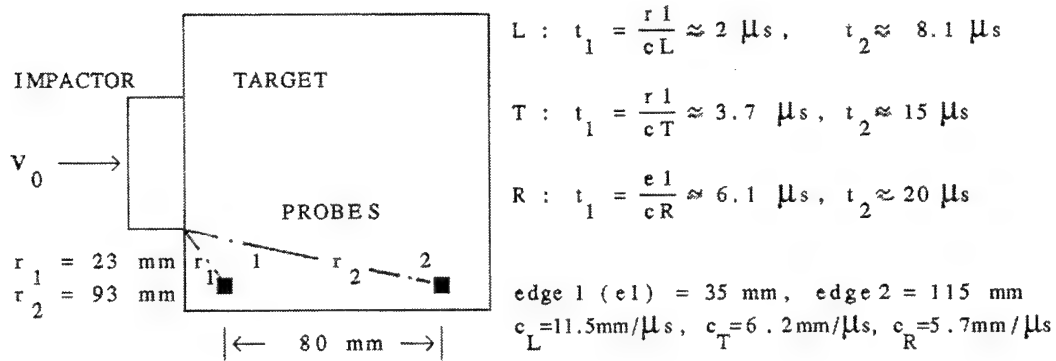


Fig. 7.6a Probe arrangement and propagation times

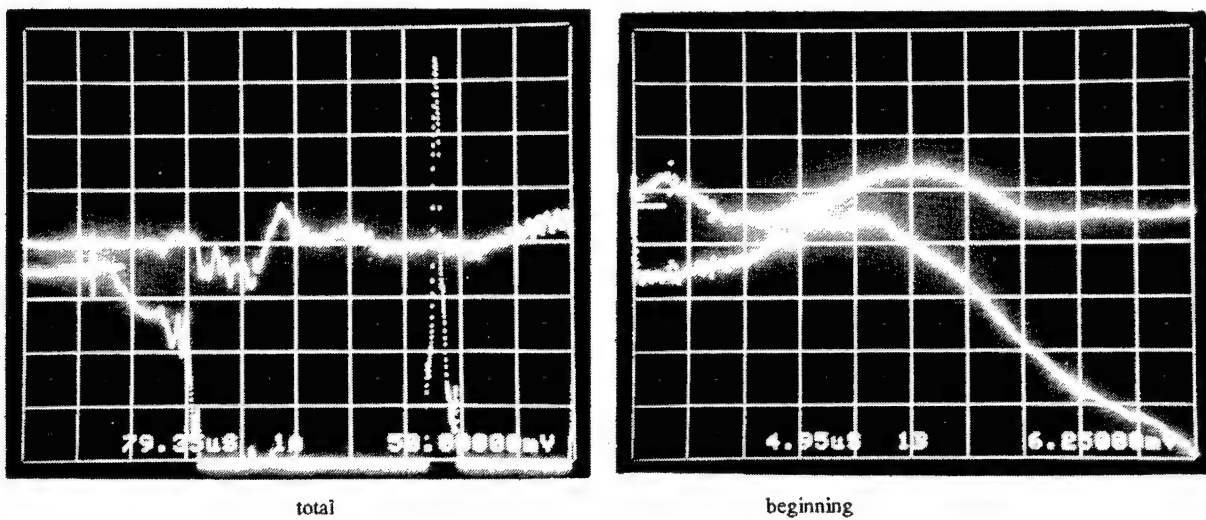


Fig. 7.6b EE signals 1 and 2, shot # 1050, sapphire, $v_0 = 193$ m/s

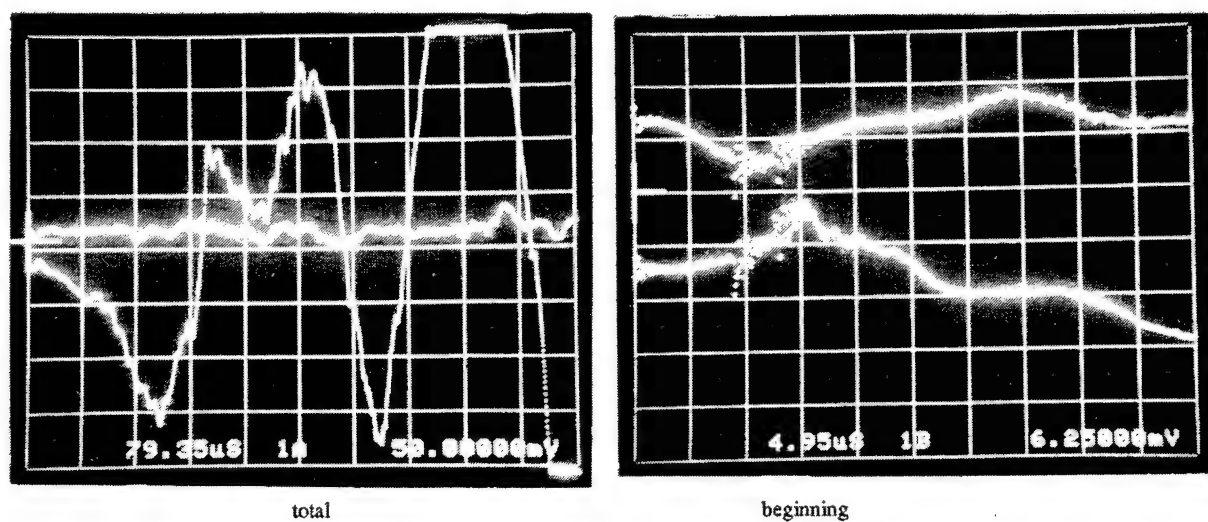


Fig. 7.6c EE signals 1 and 2, shot # 1052, sapphire, $v_0 = 114$ m/s

8. SUMMARY AND CONCLUSIONS

A total of 17 experiments has been carried out within this part of the contract, thereby 6 with sapphire. Planned tasks were the variation of the impact geometry and velocity, and the recovery of the fine debris from the impact site (Mescall zone). Problems arose with triggering the camera when knife-edge impactors were used. Four of five of these experiments failed. We were also not successful with recovering the complete material from the Mescall zone. We were, however, successful in recovering parts of it so that some conclusions could be made.

From high speed photography using a Cranz-Schardin camera wave velocities and the elastic material parameters, Young's modulus and Poisson's ratio, could be determined. Furthermore, the effect of wave splitting was directly observed and measured in glass and in sapphire targets. This supports the assumption that a crack can be drawn in the midplane of the target by the longitudinal wave front, i.e., that a tile may be cleaved in two halves by longitudinal wave speed. It was also seen that the intensity of the shadows which are correlated to the splitted wave fronts vary with propagation time. The first front is most intense in the beginning and decreases thereafter whilst the second grows. This finding that energy moves less fast than the longitudinal wave front was also reported by Beinert [6]. This helps to understand that crack velocities can reach the wave velocity only asymptotically and that the nucleation front must be delayed with respect to the longitudinal wave front. Models were developed on the stress-strain distribution and energy flow within the pressure wave and during the impact event.

In earlier investigations [1] it was found that glass under impact loading fractures with a crack field with a uniform propagation speed, the *terminal crack velocity*. Energy absorption was controlled by (a) the density of the crack field, (b) the density of nucleations of secondary cracks in the pressure wave field in front of the fan of extending primary cracks, and (c) the velocity v_D of the nucleation front [1, 2].

A terminal crack velocity was not found with alumina [2, 3]. Single cracks were produced with low impact velocities and crack fields when the impact velocity was raised. Crack speeds were observed from about 3 000 m/s up to 9 000 m/s. The transferred energy was obviously also augmented when the impact area was increased. With high impact velocities a comminution (Mescall) zone was probably produced. This is concluded from the particles found on the recovered part of the impactor of shot # 1040 ($v_0 = 311$ m/s).

Sapphire ranges in between. The scale of crack velocities extends from several 100 m/s to about 6 000 m/s with two accumulations at about 3 000 m/s and 5 000 m/s which is about the Rayleigh wave velocity and half of it. Similar as with glass and different from alumina activation of nuclei in the pressure wave field was observed with the higher rate impact experiments. The effect of a *damage velocity* was, therefore, also found with sapphire in two experiments: # 1052, $v_D = 7\ 000$ m/s which is 61 % of the longitudinal wave velocity and # 1040, $v_D = 10\ 100$ m/s or 88 % of this fastest velocity.

The crack configuration seems more complicated with sapphire than with amorphous glass or alumina. Although crystallographic or cleavage planes were not found to be preferred crack planes the crystallographic structure of the material seemed to have influenced the fracturing behavior. Parts of a crack surface can sometimes be identified to be crystallographic planes. Radial cracks follow the wave vector which is the direction energy propagates. They seem caused by the tangential tensile stress in the pressure wave field. Shell cracks were observed in low blow tests. Corner cracks initiate the target disintegration at the projectile corners. They develop in consequence of the corner shear stress rather than are Hertzian cone cracks. Observed were also edge cracks which are caused by the incident shear wave. Cracks which develop from nuclei are radial cracks.

Energy consumption in sapphire is, obviously, controlled by number and speed of cracks, viz., by generated surface areas, A, and the rate, \dot{A} , these surfaces are produced, and by the amount and rate of nucleations. The production of a Mescall zone is considered to be part of this although there are also additional contributions of different energy sinks like shearing along slip lines, kinetic energy of the particles, friction (heat generation), and re-compaction. From comminution techniques is known that the compaction effect is particle size dependend. Only particles which achieve a certain minuteness can compact. This effect may, therefore, be considered to be the defining parameter for the Mescall zone. The critical size is probably in the sub-micrometer range - but depending on the material. From shot # 1040 ($v_0 = 311$ m/s) it may be concluded that sapphire particles of 0.1 to 1 μm diameter can compact (Fig.6.4).

9. ACKNOWLEDGEMENTS

The sapphire samples tested in this contract were made available by Dennis Viechnicki, AMTL, Watertown. This is gratefully appreciated. We owe thanks to William A. Gooch from BRL and to the European Research Office of the U.S.Army in London, UK, both for encouragement and funding. Wilbur C. Simmons, the representative of ERO in the starting phase of the contract, has often demonstrated his deep interest in our work. Experiments were carried out with the assistance of Joseph Schüler. Ceramo- and fractographic work was done by Monika Aberham. X-ray examination of the sapphire specimens was performed by Eduard Reisacher.

10. REFERENCES

- [1] U. HORNEMANN, H. ROTHENHÄUSLER, H. SENF, J.F. KALTHOFF, and S. WINKLER, "Experimental Investigation of Wave and Fracture Propagation in Glass Slabs Loaded by Steel Cylinders at High Impact Velocities", Inst. Phys. Conf. Ser. No. 70, pp. 291-298, Paper presented at 3rd Conf. Mech. Prop. High Rates of Strain, Oxford 1984,
- [2] S. WINKLER, H. SENF, and H. ROTHENHÄUSLER, "Wave and Fracture Phenomena in Impacted Ceramics", Final Report, European Research Office of the U.S. Army, London, Contract Number DAJA45-88-C-0011, IWM Report V 23/89, 1989
- [3] S. WINKLER, H. SENF, and H. ROTHENHÄUSLER, "High Velocity Fracture Investigation in Alumina", Proceedings of the Conference on the Fractography of Glasses and Ceramics II, Conference held at Alfred University, July 15-18, 1990, edited by V.D. Frechette, J.R. Varner, pp. 165-183, The American Ceramic Society, 1991
- [4] D.R. CURRAN, L. SEAMAN, TH. COOPER, D.A. SHOCKEY, "Micromechanical Model for Comminution and Granular Flow of Brittle Material under High Pressure and High Strain Rate; Application to Penetration of Ceramic Plates", SRI International, Poulter Laboratory Technical Report 001-91, December 1991
- [5] LINDE brochure on sapphire
- [6] J.M. BEINERT, "Schlierenoptical Stress Analysis of Short Duration Pulses in Elastic Plates", J. Appl. Mech. Vol.42, No.1, pp.5-8, 1975
- [7] E.H. YOFFE, "The Moving Griffith Crack", Phil. Mag. 42, pp.739-750, 1951
- [8] K.B. BROBERG, "The Propagation of a Brittle Crack", Ark. Fiz. 18, pp.159-192, 1960
- [9] L.B. FREUND, "Crack Propagation in an Elastic Solid Subjected to General Loading", I and II, J. Mech. Phys. Solids, 20, pp.129-152, 1972
- [10] R.F. COOK and G.M. PHARR, "Direct Observation and Analysis of Indentation Cracking in Glasses and Ceramics", J. Am. Soc. 73, pp.787-815, 1990
- [11] A.G. EVANS and T.R. WILSHAW, "Quasi-Static Solid Particle Damage in Brittle Solids-I. Observations, Analysis, and Implications", Acta Metall., 24, pp.939-956, 1976
- [12] J. LENKFORD and D.L. DAVIDSON, "The Crack Initiation Threshold in Ceramic Materials Subject to Elastic/Plastic Indentation", J. Mater. Sci., 14, pp.1662-1668, 1979
- [13] D.A. SHOCKEY, A.H. MARCHAND, S.R. SKAGGS, G.E. CORT, M.W. BURKETT, and R. PARKER, "Failure Phenomenology of Confined Ceramic Targets and Impacting Rods", Int. J. Impact Engng. Vol 9, No.3 pp.263-275, 1990

- [14] J.E. FIELD, "Investigation of the Impact Performance of Various Glass and Ceramic Systems", Final Technical Report, ERO Contract DAJA45-85-C-0021, Cavendish Laboratory, Department of Physics, University of Cambridge, August 1988
- [15] D. VIECHNICKI, W. BLUMENTHAL, M. SLAVIN, C. TRACY, and H. SKEELE, "Armor Ceramics - 1987", Proceedings of The Third Tacom Armor Coordinating Conference 17-19 February 1987, Monterey, California, Army Materials Technology Laboratory, Watertown, MA, 1987
- [16] S. WINKLER, "Brucherkennung mit elektrischer Emission", Fraunhofer-Institut für Werkstoffmechanik, Freiburg i.Br., IWM-Bericht T 10/90, 1990
- [17] H. LOVSE, E. STRASSBURGER, H. SENF, G. ZIMMERMANN, B. SALZIGER, "Erfassung der Rißbildung in Werkstoffen durch Ausnutzung der elektrischen Emission", Fraunhofer-Institut für Kurzzeitdynamik, Weil am Rhein, EMI-Bericht 8/91, 1991
- [18] S.R. WINKLER, "Magnetic Emission Detection of Crack Initiation", Fracture Mechanics: Twenty-First Symposium, ASTM STP 1074, J.P. Gudas, J.A. Joyce, and E.M. Hackett, Eds., American Society for Testing and Materials, pp. 178-192, Philadelphia, 1990

<u>NO. OF COPIES</u>	<u>ORGANIZATION</u>
2	DEFENSE TECHNICAL INFO CTR ATTN DTIC DDA 8725 JOHN J KINGMAN RD STE 0944 FT BELVOIR VA 22060-6218
1	HQDA DAMO FDQ ATTN DENNIS SCHMIDT 400 ARMY PENTAGON WASHINGTON DC 20310-0460
1	US MILITARY ACADEMY MATH SCI CTR OF EXCELLENCE DEPT OF MATHEMATICAL SCI ATTN MDN A MAJ DON ENGEN THAYER HALL WEST POINT NY 10996-1786
1	DIRECTOR US ARMY RESEARCH LAB ATTN AMSRL-CS AL TP 2800 POWDER MILL RD ADELPHI MD 20783-1145
1	DIRECTOR US ARMY RESEARCH LAB ATTN AMSRL CS AL TA 2800 POWDER MILL RD ADELPHI MD 20783-1145
3	DIRECTOR US ARMY RESEARCH LAB ATTN AMSRL CI LL 2800 POWDER MILL RD ADELPHI MD 20783-1145

ABERDEEN PROVING GROUND

2 DIR USARL
ATTN AMSRL CI LP (305)

<u>NO. OF COPIES</u>	<u>ORGANIZATION</u>	<u>NO. OF COPIES</u>	<u>ORGANIZATION</u>
1	HQ DEPT OF THE ARMY ATTN SARD TR R CHAIT PENTAGON WASHINGTON DC 20310-0103	3	DIR LLNL ATTN EDWARD J CHAPYAK MS F664 JOSEPH V REPA MS A133 MICHAEL O SCHNICK MS F607 PO BOX 1663 LOS ALAMOS NM 87545
6	CDR US ARMY TACOM ATTN AMSTA TR T FURMANIAK S GOODMAN D HANSEN M MINNICK D THOMAS J THOMPSON WARREN MI 48397-5000	4	DIR LLNL ATTN R GOGOLEWSKI MS L290 R LANDINGHAM L369 J REAUGH L32 D STEINBERG PO BOX 808 LIVERMORE CA 94550
2	CDR US ARMY RESEARCH OFFICE ATTN J BAILEY K IYER PO BOX 12211 RESEARCH TRIANGLE PARK NC 27709-2211	6	DIR SANDIA NATL LABS ATTN J ASAY MS 0458 R BRANNON MS 0820 L CHHABILDAS MS 0821 D CRAWFORD ORG 0821 M FORRESTAL DIV 1551 PO BOX 5800 ALBUQUERQUE NM 87185-0307
1	CDR EUROPEAN RSCH OFC USARDSG (UK) ATTN R REICHENBACH PSC 802 BOX 15 FPO AE 09499-1500	1	CIA ATTN OSWR DSD W WALTMAN ROOM 5P0110 NHB WASHINGTON DC 20505
1	CDR NGIC ATTN W MARLEY 220 SEVENTH AVE CHARLOTTESVILLE VA 22901-5391	1	BROWN UNIV DIV OF ENGINEERING ATTN R CLIFTON PROVIDENCE RI 02912
1	NAVAL RESEARCH LABORATORY ATTN ANDREW E WILLIAMS CODE 6684 4555 OVERLOOK AVE SW WASHINGTON DC 20375	6	INST OF ADVANCED TECH ATTN S BLESS H FAIR T KIEHNE D LITTLEFIELD M NORMANDIA R SUBRAMANIAN PO BOX 202797 AUSTIN TX 78720-2797
1	NAVAL POST GRADUATE SCHOOL ATTN JOSEPH STERNBERG CODE EW MONTEREY CA 93943	3	SOUTHWEST RESEARCH INST ATTN C ANDERSON J RIEGEL J WALKER PO DRAWER 28510 SAN ANTONIO TX 78284
1	AIR FORCE ARMAMENT LAB ATTN AFATL DLJW W COOK EGLIN AFB FL 32542		
2	DIR LANL ATTN F ADDESSIO M BURKETT LOS ALAMOS NM 87545		

<u>NO. OF COPIES</u>	<u>ORGANIZATION</u>	<u>NO. OF COPIES</u>	<u>ORGANIZATION</u>
2	UNIV OF CA SAN DIEGO DEPT OF APPL MECH & ENGR SVCS R011 ATTN S NEMAT NASSER M MEYERS LA JOLLA CA 92093-0411	1	APPLIED RESEARCH ASSOC INC ATTN D GRADY 4300 SAN MATEO BLVD NE STE A 220 ALBUQUERQUE NM 87110
3	UNIV OF DAYTON RSCH INST KLA14 ATTN N BRAR D GROVE A PIEKUTOWSKI 300 COLLEGE PARK DAYTON OH 45469-0182	1	BATTELLE EDGEWOOD ATTN A RICCHIAZZI 2113 EMMORTON PARK RD EDGEWOOD MD 21040
2	ADELMAN ASSOCIATES ATTN C CLINE M WILKENS 3301 EL AMINO RIAL STE 280 ATHERTA CA 94027	1	BRIGS CO ATTN JOSEPH E BACKOFEN 2668 PETERSBOROUGH ST HERNDON VA 22071-2443
1	ADVANCED PROTECTIVE PRODUCTS INC ATTN W PERCIBALLI 910 E MOUNTAIN SKY AVE PHOENIX AZ 85048	1	CALKINS R&D INC ATTN N CALKINS 515 SEWARD PK AVE ALBUQUERQUE NM 87123
2	AERONAUTICAL RSCH ASSOC ATTN R CONTILIANO J WALKER 50 WASHINGTON RD PRINCETON NJ 08540	1	THE CARBORUNDUM CO ATTN R PALIA PO BOX 1054 NIAGARA FALLS NY 19302
2	ALLIANT TECHSYSTEMS INC ATTN T HOLMQUIST G JOHNSON 600 SECOND STREET NE HOPKINS MN 55343	1	CENTURY DYNAMICS INC ATTN N BIRNBAUM 2333 SAN RAMON VALLEY BLVD SAN RAMON CA 94583-1613
1	ALME AND ASSOC ATTN M ALME 6219 BRIGHT PLUME COLUMBIA MD 21044-3790	3	CERCOM INC ATTN A EZIS G NELSON R PALICKA 1960 WATSON WAY VISTA CA 92083
1	APPLIED RESEARCH ASSOC INC ATTN JEROME D YATTEAU 5941 S MIDDLEFIELD RD SUITE 100 LITTLETON CO 80123	1	COORS CERAMIC CO STRUCTURAL DIV ATTN R PARICIO 600 NINTH ST GOLDEN CO 80401
		1	CORNING INC ATTN S HAGG SP DV 22 CORNING NY 14831
		1	CYPRESS INTERNATIONAL ATTN A CAPONECCHI 1201 E ABINGDON DR ALEXANDRIA VA 22314

<u>NO. OF COPIES</u>	<u>ORGANIZATION</u>	<u>NO. OF COPIES</u>	<u>ORGANIZATION</u>
3	DOW CHEMICAL INC ORDNANCE SYSTEMS ATTN C HANEY A HART B RAFANIELLO 800 BUILDING MIDLAND MI 48667	3	LANXIDE ARMOR PRODUCTS ATTN B FRANZEN K LEIGHTON R WOLFFE 1300 MARROWS RD NEWARK DE 19714-6077
1	EPSTEIN AND ASSOC ATTN K EPSTEIN 2716 WEMBERLY DRIVE BELMONT CA 94002	3	O'GARA HESS & EISENHARDT ATTN G ALLEN D MALONE T RUSSEL 9113 LE SAINT DR FAIRFIELD OH 45014
2	GDLS ATTN W BURKE J ERIDON 38500 MOUND RD STERLING HEIGHTS MI 48310-3260	4	POULTER LABORATORY SRI INTERNATIONAL ATTN D CURRAN R KLOOP L SEAMAN D SHOCKEY 333 RAVENSWOOD AVE MENLO PARK CA 94025
1	GENERAL RESEARCH CORP ATTN A CHARTERS PO BOX 6770 SANTA BARBARA CA 93160-6770	1	SAIC ATTN J FURLONG MS 264 1710 GOODRIDGE DR MCLEAN VA 22102
1	GEORGIA INST OF TECHNOLOGY ATTN K LOGAN ATLANTA GA 30332-0245	1	SIMULA INC 10016 SOUTH 51ST STREET PHOENIX AZ 85044
1	INTERNATNL RSCH ASSOC ATTN D ORPHAL 4450 BLACK AVENUE PLEASANTON CA 94566	4	UNITED DEFENSE LP ATTN V HORVATICH M MIDDIONE J MORROW R RAJAGOPAL PO BOX 359 SANTA CLARA CA 95052-0359
1	JET PROPULSION LABORATORY ATTN M ADAMS IMPACT PHYSICS GROUP 4800 OAK GROVE DRIVE PASADENA CA 91109-8099	1	UNITED DEFENSE LP ATTN J JOHNSON PO BOX 15512 YORK PA 17405-1512
1	KAMAN SCIENCES CORP 1500 GARDEN OF THE GODS RD COLORADO SPRINGS CO 80907		
1	KERAMONT CORP ATTN E SAVRUN 4231 S FREEMONT AVE TUSCON AZ 85714		

<u>NO. OF COPIES</u>	<u>ORGANIZATION</u>	<u>NO. OF COPIES</u>	<u>ORGANIZATION</u>
1	ZERNOW TECH SVCS INC ATTN LOUIS ZERNOW 425 W BONITA AVE SUITE 208 SAN DIMAS CA 91773		AMSRL-WM-TD, A M DIETRICH T FARRAND K FRANK A GUPTA M RAFTENBERG G RANDERS-PERSON M SCHEIDLER S SEGLETES J WALTER T WRIGHT AMSRL-WM-WD, A NIILER AMSRL-WM-M, D VIECHNICKI AMSRL-WM-MC
1	R J EICHELBERGER 409 W CATHERINE ST BEL AIR MD 21014-3613		
1	B EINSTEN 1212 MORNINGSIDE WAY VENICE CA 90297		
1	BOB SKAGGS RT 11 BOX 81E SANTA FE NM 87501		M CHEN G GILDE P HAUNG T HYNES J SWAB J WELLS
	<u>ABERDEEN PROV GROUND</u>		AMSRL-WM-MF S CHOU D DANDEKAR J MACKIEWICZ R RAJENDRAN
61	DIR USARL ATTN AMSRL-WM, D ECCLESHALL AMSRL-WM-T, W MORRISON AMSRL-WM-TA, W BRUCHEY G BULMASH M BURKINS G FILBEY W GILLICH W GOOCH (15 CP) T HAVEL E HORWATH Y HUANG H MEYER E J RAPACKI J RUNYEON N RUPERT M ZOLTOSKI AMSRL-WM-TC, W S DE ROSSET F GRACE K KIMSEY M LAMPSON L MAGNESS D SCHEFFLER G SILSBY R SUMMERS W WALTERS		

<u>NO. OF COPIES</u>	<u>ORGANIZATION</u>	<u>NO. OF COPIES</u>	<u>ORGANIZATION</u>
3	AERONAUTICAL & MARITIME RESEARCH LABORATORY ATTN N BURMAN S CIMPOERU D PAUL PO BOX 4331 MELBOURNE VIC 3001 AUSTRALIA	1	CONDAT ATTN J KIERMEIR MAXILLANSTR 28 8069 SCHEYERN FERNHAG GERMANY
1	BATTELLE INGENIEURTECHNIK GMBH ATTN W FUCKE DUESSELDORFFER STR 9 ESCHBORN D 65760 GERMANY	2	DEFENCE TECH & PROCUREMENT AGCY ATTN G LAUBE W ODERMATT BALLISTICS WPNS & COMBAT VEHICLE TEST CTR CH 3602 THUN SWITZERLAND
1	CARLOS III UNIV OF MADRID ATTN C NAVARRO ESCUELA POLITÉCNICA SUPERIOR C/. BUTARQUE 15 28911 LEGANÉS MADRID SPAIN	1	DEFENCE RESEARCH AGENCY ATTN T BARTON FORT HALSTEAD SEVENOAKS KENT TN14 7BP UNITED KINGDOM
1	CELSIUS MATERIALTEKNIK KARLSKOGA AB ATTN L HELLNER S 691 80 KARLSKOGA SWEDEN	6	DEFENCE RESEARCH AGENCY ATTN W CARSON I CROUCH C FREW T HAWKINS B JAMES B SHRUBSALL CHOBHAM LANE CHERTHEY SURREY KT16 0EE UNITED KINGDOM
3	CENTRE D'ETUDES GRAMAT ATTN J CAGNOUX C GALLIC J TRANCHET GRAMAT 46500 FRANCE	1	DEFENCE RSCH ESTAB SUFFIELD ATTN C WEICKERT BOX 4000 MEDICINE HAT ALBERTA T1A 8K6 CANADA
6	CENTRE DE RECHERCHES ET D'ETUDES D'ARCUEIL ATTN D BOUVART C COTENNOT S JONNEAUX H ORSINI S SERROR F TARDIVAL 16 BIS AVENUE PRIEUR DE LA CÔTE D'OR F 94114 ARCUEIL CÉDEX FRANCE	1	DEUTSCHE AEROSPACE AG ATTN M HELD POSTFACH 13 40 D 86 523 SCHROBENHAUSEN GERMANY

<u>NO. OF COPIES</u>	<u>ORGANIZATION</u>	<u>NO. OF COPIES</u>	<u>ORGANIZATION</u>
3	DEUTSCHE FRANZÖSISCHES FORSCHUNGSIINSTITUT SAINT LOUIS ATTN H ERNST K HOOG H LERR CÉDEX 5 RUE DU GÉNÉRAL CASSAGNOU F 68301 SAINT LOUIS FRANCE	3	FRANHOFER INSTITUT FÜR KURZZEITDYNAMIK ERNST MACH INSTITUT ATTN V HOHLER A STILP K THOMA ECKERSTRASSE 4 D 79 104 FREIBURG GERMANY
1	DIEHL GMBH AND CO ATTN M SCHILDKNECHT FISCHBACHSTRASSE 16 D 90552 RÖTBENBACH AD PEGNITZ GERMANY	3	FRANHOFER INSTITUT FÜR KURZZEITDYNAMIK ERNST MACH INSTITUT ATTN H ROTHENHÄUSLER H SENF E STRASSBURGER HAUPTSTRASSE 18 D 79 576 WEIL AM RHEIN GERMANY
1	DYNAMIC RESEARCH AB ATTN Å PERSSON PARADISGRÄND 7 SÖDERTÄLJE S 151 36 SWEDEN	2	HIGH ENERGY DENSITY RESEARCH CTR ATTN V FORTOV G KANEL IZHORSKAYA STR 13/19 MOSCOW 127412 RUSSIAN REPUBLIC
1	ETBS DSTI ATTN P BARNIER ROUTE DE GUERAY BOITE POSTALE 712 18015 BOURGES CEDEX FRANCE	1	INGENIEURBÜRO DEISENROTH ATTN F DEISENROTH AUF DE HARDT 33 35 D 5204 LOHMAR 1 GERMANY
1	EMBASSY OF AUSTRALIA ATTN R WOODWARD COUNSELLOR DEFENCE SCIENCE 1601 MASS AVE NW WASHINGTON DC 20036-2273	1	INST OF CHEMICAL PHYSICS ATTN S RAZORENOV 142432 CHERNOGOLOVKA MOSCOW REGION RUSSIAN REPUBLIC
2	FEDERAL MINISTRY OF DEFENCE DIR OF EQUIPMENT AND TECH LAND RÜV 2 ATTN D HAUG L REPPER POSTFACH 1328 53003 BONN GERMANY	7	INSTITUTE FOR PROBLEMS IN MATERIALS SCIENCE ATTN S FIRSTOV B GALANOV O GRIGORIEV V KARTUZOV V KOVTUN Y MILMAN V TREFILOV 3, KRHYZHANOVSKY STR 252142, KIEV-142, UKRAINE

<u>NO. OF COPIES</u>	<u>ORGANIZATION</u>	<u>NO. OF COPIES</u>	<u>ORGANIZATION</u>
1	INSTI FOR PROBLEMS OF STRESS ATTN G STEPANOV TIMIRYAZEVSKAYA STR 2 252014 KIEV UKRAINE	1	OTO BREDA ATTN M GUALCO VIA VALDIOCCHI 15 I 19136 LA SPEZIA ITALY
3	INST OF MECH ENGINEERING PROBLEMS ATTN V BULATOV D INDEITSEV Y MESCHERYAKOV BOLSHOY, 61, V.O. ST PETERSBURG, 199178 RUSSIAN REPUBLIC	5	RAFAEL BALLISTICS CENTER ATTN M MAYSELESS Y PARTOM G ROSENBERG Z ROSENBERG Y YESHURUN PO BOX 2250 HAIFA 31021 ISRAEL
2	IOFFE PHYSICO TECH INST ATTN E DROBYSHEVSKI A KOZHUSHKO ST PETERSBURG 194021 RUSSIAN REPUBLIC	1	RSCH INST OF MECHANICS NIZHNIY NOVGOROD STATE UNIV ATTN A SADYRIN PR GAYARINA 23 KORP6 NIZHNIY NOVGOROD 603600 RUSSIAN REPUBLIC
1	K&W THUN ATTN W LANZ ALLMENDSSTRASSE 86 CH 3602 THUN SWITZERLAND	1	ROYAL MILITARY ACADEMY ATTN E CELENS RENAISSANCE AVE 30 B 1040 BRUSSELS BELGIUM
1	MORGAN MATROC ATTN C ROBERTSON ST PETERS RD RUGBY WARWICKSHIRE CV 21 3QR UNITED KINGDOM	1	ROYAL NETHERLANDS ARMY ATTN J HOENEVELD V D BURCHLAAN 31 PO BOX 90822 2509 LS THE HAGUE NETHERLANDS
2	NATIONAL DEFENCE RSCH ESTAB ATTN J ERIKSON S SAVAGE FOA 630 S 172 90 STOCKHOLM SWEDEN	3	SNPE ATTN P FABRE C GAUDIN C GOZOUGUEN BP NO 2 91710 VERT-LE-PETIT FRANCE
1	R OGORKIEWICZ 18 TEMPLE SHEEN LONDON SW 14 7RP UNITED KINGDOM	3	SWEDISH DEFENCE RSCH ESTAB ATTN L HOLMBERG B JANZON I MELLGARD BOX 551 S 147 25 TUMBA SWEDEN

NO. OF
COPIES ORGANIZATION

1 TECHNION INST OF TECH
FACULTY OF MECH
ENGINEERING
ATTN S BODNER
TECHNION CITY
HAIFA 32000
ISRAEL

3 TECHNISCHE UNIVERSITÄT
CHEMNITZ-ZWICKAU
ATTN I FABER
L KRUEGER
L MEYER
SCHEFFEL STR 110
09120 CHEMNITZ
GERMANY

2 TNO PRINS MAURITS LAB
ATTN H PASMAN
R YSELSTEIN
PO BOX 45
LANGE KLEIWEG 137
2280 AA RIJSWIJK
NETHERLANDS

1 TOMSK BR OF THE INST
FOR STRUCTURAL
MACROKINETICS
ATTN V GORELSKI
8 LENIN SQ GSP 18
TOMSK 634050
RUSSIAN REPUBLIC

INTENTIONALLY LEFT BLANK.

REPORT DOCUMENTATION PAGE			Form Approved OMB No. 0704-0188
<p>Public reporting burden for this collection of information is estimated to average 1 hour per response, including the time for reviewing instructions, searching existing data sources, gathering and maintaining the data needed, and completing and reviewing the collection of information. Send comments regarding this burden estimate or any other aspect of this collection of information, including suggestions for reducing this burden, to Washington Headquarters Services, Directorate for Information Operations and Reports, 1215 Jefferson Davis Highway, Suite 1204, Arlington, VA 22202-4302, and to the Office of Management and Budget, Paperwork Reduction Project(0704-0188), Washington, DC 20503.</p>			
1. AGENCY USE ONLY (Leave blank)	2. REPORT DATE	3. REPORT TYPE AND DATES COVERED	
	February 1997	Final, Sep 90 - May 93	
4. TITLE AND SUBTITLE Experimental Investigation of Wave and Fracture Phenomena in Impacted Ceramics: Sapphire			5. FUNDING NUMBERS C: DAJA45-90-C-0053
6. AUTHOR(S) H. Senf and S. Winkler			
7. PERFORMING ORGANIZATION NAME(S) AND ADDRESS(ES) Franhofer-Institut fuer Kurzzeitdynamik Ernst-Mach-Institut Weil am Rhein, Germany			8. PERFORMING ORGANIZATION REPORT NUMBER
9. SPONSORING/MONITORING AGENCY NAMES(S) AND ADDRESS(ES) U.S. Army Research Laboratory ATTN: AMSRL-WM-TA Aberdeen Proving Ground, MD 21005-5066			10. SPONSORING/MONITORING AGENCY REPORT NUMBER ARL-CR-310
11. SUPPLEMENTARY NOTES Point of contact for this report is William A. Gooch, Jr., U.S. Army Research Laboratory, ATTN: AMSRL-WM-TA, Aberdeen Proving Ground, MD 21005-5066.			
12a. DISTRIBUTION/AVAILABILITY STATEMENT Approved for public release; distribution is unlimited.		12b. DISTRIBUTION CODE	
13. ABSTRACT (Maximum 200 words) This report documents the experimental investigation of wave and fracture phenomena in monocrystalline sapphire. This research includes comparisons with glass and complements the Ernst-Mach-Institut investigation of ceramics and glasses that was published subsequently in ARL-CR-214, "Experimental Investigations of Wave and Fracture Phenomena in Impacted Ceramics and Glasses." A detailed discussion of wave phenomena and fracture phenomena is included, as well as a discussion of an electric emission method for wave and fracture detection. The work was made possible by the state-of-the-art, high-speed photographic capability available at the Ernst-Mach-Institut, specifically two 24-spark Cranz-Shradin cameras, which can be used both in transmission and reflectance. Sapphire tiles were impacted by both spherical and flat projectiles and the generation of pressure waves and disintegration effects were observed. Twenty-four high-quality photographic images could be obtained at predetermined time intervals of less than 1 microsecond.			
14. SUBJECT TERMS ceramics, sapphire, high-speed photography, impact, spalling, crack nucleation, crack velocity, Mescall zone, electric emission			15. NUMBER OF PAGES 95
			16. PRICE CODE
17. SECURITY CLASSIFICATION OF REPORT UNCLASSIFIED	18. SECURITY CLASSIFICATION OF THIS PAGE UNCLASSIFIED	19. SECURITY CLASSIFICATION OF ABSTRACT UNCLASSIFIED	20. LIMITATION OF ABSTRACT UL

INTENTIONALLY LEFT BLANK.

USER EVALUATION SHEET/CHANGE OF ADDRESS

This Laboratory undertakes a continuing effort to improve the quality of the reports it publishes. Your comments/answers to the items/questions below will aid us in our efforts.

1. ARL Report Number/Author ARL-CR-310 (Senf [POC: Gooch]) Date of Report February 1997

2. Date Report Received _____

3. Does this report satisfy a need? (Comment on purpose, related project, or other area of interest for which the report will be used.)

4. Specifically, how is the report being used? (Information source, design data, procedure, source of ideas, etc.)

5. Has the information in this report led to any quantitative savings as far as man-hours or dollars saved, operating costs avoided, or efficiencies achieved, etc? If so, please elaborate.

6. General Comments. What do you think should be changed to improve future reports? (Indicate changes to organization, technical content, format, etc.)

Organization

CURRENT
ADDRESS

Name

E-mail Name

Street or P.O. Box No.

City, State, Zip Code

7. If indicating a Change of Address or Address Correction, please provide the Current or Correct address above and the Old or Incorrect address below.

Organization

OLD
ADDRESS

Name

Street or P.O. Box No.

City, State, Zip Code

(Remove this sheet, fold as indicated, tape closed, and mail.)
(DO NOT STAPLE)

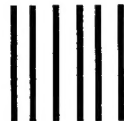
DEPARTMENT OF THE ARMY

OFFICIAL BUSINESS

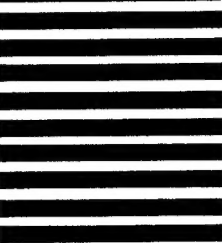
BUSINESS REPLY MAIL
FIRST CLASS PERMIT NO 0001, APG, MD

POSTAGE WILL BE PAID BY ADDRESSEE

**DIRECTOR
US ARMY RESEARCH LABORATORY
ATTN AMSRL WM TA
ABERDEEN PROVING GROUND MD 21005-5066**



**NO POSTAGE
NECESSARY
IF MAILED
IN THE
UNITED STATES**

A vertical stack of eight horizontal black bars of varying lengths, used for postal processing.